Swansea University E-Theses

Electric force microscopy of one dimensional nanostructures.

Bell, Kimberley F

Swansea University
Prifysgol Abertawe

Electric Force Microscopy of one dimensional nanostructures

By

Kimberley F. Bell BSc (Hons) MRes

Submitted to the University of Wales in fulfillment of the requirements
for the degree of Doctor of Philosophy

Swansea University

2010

Abstract

As the limitations of current technology and the possibility of scaling down of technology becomes ever more apparent the drive for smaller, faster, cheaper and more sensitive devices gains momentum. Recent literature reports new and exciting possibilities with zinc oxide based one-dimensional nanomaterials rather than the popular carbon nanotubes. The attractiveness of these one-dimensional nanomaterials is the increased surface to volume ratios and the ability of this increased surface area to exhibit sensitivity to a range of gases by altering the conductivity upon absorption of molecules on the surface. The work in this thesis demonstrated the effectiveness of the electric force microscopy technique in imaging conducting and semi-conducting samples. The technique is extremely useful in charging nanomaterials and imaging the sample discharging. This technique allows for the imaging of nanomaterials with varying applied tip bias and the results allowed the determination of a method to calculate the dielectric constant of one dimensional nanomaterials by examining the phase data. The second part of this thesis illustrates the intriguing nature of zinc oxide one dimensional nanomaterials by exploring the gas sensing capabilities of single nanowire devices. The sensitivity observed is mostly likely due to the absorption of electron donating molecules to the surface of the nanowire and hence donating charge carriers into the bulk increasing the conduction. This sensitivity can also be due to electron withdrawing molecules being absorbed onto the surface of the nanowire which reduces the conduction.

I

Declaration

This work has not previously been accepted in substance for any degree and is not being concurrently submitted in candidature for any degree.

Signed ... . (candidate)

Date ...... *20 - 1 - 11*

STATEMENT 1

This thesis is the result of my own investigations, except where otherwise stated. Where correction services have been used, the extent and nature of the correction is clearly marked in a footnote(s).

Other sources are acknowledged by footnotes giving explicit references. A bibliography is appended.

Signed . ... (candidate)

Date ...... *20 - 1 - 11*

STATEMENT 2

I hereby give consent for my thesis, if accepted, to be available for photocopying and for inter-library loan, and for the title and summary to be made available to outside organisations.

Signed .... (candidate)

Date .... *20 - 1 - 11*

NB: *Candidates on whose behalf a bar on access has been approved by the University (see Note 7), should use the following version of Statement 2:*

I hereby give consent for my thesis, if accepted, to be available for photocopying and for inter-library loans **after expiry of a bar on access approved by the Swansea University.**

Signed .... (candidate)

Date ....

Certificate of Originality

This thesis is submitted to Swansea University, Swansea, under the supervision of Professor S. P. Wilks in the Multidisciplinary Nanotechnology Centre, School of Engineering, Swansea University, Swansea in candidature for the degree of Philosophy Doctor. The material in this thesis is the original work of the author except where acknowledgement to other authors is expressly made.

Signed 20/1/11

Kimberley F. Bell

(Candidate)

Signed ....

Prof. S. P. Wilks

(Supervisor)

Acknowledgements

Contents Page

Chapter 1 Introduction to Project

Chapter 2 Zinc Oxide Nanobelts Literature Review

Chapter 3 Scanning Probe Microscopy

Chapter 4 Field Effect Transistors and Chemical Sensing

Chapter 5 Experimental Techniques

Chapter 6 Electric Force Microscopy results and Capacitance measurements

Chapter 7 ZnO Nanobelt Device Synthesis and Characterisation

Chapter 8 Conclusion and Future work

List of Tables

.

List of figures

and L, length and (c) an image of the Pt-Ir tip.

p-type nanowire 1.

Chapter 1

Introduction to Project

1.1 Aims and Objectives of Thesis

The main aim of this work was to produce a device based on a single nanowire. The objective of this device was to work as a gas sensor thus exploring the use of nanowires as gas sensing devices.

The objectives of this work are as follows;

- To produce a device which works off a single nanowire

- To use this device as a gas sensor and successfully expose the device to a range of gases for detection.

- To find a successful synthesis route using a bottom up approach to produce nanowire device without degrading either the nanowire or the electrical contacts.

- To explore the electric force microscopy technique and understand the influences on the cantilever and what this means with regard to the material being imaged.

- To apply the electric force microscopy technique to different materials and examine how difference materials affect the results.

- Explore zinc oxide nanowires with the thought of application as single nanowire devices.

1.2 Introduction

" I would like to describe a field in which little had been done,

but in which an enormous amount can be done in principle "

Richard P. Feynman "There's plenty of Room at the bottom" Dec 26 1959

The scale of interest to nanotechnologists ranges from a maximum of a few micrometers down to 1 nanometer in size. Figure 1.1 shows clearly the interesting end of the scale with a strand of naturally occurring DNA being marginally bigger than manufactured carbon nanotubes. It is down at this end of the scale where the materials and their properties become increasingly

varied and interesting as many do not behave as they do in macro size or as we would expect them to. This is the driving force behind the exciting new world that is nanoscience.

In order to manufacture and produce increasingly smaller materials and devices with new or improved properties/responses a new way of fabrication was developed and is being constantly improved upon. The fabrication techniques can be split into two separate components, top-down and bottom-up. As the name suggests the top-down technique starts with a larger scale material and its dimensions are reduced by means of etching, cutting and grinding until the desired nanostructure is reached. Bottom-up involves the assembly of smaller sub-units to produce a larger nanostructure. This bottom-up technique is the more recently developed of the two due to its dependence on the development of microscopes which enable to precise movement of nanosized materials.

1.3 What is Nanotechnology?

The term nanotechnology covers the design, construction and utilisation of functional structures with at least one dimension measured in nanometers [1]. The increase in surface area increases the surface free energy, decreasing particle size, which leads to changes in the inter-atomic spacing of the material. Nanoscale structures have a very high surface area to volume ratio, which makes them ideal catalysts. These catalysts can increase rate, selectivity and efficiency of chemical reactions.

The surface area to volume ratio has always been an important consideration when exploring science. In chemistry the surface to volume ratio has an effect on the reactivity of materials for example a material with a large surface to volume ratio (i.e. a very small diameter or very porous) will react much faster as more surface area is available for interactions. This ratio also has an enormous impact in biology with determining the size and shape of cells depending upon function for example gas exchange cells having a higher surface area to volume ratio. Materials should have constant physical properties regardless of the size from bulk to nanoscale however this is not observed and hence the ratio of surface to volume becomes even more important when considering the change in properties and behaviours of materials at the nanoscale. For a bulk material the percentage of atoms at the surface of a material becomes insignificant in relation to the number of atoms in the bulk. However at nanoscale the number of atoms on the surface of a material is much more than the number of atoms in the bulk of the material.
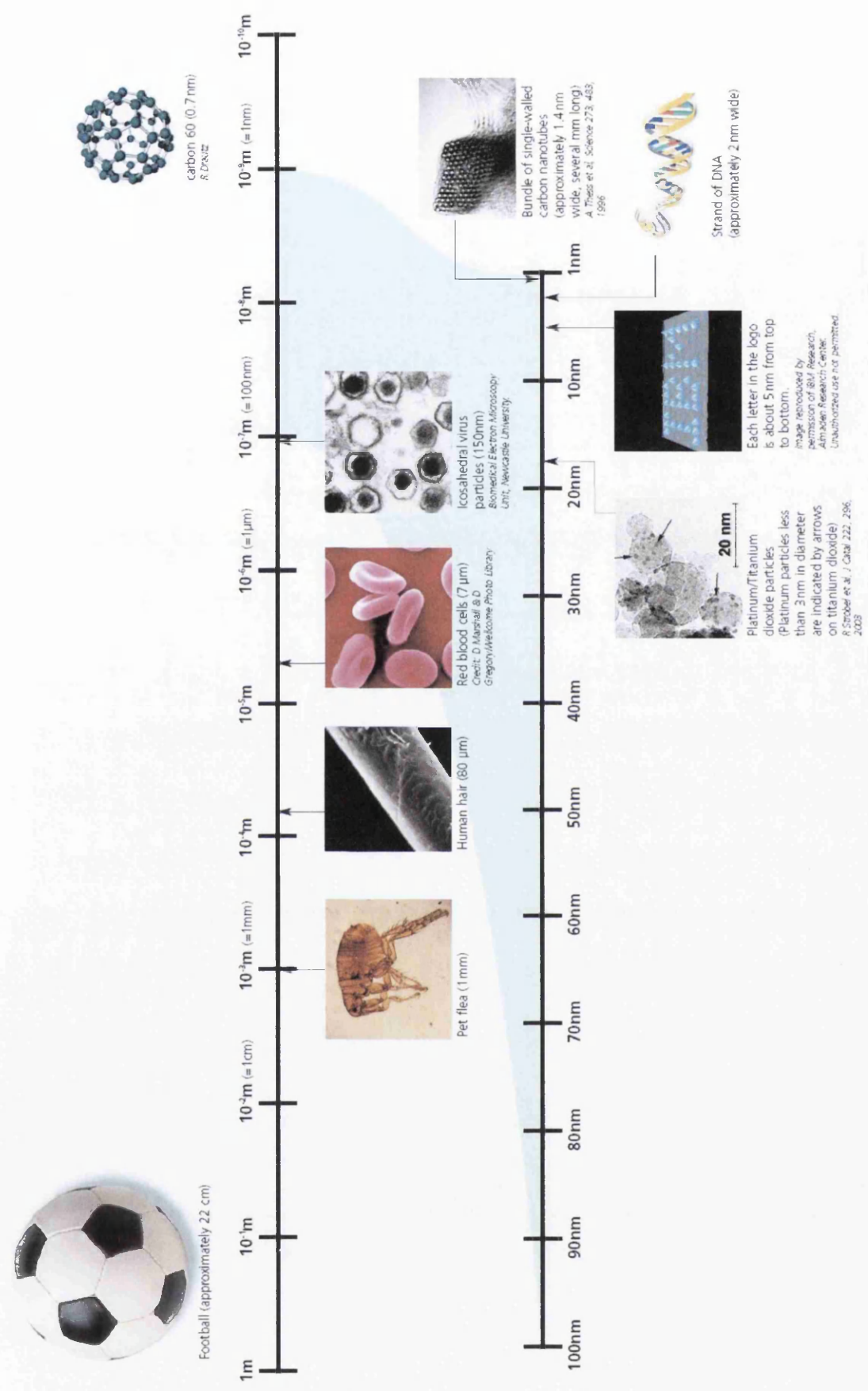
Figure 1.1 Length scale of interest in Nanotechnology [2].

Hence the material becomes more surface dominant at the nanoscale. As observed from the graph (figure 1.2) when the volume is small the surface area is large and vice versa. This would indicate that when examining nanoscale materials which have a very small volume the surface area of the material would be dominant and therefore control the observed physical properties and be the reason behind any observed changes in behaviour at the nanoscale.
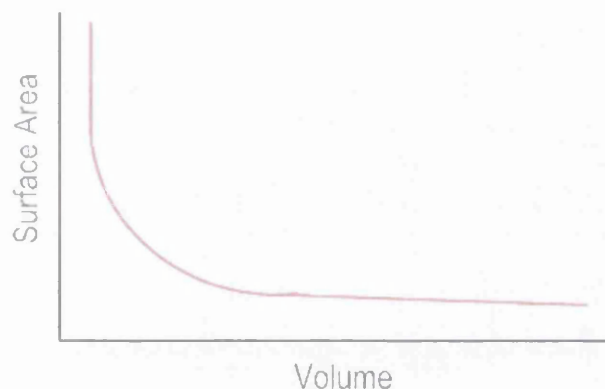
Figure 1.2 The Surface area to volume ratio shown in graphical form.

In many materials the properties of the bulk vary wildly when compared to the material at the nanoscale. For example gold in bulk form is a shiny yellow colour, conducts electricity and is inert, however nanogold is an excellent catalyst, a semiconductor and has a range of colours including red, blue and yellow [3]. The reduced dimensionality affects the electronic structure of the atom. It affects the energies of the highest occupied molecular orbital (HOMO), valence bond and the lowest unoccupied molecular orbital (LUMO). The optical emission and adsorption depends upon transitions made between the electronic states mentioned. This would indicate that nanoscale materials would have different optical properties when compared to the bulk material.

1.4 Fabrication Techniques

A vast array of sophisticated tools has been developed to manipulate and investigate materials [4]. These tools are shown in figure 1.3 and can vary in quality, speed and cost. There are two distinct fabrication routes Top-down and Bottom-up. Top-down manufacturing begins with a large-scale pattern and then reduces the lateral dimensions to carve out nanostructures. The techniques used in top-down include etching, cutting and grinding and also lithography.
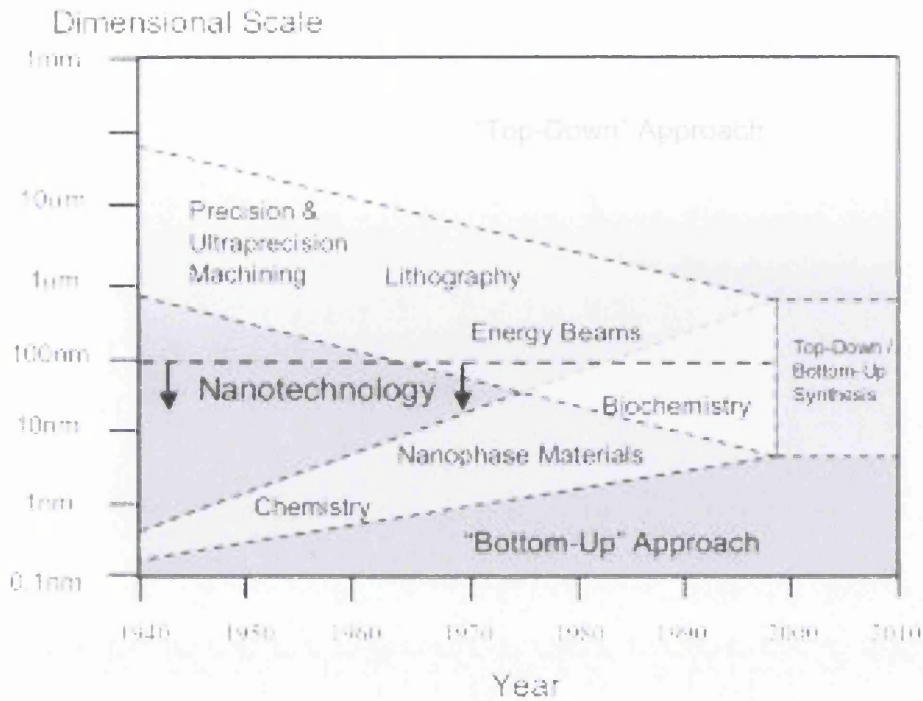
Figure 1.3 A scale illustrating the change in the synthesis approach of nanomaterials [2].

Bottom-up manufacturing is the more recent development of the two processes. It involves the assembly of sub-units to produce a much larger structure. Position engineering, chemical synthesis and self-assembly are all examples of bottom-up manufacturing.

The ability of each of these techniques to produce nanosized materials and devices is slowly converging due to the development of more sophisticated equipment (Figure 1.3). In the early part of the 20th century bottom-up approaches focused on chemical techniques to produce smaller materials and the precision engineering and machining developed the top-down approach. In the late 20th early 21st century these two techniques are converging and are able to synthesis materials in the same size range of 1um - 5nm.
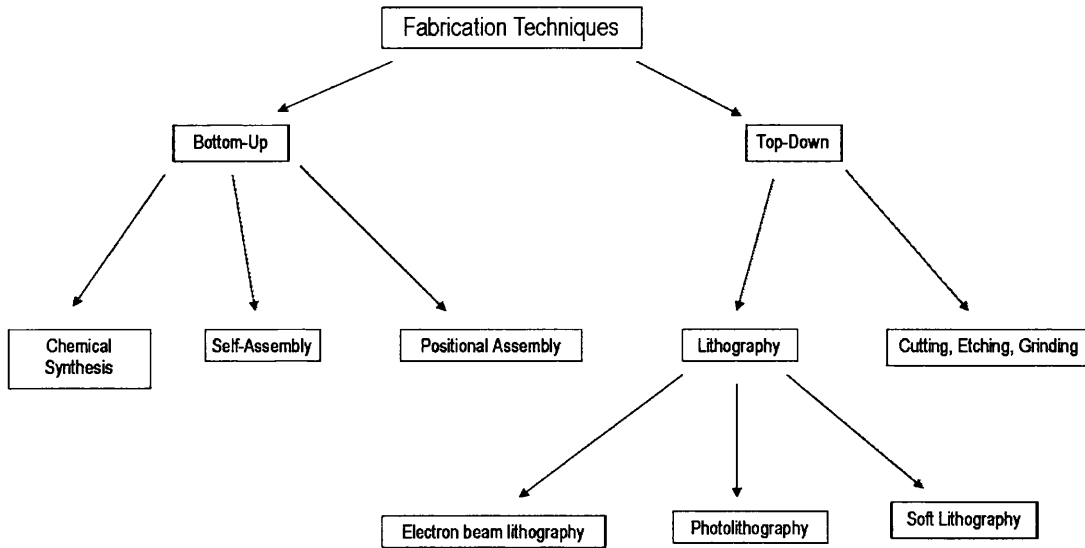
Figure 1.4 Overview of fabrication techniques illustrating the two branches of synthesis.

1.4.1 Top-Down Manufacturing

Top-down manufacturing takes advantage of conventional techniques to synthesise nanostructures. Milling or mechanical attrition is an example of grinding. A coarse material is crushed mechanically between rotating hard balls of steel. This repeated deformation causes a large reduction in particle size. This process is industrially applicable as it can be repeated continuously, however the resulting material cannot be influenced. Lithography is a technique widely used to produce nanostructures especially within the semiconductor industry. Controlled patterns are requires for a range of applications including integrated circuits, sensors for chemical detection, arrays for biomedical research and also data storage.

Lithography can be broken down further into photo, soft and electron beam lithography. Photolithography is an extension of the technique utilised in photography and is widely used within the semiconductor industry to manufacture microchips [5]. There are two sections to this process, one involving the production of a mask, which is slow and expensive, and the

second, the use of the mask to manufacture replicas, which is rapid and inexpensive. Figure 1.4 outlines schematically the photolithography process.
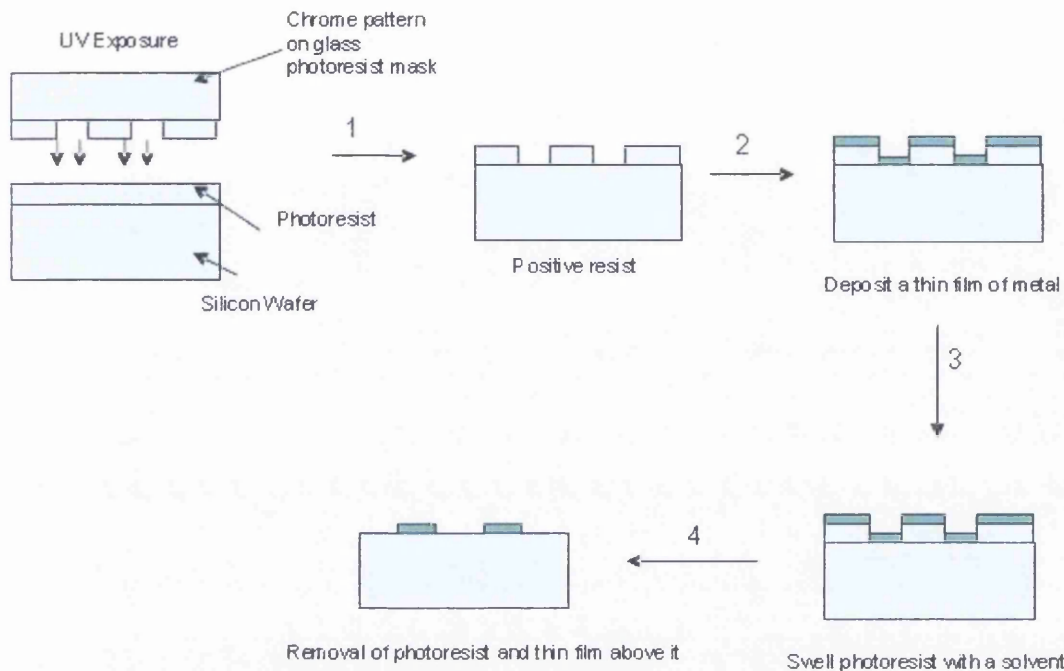
Figure 1.5 Graphical illustration of the Photolithography technique used to synthesis nanomaterials using a 'bottom-up' approach.

Step one is to spin coat a polymer resist onto a substrate and bake to remove any excess solvent [6]. The next step is to expose the resist to UV radiation from a mercury arc lamp through a patterned mask usually chromium. Treat the sample with solvents to dissolve exposed regions in a positive resist or unexposed regions in a negative resist. This step produces a template for the pattern to be etched onto the substrate. Step 5 involves the etching of the sample by treatment with hydrofluoric acid (wet etching) or by dry plasma etching, to remove the uppermost layer of the substrate. The final step is to remove all remaining resist leaving only the required pattern on the substrate. Photolithography is limited due to diffraction problems when the resolution required is less then 1um. The resolution can be determined by equation1.1. This illustrates the relationship between the resolution (minimum feature size) and the wavelength of light used where C is the material dependant constant.

Minimum feature size = C x λ / numerical aperture of focusing lens   *Equation 1.1*

The demand for ever-smaller devices has increased the demand to be able to manufacture microchips on a large scale. One possible synthesis route would be to use a beam of electrons, which have a much shorter wavelength than UV light and hence can have a resolution of approximately 5nm [7]. The required circuitry pattern is written using a high-energy beam of electrons onto a thin polymer film. This can be very time consuming and expensive and hence not a viable option for large-scale production.

Soft lithography utilises either of the techniques described above to produce a pattern in a layer of photo resist which is on the surface of a substrate for example silicon wafer. This generates a bias relief master where the island of photo resist protrudes from the substrate; a chemical precursor (polydimethylsiloxane [PDMS]) is then poured over the master and is cured into a rubbery solid. This part of the process is expensive as it requires the application of either photo or electron beam lithography. This rubbery solid is a stamp, which can be used to reproduce the desired pattern fairly cheaply to produce nanostructures. This stamp can be placed onto a hard surface and a liquid polymer flows by capillary action into the recesses between the surface and the sample. This process is termed Micromolding and can reproduce patterns as small as 10nm. This technique has enabled the production of sub-wavelength optical devices.

The advantages of using techniques such as the ones described above can promote further miniaturisation of devices with high precision and reduction in production costs. However the process of producing nanostructure using a top-down method can be very time consuming and can produce a massive amount of wastage.

1.4.2 Bottom-Up Manufacturing

Bottom-up manufacturing involves the highly controlled deposition and growth of materials to synthesise nanostructures. Bottom-up encompasses a range of techniques including chemical synthesis, positional and self-assembly.

Positional assembly takes advantage of recent developments including atomic force microscopy (AFM) and scanning near field optical microscopy (SNOM). Atoms are deliberately manipulated and positioned individually. Optical tweezers are an example of this technique and operate by using the radiation pressure from a focused laser beam to trap

particles. These trapped particles can then be manipulated and moved around the sample. This is extremely laborious and is not really applicable to industry as they are very expensive, custom built instruments.

Self-assembly involves the arrangement of atoms/molecules into structures with little or no external influence [1]. The atoms can arrange themselves by physical or chemical interactions such as Van der Waal forces of attraction. Self-assembly can be seen occurring naturally for a sustained period of time however it is only recently been exploited by industry. This technique is attractive to industry as it forms very little waste and requires very little in the way of input hence cost effective to run.

Chemical synthesis can be carried out in either, solid liquid or gaseous phases. The more common synthesis route is physical vapour deposition (PVD) (ref to Chapter 5 experimental details). PVD is the thermal decomposition of gaseous species at high temperatures and subsequent condensation and deposition onto a substrate located in a lower temperature region. This can occur with or without a catalyst however, the presence of a catalyst increases the rate of the reaction but can interfere with the grown nanostructure as it is often found terminating the nanostructure.

1.5 Conclusion and Outline of Thesis content.

There are two distinct routes for synthesis of nanostructures, bottom-up and top-down. This thesis concentrates on the 'bottom-up' synthesis route utilising techniques such as photolithography to produce a nanobelt device with applications in chemical sensing and nanoelectronics.

Chapter 2 describes a technique for imaging nanomaterials termed atomic force microscopy. This technique allows the precise imagining of nanoscopic materials *in situ* by examining the changes of the cantilever position due to an interaction with the surface forces. This technique was extended to include electric force microscopy to enable the electrical charges of the surface and in turn allow the charging of zinc oxide nanobelts.

Chapter 3 outlines the recent literature published in the area of zinc oxide nanobelts and why they have become such a fascinating nanomaterial to work with. The crystal structure is examined including the basic chemistry and physical parameters. The nanobelts themselves

exhibit a vast array of interesting and exciting properties, which leads on to a wide variety of potential and real applications.

The application of nanobelts in the area of transistors and processes such as chemical sensing are covered in Chapter 4. Chapter 5 and 7 describes the techniques used to synthesis the nanobelt device and the results obtained from electrical measurements and chemical sensing experiments respectively.

Chapter 6 concentrates on the technique of electric force microscopy and the application of this technique on silicon and zinc oxide nanowires in order to determine the dielectric constant for each material.

Chapter 8 brings together all the research including an outline for future work. This chapter also covers the social and ethical considerations needed to exploit this technology to the fullest but in a safe and unbiased manner.

1.6 References

1.   Kelshall R., H.I., and Geoghegan M., , *Nanoscience and Technology*. 2005, John Wiley & Sons: London UK. p. 32-54.

2.   Engineering, T.R.S.T.R.A.o., *Nanoscience and nanotechnologies: opportunities and uncertainties*. 2004. p. 1-116.

3.   University, L. (2004) *Nanogold Does Not Glitter, But Its Future Looks Bright*. Science Daily **Volume**,

4.   Christie B., *Nanofabrication*. Scientific American, 2001. **285**(34).

5.   Whitesides G. H., a.L.J.C., *The art of Building Small*, in *Understanding Nanotechnology from the Editors of Scientific American*. 2002, Warner Books: New York USA. p. 36-55.

6.   Cowie J. M. G., in *Polyers: Chemistry and Physics of Modern Materials*. 1991, Blackie Academic and Professional: Glasgow UK. p. 399-432.

7.   Wilson M., K.K., Smith G., Simmons M., and Raguse B. , *Nanotechnology: Basic science and emerging technology*. 2002: Chapman & Hall/CRC.

Chapter 2

Zinc Oxide Nanostructures

2.1 Introduction

Interest in Zinc Oxide originates from experiments conducted to determine the lattice dimensions of the crystal in 1935 [1]. Bunn characterised zinc oxide using x-ray powder photographs. He found lattice dimensions of a_0 = 3.242Å and c_0 = 5.1948Å which is consistent with the values shown in table 1, which are used as the parameters for all zinc oxide analysis. From this starting point interest in the inorganic compound gained momentum and was found to be a semiconductor with a variety of interesting properties with far reaching applications. Zinc oxide exhibits semiconducting and piezoelectric properties which has lead to applications such as nanogenerators [2]. The compound shows the ability to form diverse and abundant configurations of nanostructures such as nanowires [3] [4], nanorings [5] and nanohelixes [5] to name a few. There are many advantages to zinc oxide as a nanomaterials and a selection explored in this chapter. Zinc oxide occurs as a white powder and is nearly insoluble in water and alcohol however it does degrade when mixed with an acidic solution. The advantages range from chemical, biological, electrical, mechanical and optical. Zinc oxide demonstrates the ability to exhibit electrical properties of a semiconductor while showing extraordinary mechanical properties. These properties allow zinc oxide to have a variety of applications within industry ranging from field effect transistors, chemical sensors and biosensors. The advantage of using zinc oxide is that it is biocompatible and also environmentally friendly. The biocompatibility of zinc oxide has been explored by exposing epithelial cells and subcutaneous connective tissue to zinc oxide nanowires [6]. The cells grew and reproduced in the presence of the nanowires. Some of the cells even phagocytosed some of the broken nanowires, they are engulfed the nanowires in the cell membrane and formed an internal phagosome containing the nanowire. Phagocytosis normally occurs in the acquisition of nutrients or in the immune system to remove pathogens. This illustrates that zinc oxide is biocompatible as the cells grew and reproduced undisturbed by the presence of the nanowires. This is an important step in the potential application of nanowires within the bionanotechnology sector.

2.2 Zinc Oxide Crystal Structure

Zinc is a d-block transition metal with an electronic structure of (Ar) $3D^{10}\,4S^2$. Each atom of zinc is tetrahedrally surrounded by four oxygen atoms to ensure the d-orbital electrons are hybridised with $2p_y$ and $2p_z$ lone orbital electrons of oxygen [7]. The zinc oxide molecular bond is ionic in nature. It is also an amphoteric oxide, which is nearly insoluble in water and alcohol but degrades in both acidic and basic conditions.

Bulk Zinc oxide has a wurtzite crystal structure with alternating planes in an ABABAB array which is the most stable and hence most common at ambient conditions [8]. The structure is illustrated in figure 2.1 with the oxygen atoms (anions) forming a hexagonal close packed formation and the zinc atoms (cations) occupy half the tetrahedral holes in the lattice. The lattice parameters are measured to be a = 3.25Å and c = 5.205Å. The ratio of c:a is approximately 1.60 which is comparable to the ideal hexagonal cell ratio of 1.6333. This would indicate that the ideal structural formation is hexagonal.

O^{2-}

Zn^{2+}
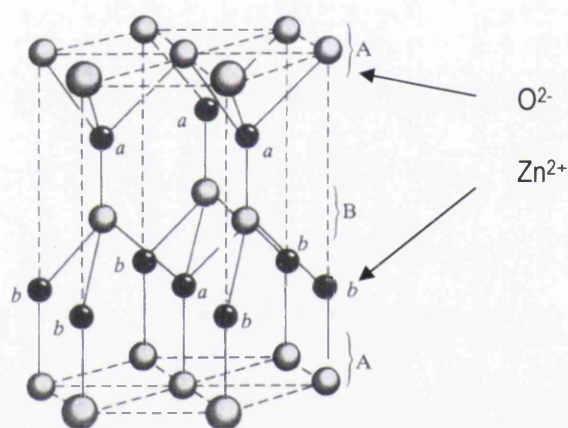
Figure 2.1 wurtzite structure of ZnO [8].

Zinc oxide is an II-IV semiconductor and has a band gap of 3.37eV, as illustrated in table 2.1, which is typical of transition metal complexes. The band gap describes the degree of ionic character in the bonds of the compound [9]. There are many advantages to possessing a large band gap including higher breakdown voltages, lower electronic noise, high temperature and power operation and the ability to sustain large electric fields for a considerable period of time.

Physical Parameter	ZnO
Molecular weight	81.389
Lattice Type	Wurtzite
Space Group	P63mc
Lattice Parameters	a=3.25Å
	c=5.205Å
Melting Point (K)	2250
Band gap energy (eV)	3.37
Exciton binding energy (meV)	60

Table 2.1 Physical parameters of bulk Zinc Oxide[7].

ZnO has many interesting and varied properties. It has a wide band gap, which would indicate that it is transparent in the visible range of the spectra. ZnO has a very large exciton binding energy of 60meV (table 2.1), which indicates the ability to operate a lasing mechanism at room temperature.

2.3 Synthesis: Growth Mechanisms

There is a vast array of synthesis routes that have been explored in recent literature, however due to this only a selection have been covered in this chapter. In order to determine which synthesis route is more appropriate structural analysis of grown nanostructures needs to be completed after the growth has occurred. New techniques have allowed the in situ monitoring of growth by x-ray diffraction [10]. X-ray diffraction patterns were collected at room temperature before, after and at 5-minute intervals during heating. Two types of structures were observed, one-dimensional and two-dimensional. The one-dimensional structures include nanowires and branched nanostructures. These one-dimensional structures appeared to grow out from the original zinc particles that were used as the source material. It was also observed that at higher growth temperatures straight nanowires were grown however at much lower growth temperatures, branched nanowires were the dominant structure formed. The existence of branched nanostructures determined that the growth occurred at the tip of the nanostructure rather than at

the base due to the location of the branches. This would rule out the ability of a self-catalysed mechanism where growth would occur at the zinc/zinc oxide interface. The two-dimensional nanostructures were in the form of zinc oxide layers grown on the source zinc particles. These layers would detach from the zinc particles when the growth temperature was lowered and the sample was cooled due to thermal contraction of the layers.

The dependence of the morphology of nanostructures on the growth temperature can be explained by examining changes with the vapor pressure. The vapor pressure of zinc will increase with increasing temperature. This increased vapor pressure could encourage one-dimensional growth by increasing the availability of zinc particles away from the surface. Examination of the kinetics data shows that growth occurs before the growth temperature is reached, as the experimental data does not begin at the origin. This would indicate that the growth of nanostructures begins as soon as the temperature is increased above room temperature and not necessarily just at the growth temperature.

2.3.1 Vapour Transport Synthesis

Vapour Transport synthesis is the most common synthesis route in the production of nanostructures [11]. This is a highly effective technique and can produce large quantities of nanostructures and at relatively low cost [12]. Vapour transport can be categorised into two separate growth mechanisms;

1. Catalyst free vapour-solid process
2. Catalyst assisted vapour-liquid-solid process

Both of these routes lead to the formation of an array of interesting and varied nanostructures.
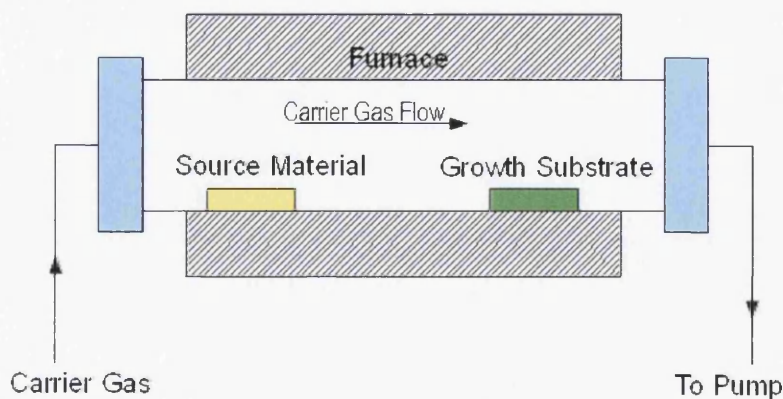
Figure 2.2 Schematic of horizontal tube furnace for thermal evaporation of nanostructures.

The experimental set-up is essentially the same for each growth mechanism. This includes a horizontal tube furnace containing a narrower alumina / ceramic quartz tube in which alumina boats containing the substrate and source material are placed (figure 2.2). One end of the tube is connected to the pump system and the opposite end is connected to the carrier gas supply. The carrier gas and the pumping ratio are controlled by a needle value connected to a flow meter. Both ends of the system are sealed with circular rubber rings.

The procedure parameters are important factors to consider as they have a profound affect on the morphology, size and yield of the nanostructures synthesised.

- Temperature: The temperature of both the vaporisation and the condensation occurs are dependent on the volatility of the source material. The evaporation temperature must be high enough for the source material to vaporise and the condensation temperature must be low enough for the molecules to condense. The exact temperatures used will depend upon the source material and the evaporation and condensation conditions for that particular element. The substrate is placed further down stream from the source materials, the further this distance the bigger the temperature difference will be. The local temperature at the position of the substrate will determine the size, shape and number of nanostructures obtained.

- Pressure: The pressure is dependant upon the vapour pressure of the source materials and the evaporation rate.

- Carrier Gas: The carrier gas is used to help the flow of source material from the initial position to the substrate. This carrier gas must be inert and not participate in the reaction on going within the horizontal tube furnace. For this reason argon gas is the most commonly used gas in thermal evaporation techniques. The flow rate of this gas can also be tuned to give the maximum and finest yield of products.

- Substrate: The type of substrate used in the growth needs to be robust enough to withstand the range of temperatures required throughout the growing process. The crystallography of the substrate is also important consideration as this will have an affect on the growth planes of the nanostructures.

- Evaporation time period: Evaporation time period is the amount of time in which the products are allowed to grow.

The concentration of oxygen within the chamber also needs to be tightly controlled as it influences the volatility of the source material, the stoichiometry of the vapour phase and the formation of the products.

2.3.1.1 Vapour-Solid Process (V-S process)

The V-S process is a catalyst free mechanism by which the nanostructures are formed by condensing directly from the vapour phase into the solid phase. A condensed source material is vaporised at an elevated temperature, which is higher than the melting point of the material, in a horizontal tube furnace [3]. This produces a vapour, which will condense on to a substrate under certain parameters further down the tube furnace in the lower temperature region.

The ability to synthesise without the need for a catalyst is an important process when producing nanostructures with interestingly terminated structures, which would be hindered by the presence of a catalyst particle. ZnO nanoneedles were grown by a metal organic chemical vapour deposition, essentially a VS mechanism [13]. The substrate used was <111> silicon that had been cleaned in an ultrasonic bath with acetone and methanol. The source materials consisted of diethyl zinc (Et_2Zn) and oxygen with flow rates of 20-100sccm and 0.5-5sccm respectively. The growth temperature was in the range of 400°C to 500°C and the growth time was 1 hour. A correlation was observed between the growth time and the diameter and lengths of the nanoneedles produced. The growth time of approximately an hour yielded the superior results with lengths of 740nm and diameters of 40nm. The sizes of the nanoneedles were also affected by changes in the temperature and pressure of the growth chamber. Electron microscopy analysis of the resulting structures showed nanoneedles with very sharp tips that appeared to grow vertically from substrates. These nanoneedles showed uniform distribution in diameter, length and density. The nanoneedles showed high crystallinity and excellent photoluminescent characteristics according to the results.

A similar method was used in the synthesis of zinc oxide nanorods as discussed by Ogata et al [14]. Source materials included diethyl zinc (Et_2Zn) and nitrous oxide (N_2O) and high purity N_2 was used as the carrier gas. The nanostructures were grown at 200Torr in a horizontal tube furnace. The flow rate was altered so that the ratio of (N_2O)/ (Et_2Zn) was between 500 and 100,000. Two types of substrates were utilised. One was a sapphire substrate and was pre-

treated to obtain an atomically flat surface and the growth temperatures ranged from 500°C to 900°C. This method produced columnar structures of ZnO with diameters of 10-50nm. The diameter of the nanorods increased with increasing growth temperature and this property could be used to achieve the growth of nanorods with a desired diameter for a specific application. However when the temperature was 900°C this produced almost flat ZnO epilayers.

The second substrate explored was bulk <0001> ZnO, which had been cleaned with an organic solvent before growth. Flat uniform layers of ZnO were grown at a reduced maximum temperature of 800°C. A decrease in growth temperature was due to the easy evaporation of oxygen, which would leave a large number of oxygen vacancies in the nanowire.

ZnO nanowires have been synthesised by what is described as vapor-solid mechanism but included the use of a thin film of Tin on silicon wafer as a catalyst [12]. The nanowires grown have clean tips unlike the vapor-liquid-solid mechanism, which is said to be metal seeded, produces nanostructures with catalyst particles located at their tips. The vapor solid mechanism proposed for the growth of zinc oxide nanowires is illustrated in Figure 3. Tin has a very low melting point and is molten before the zinc oxide vapor is formed in the reaction tube (figure 2.3(b)). Increasing the temperature to growth temperature of approximately 850°C produces zinc/zinc oxide vapor and the tin supersaturates. Precipitation of zinc oxide occurs at these mechanism seeds of supersaturated tin. Controlling the vapor pressure of zinc oxide in the furnace allows the nanowires to continue to aggregate and grow from the tin surface as demonstrated in figure 2.3 part c.
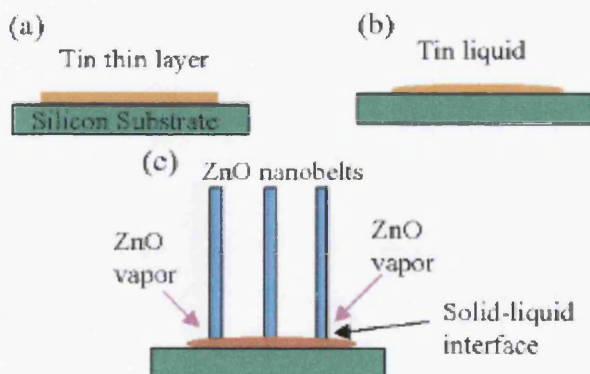
Figure 2.3 Illustration of the mechanism of the formation of zinc oxide nanowires on a tin catalytic layer [12].

This method illustrates that it is not always necessary to pre-synthesise catalyst nanoparticles as in the conventional vapour-liquid-solid mechanism in order to control the nanowire size. The large tin particles, formed in figure 2.3 part b, provide an effective catalytic point for growth and allows a small amount of control over the size of the nanowires produced.

The method produces a wide variety of nanostructures including nanowires, nanorods, nanowires and complex nanostructures such as nanotubes and nanotetrapods. A selection of images obtained through the mechanisms described above is illustrated in figure 2.4. The diverse range of nanostructures produced indicates that less control over the geometry, alignment and precise location of the products is inevitable with this process.
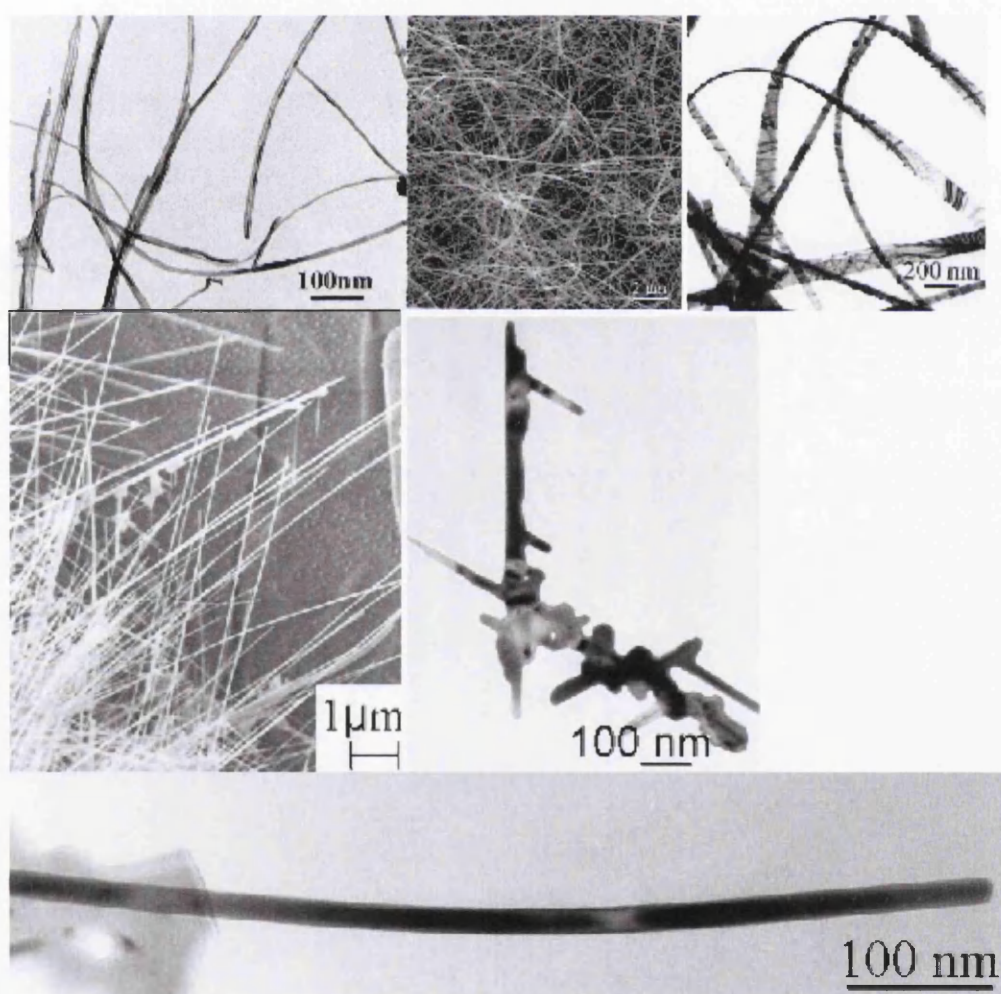
Figure 2.4 (a) TEM image of ZnO nanowires [12] (b) SEM image of the as-synthesised ZnO nanowires [15] (c) TEM image of ZnO nanowires [15] (d) SEM image of as grown nanowires [10] (e) TEM images of a branched nanostructure [10] (f) TEM image of a single nanowire [10].

2.3.1.2 Vapour-Liquid-Solid Process (V-S-L process)

V-S-L process is a more controlled catalyst assisted method leading to the production of nanowires, nanorods and nanotubes. Typical catalysts used include nanoparticle or nanoclusters of gold [11, 16], copper [17], cobalt [18] and tin [19-21].

A eutectic alloy droplet forms at each catalyst site on the substrate as illustrated in step 1 of figure 2.5.This droplet is supersaturated with source material, in this case zinc, leading to nucleation and growth of the solid nanostructures in step 3. Incremental growth occurs at the droplet interface, which constantly pushes the catalyst particle upwards. The catalyst particle terminates the end of the nanostructures and is responsible for the diameter of the grown nanostructures.
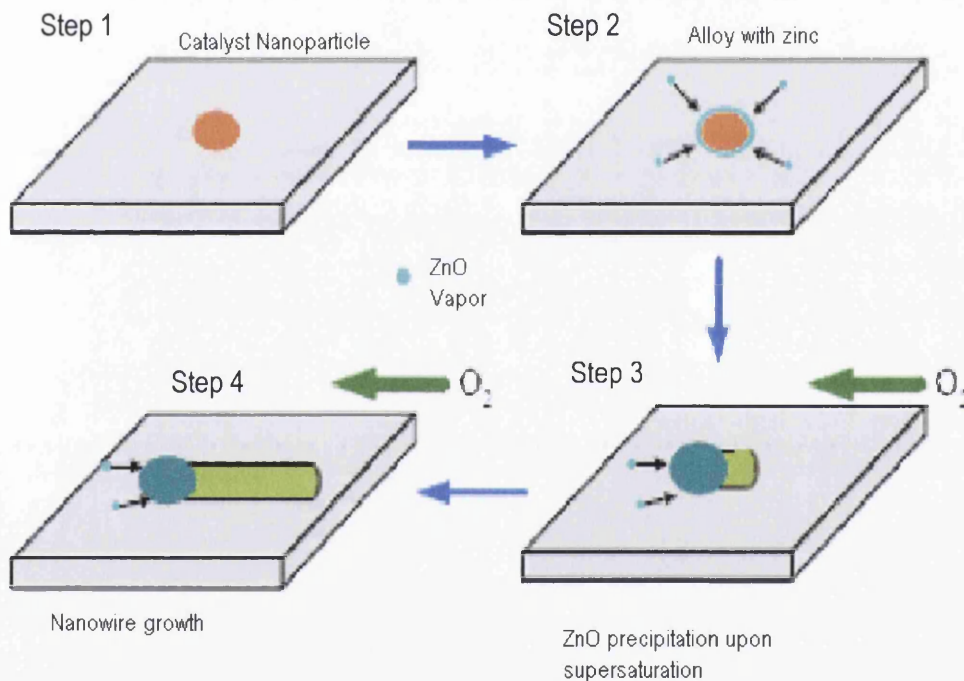
Figure 2.5 Schematic of VLS process showing the catalyst particle forming an alloy with zinc and under flow of oxygen the precipitation and supersaturation steps to synthesis of a nanowire [11]

This technique provides site-specific nucleation at each catalyst site and allows for the controlled growth of nanostructures. Altering the size of the catalyst particle can control the diameter of the nanostructure and also patterning the substrate with catalyst particles to create an array by both lithographic and non-lithographic techniques can control the location and alignment of growth.

Historically VLS synthesis has been utilised for over four decades. Wagner and Ellis describe the mechanism of vapour-liquid-solid mechanism of silicon whiskers published in 1964 [22]. This mechanism can be applied to controlled growth methods including those used to produce filamentary crystals and epitaxial layers. A small particle of gold is placed on a <111> silicon wafer and the sample is heated to 950°C. This heat treatment forms an alloy of gold and silicon on the substrate. A mixture of hydrogen and silicon tetrachloride (SiCl$_4$) gas is introduced into the growth chamber. It is suggested that the liquid alloy takes on the role of catalyst for the subsequent chemical reaction. The silicon molecules enter the alloy droplet and begin to freeze out at the interface between the substrate and the liquid alloy. This process continues gradually forming a whisker (Figure 2.6), which increases in size under the alloy. As shown in the diagram the alloy is now located on top of the growing whisker. This whisker continues to grow until either the growth conditions have altered or all of the gold catalyst has been consumed during the reaction.
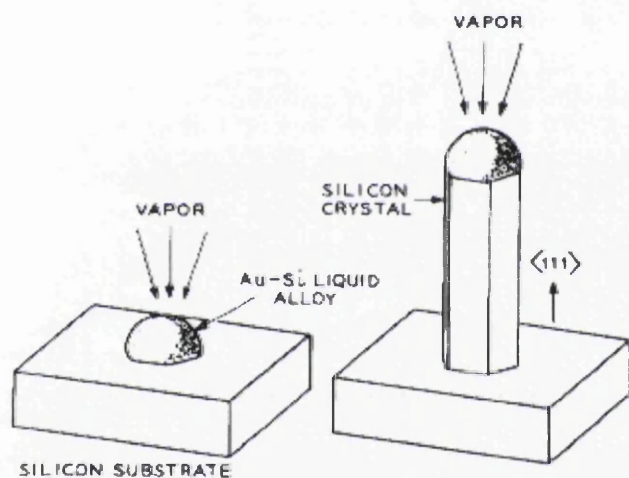
Figure 2.6 Illustration of vapor-solid-liquid mechanism of a single silicon whisker [22].

The work of Wagner and Ellis was an important step to understanding growth conditions and the possible synthesis routes to produce the desired nanomaterial. Their work was subsequently explored and improved to produce a variety of nanostructures using the vapour-liquid-solid (VLS) mechanism as shown in Figure 2.7.

The choice of catalyst is heavily dependant upon the growth temperature which is required for the synthesis of nanostructures [19]. The catalyst is required to be in a liquid state at the growth temperature and it also cannot form a solid solution with the nanowire. Growth only terminates

when the temperature drops below the eutectic temperature of the alloy or if the reactant is not longer readily available.
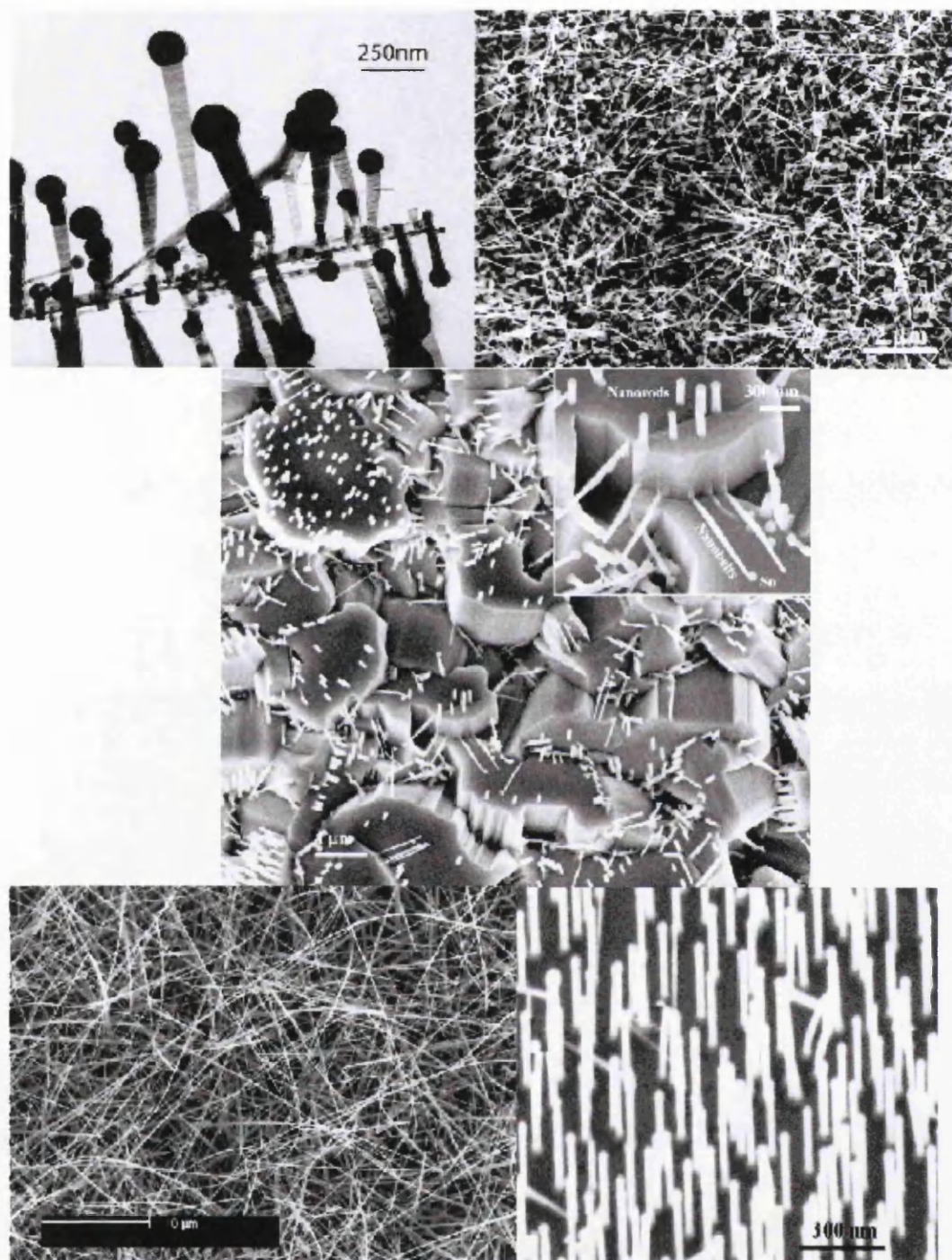
Figure 2.7 (a) TEM image of nanowire-nanoribbon array [21] (b) SEM image of tin guided ZnO nanowires and nanowires [19] (c) SEM image of ZnO nanorods and nanowires grown on top and side surfaces of ZnO microrods [20] (d) SEM image of ZnO nanowires[23] (e) Aligned ZnO nanorod array[20].

2.3.2 Laser Ablation

This technique requires the removal of material from a solid surface by irradiating it with a laser. This allows precise control over the nanostructures obtained. When the laser is operated at a low flux the material is heated by the absorbed energy from the laser and consequently evaporates. However when a high flux is used, the material is converted straight into plasma. A variety of nanostructures can be synthesised this way including zinc selenide (ZnSe) nanowires [24], Gallium nitride nanowires [25], and zinc oxide nanorods [26]. Zinc oxide thin films were grown on Al_2O_3 and GaN substrates at various laser wavelengths using a pulsed laser technique. A high-powered pulsed laser beam is focused to strike the zinc oxide target, which was placed 40mm away from the substrate. The zinc oxide molecules were then vaporised from the target and deposited as a thin film on the substrate. When the laser pulse is absorbed by the zinc oxide target, energy from the laser is first converted to electronic excitation and then into chemical and thermal energy. This evaporates the zinc oxide into the surrounding vacuum followed by the nucleation and growth of the zinc oxide thin film on the substrate. Scanning Electron Microscope images of the thin films showed a random arrangement of zinc oxide nanorods on both the Al_2O_3 and GaN substrates [26].

2.3.3 Template directed method

Template directed technique utilises the substrate to guide the growth of nanowires. This method has produced large scale arrays of zinc oxide nanowires [27] as well as zinc oxide nanowires on carbon nanotube tips [28]. The hexagonal gold arrays were made through a masking technique of a metal membrane nanotube mask. The membranes were electrochemically replicated from a master template and showed enhanced flexibility and ease of usage. These hexagonal substrates were used to produce arrays of vertically aligned nanowires in an identical hexagonal array. The nanotubes were grown via a vapour deposition technique that involved a horizontal tube furnace with a mixture of zinc oxide and graphite powders in a boat at one end of the tube and the patterned substrate 6cm away downstream. The nanowires synthesised had the same hexagonal structure as the gold array. In the usual vapour deposition technique it would be expected for the gold particles to be at the top of the nanowires. However in the case reported gold did not appear at the top of the nanowires that would suggest the growth mechanism illustrated in Figure 2.2.8. The gold hexagonal disks fragment into smaller particles and form alloys with the zinc vapor atoms (figure 2.8(a)). These gold and zinc particles coagulate into

larger droplets. The precipitation and coagulation of zinc forms a central zinc oxide nucleus (figure 2.8 (b)). The zinc atoms encroach and move about on the surface due to their higher vapour concentration (figure 2.8(c)). These atoms nucleate and amalgamate into the zinc oxide lattice at the peak, as it is the lowest energy site. Figure 2.8(d) shows the zinc oxide pillars formed after growth and cooling of the substrate. It is also evident that the gold nanodots remain around the base of the zinc oxide structure.
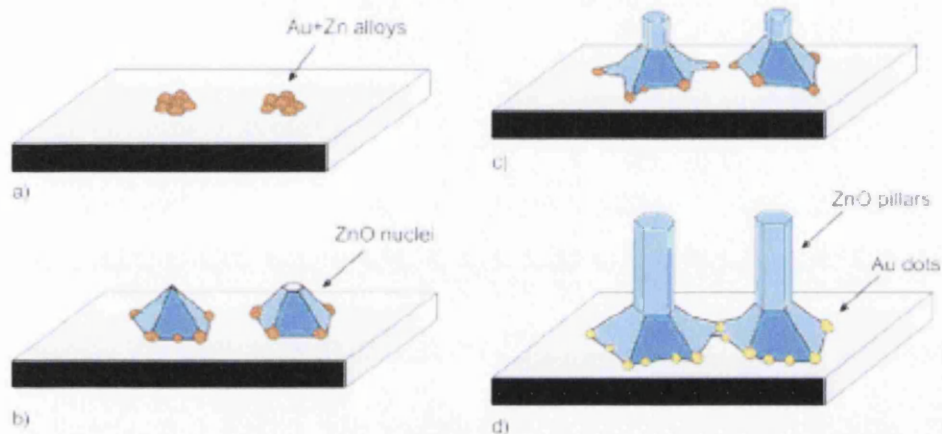
Figure 2.8 Growth mechanism suggested for the growth of zinc oxide nanowires on gold patterned substrate [27].

Carbon nanotubes can also be used as growth sites for zinc oxide nanowires [28]. An array of multiwalled carbon nanotubes was used as a platform for the directed growth of zinc oxide nanowires. The multiwalled carbon nanotubes were selected as the platform due to their ability to contend with both synthetic and biological materials. Gold nanoparticles were added to the ends of the nanotubes by DNA hybridisation. One sequence of DNA attached to the terminus of the nanowire and the second sequence of DNA with the gold nanoparticle attached then combines with the first sequence. A removal step for the DNA is not required as the DNA sequences are vaporised at the growth temperature (600°C) of the zinc oxide nanowires. This method generated sequenced nanowires in an ordered array.

2.3.4 Other synthesis routes

2.3.4.1 Wet Chemical route

Synthesising nanostructures through wet chemical routes has many advantages including proper mixing of precursors at molecular level, reaction kinetics can be controlled by choosing the correct

solvent and the growth can be controlled by using the correct and appropriate ligands [29]. During gas-phase synthesis nucleation, growth and coalescence all occur at the same time, which allows the possibility of a disordered structure. In the wet chemical approach the nucleation and growth can be monitored and influenced in real time. Chemical synthesis of zinc oxide nanowires occur from a reaction between the precursor molecule Zn $(CH_3CHOO)_2.2H_2O$ with ethanol and excess deionised water as the solvent. Refluxing this solution gave zinc hydroxy double salt with a chemical formula $Zn_5(OH)_8(COOCH_3)_2$. This solution then underwent hydrolysis without the presence of a catalyst due to the excess amount of water present forming colloidal particles. The colloidal particles were confirmed to be zinc oxide nanoparticles by scanning electron microscope analysis. Zinc oxide nanowires formed after the addition of a catalyst to the monodispersed nanoparticles through anisotropic agglomeration. The nanowires formed were examined through scanning electron microscopy.

2.3.4.2 Hydrogen Treatment

Hydrogen treatment of zinc oxide thin films at 425°C produced well aligned zinc oxide nanorods [30]. The nanorods produced were examined with a transmission electron microscopy and found to be 40nm in diameter and longer than 450nm in length. The nanorods synthesised were significantly longer than the films were thick which suggested that rather than being etched from the films themselves they were grown on the films. However prolonged hydrogen treatment resulted in all the nanorods collapsing back on to the substrate. It was proposed that both the etching and redeposition occurred during the hydrogen treatment, producing enhanced zinc oxide nanorods.

2.4 Properties

2.4.1 Electrical

In order to utilise zinc oxide nanowires to their full potential exploring their remarkable electrical properties is a must. The electrical characteristics of single zinc oxide nanowires have been studied mainly through field effect transistor devices based on these single nanowires of zinc oxide and there is a vast amount of literature published on this topic [3, 11, 31, 32]. The characteristics of theses devices were examined by I(V) curves as shown in figure 2.9 where different gate voltages were applied to the nanowire and the corresponding I(V) curve was examined.
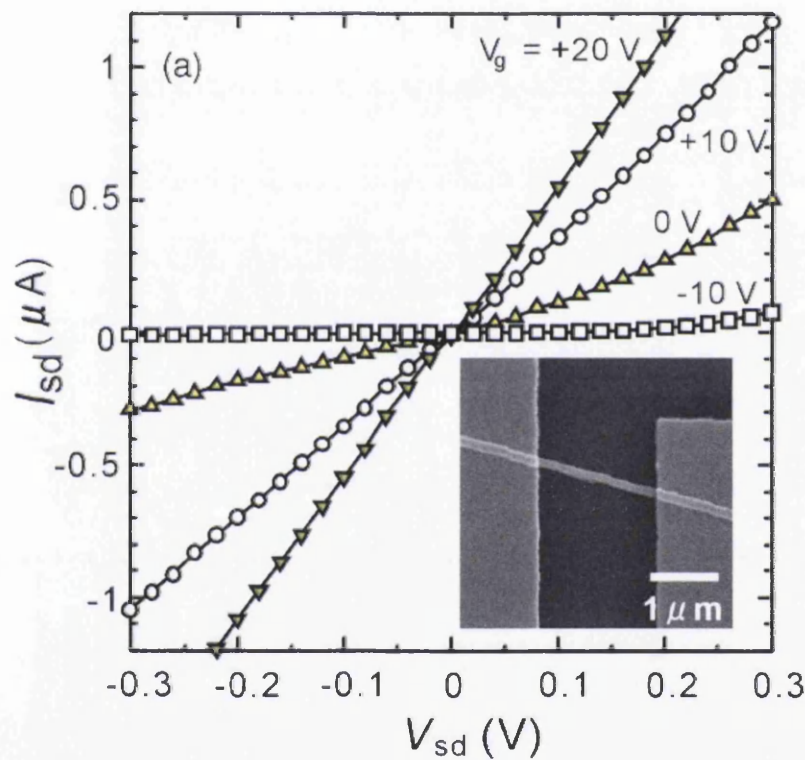
Figure 2.9 I(V) characteristic of a single zinc oxide nanowire probed using Ti/Au electrodes as varying gate voltages, with insert SEM image of nanowire bridging electrodes [31].

The zinc oxide nanowire was deposited on Ti/Au electrodes using a photolithographic technique and a SEM image of the resultant device is seen in the insert in figure 2.9. The device was explored using differing gate voltages -10V, 0V, +10V and +20V. The results in figure 2.9 show that as the gate voltage increased in the positive sense the conductivity of the nanowire also increase and this improved the linearity in the curves. The increased conductivity was due to an increase in carrier concentration which was a direct result of a higher gate voltage. The improved

linearity seen in the results is due to carrier doping in the contact region between the nanowire and the electrodes. The dependence of the nanowire on the gate voltage indicated that the sample was n-type semiconductor. Research shows that due to the oxygen vacancies and zinc interstitials the more common behaviour illustrated by zinc oxide nanowires is that of n-type semiconductor. The breaking point of the applications of zinc oxide nanowires is determined by the ability to p-type doping of the zinc oxide nanowires. The successful p-type doping of the nanowires will enhance their potential applications in nanoscale electronics and optoelectronics.

Vertically aligned Zinc Oxide nanowires have also been explored as electric field emission devices [11]. Tseng et al grew very thin and needle shaped zinc oxide nanowires on a Ga-doped ZnO film as shown in figure 2.10 (a). These nanowires were grown in almost perfect vertical alignment.
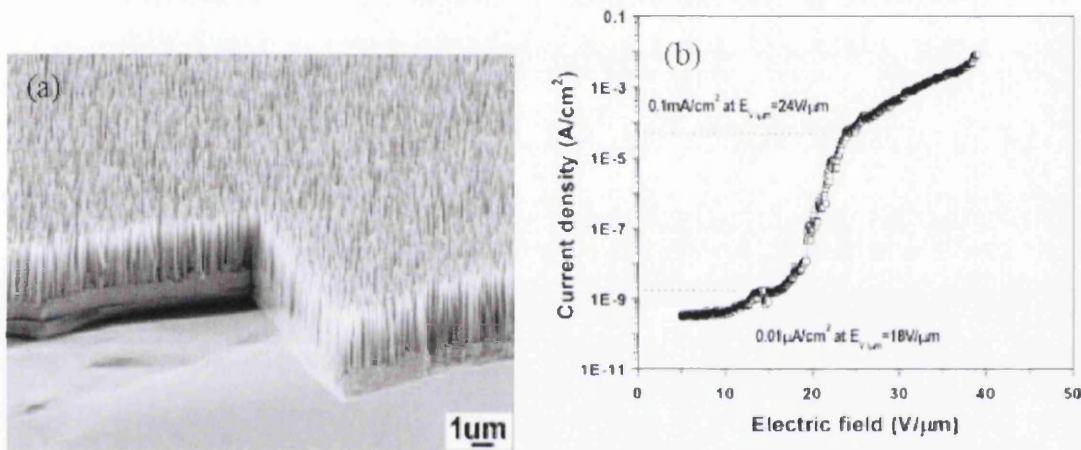
Figure 2.10 (a) Image of vertically aligned zinc oxide nanowires and (b) I(V) characteristics of the emission from zinc oxide nanowires [11].

The results from the electric field emission are shown in figure 2.10 (b) which shows the current density with electric field. The turn-on field was found to be ~18V/μm at a current density of 0.01μA/cm^3. The emission current reached 0.1mA/cm^2 at 24V/μm.

2.4.2 Mechanical

Investigating and characterising the mechanical properties of nanowires is a major step in discovering applications for these potential revolutionising materials in nanodevices. The main technique used is based around nanoindentation of nanowires with a probe such as an atomic force microscope (AFM) tip.

ZnO nanowires were bridged over 1µm wide trenches on a standard atomic force microscope (AFM) three-dimensional reference sample [33]. Both ends of the belt were mounted by deposition a thin layer of carbonaceous material over the nanowire and the supporting material using electron-beam induced deposition. The AFM was used to locate the centre of each single nanowire over a trench and in situ apply a force at the centre by contacting the tip with the nanowire. Any changes in morphology were recorded by directly imaging the nanowire after the bending test. The nanowire was tested on a solid substrate (without any trenches) in order to eliminate both the indentation effect and the tip cantilever deflection effect on the result.
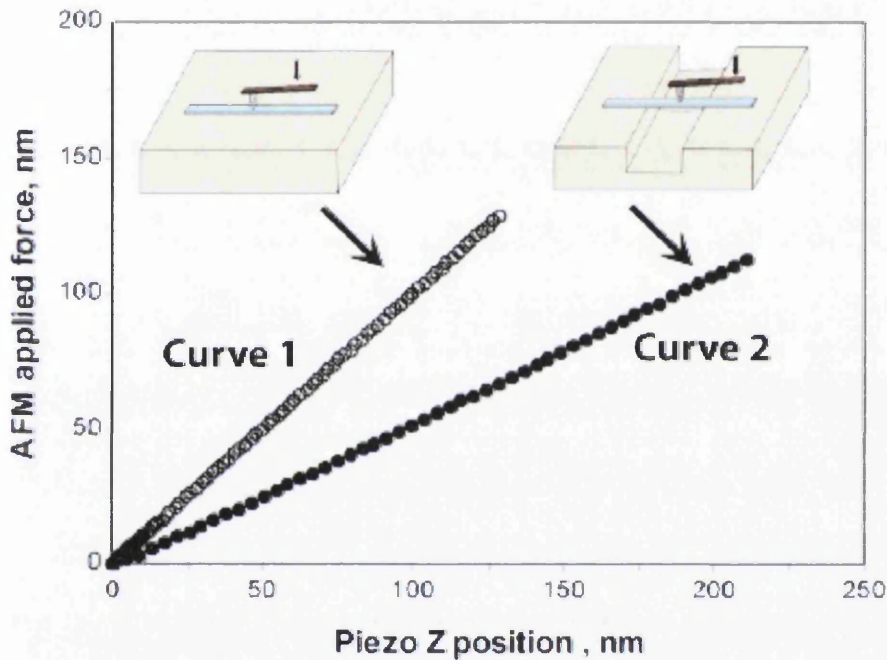
Figure 2.11 Cantilever deflection baseline (curve 1) and nanowire and cantilever deflection (curve 2) [31].

The results clearly show a linear relationship between the applied force and the deflection of the nanowire except that when a load of 22.2µN is applied the final fracture point of the nanowire is reached.

The spring constant of each nanowire must be known in order to calculate the Youngs modulus of each nanowire. The spring constant is defined as the gradient of the initial linear portion of the applied load and deflection curve. The nanowire is assumed to follow the linear elastic theory of an isotropic material hence the Young's modulus (E_n) can be calculated from equation 2.1.

$$E_n = \frac{FL^3}{192 d_n I}$$

Equation 2.1

Reducing the equation down to equation 2.2 where, I is the moment of inertia.

$$E_n = \frac{k_n L^3}{192 I}$$

Equation 2.2

For a nanowire, having a rectangular shape, the moment of inertia is given by

$$I = \frac{bh^3}{12}$$

Equation 2.3

Where b is the width and h is the height of the nanowire. L describes the length of nanowire over the trench and F is the applied load at the mid point position across the nanowire.

Reducing the equation for the Young's modulus to

$$E_n = \frac{3 k_n L^3}{48 b h^3}$$

Equation 2.4

The effect of the surface-to-volume ratio of the zinc oxide nanowires was also explored and it was determined to have no effect on the Young's modulus. This could be due to the fact that the nanowires examined were of 100nm thickness and width and maybe the effect would be more pronounced in nanowires of the size 10nm. It would be expected that the surface-to-volume ratio would affect the Young's modulus (and other mechanical properties) as the more surface atoms that exist, the more active they are and the easier they can move when compared to the internal atoms. The Young's modulus obtained from three point bending experiments was approximately 38.2 ± 1.8 GPa. The Young's modulus determined from the nanoindentation experiment was 31.1 ± 1.3 GPa. The disagreement in these results could be due to more surface atoms being involved in the three point bending and surface atoms are much easier to stretch than atoms that are locked into the crystal lattice. No plastic deformation was detected during the bending even

though nanowires have a single crystal structure. Also before and after bending the nanowires showed almost no alteration in their morphology at the point of contact (centre of the belt), which would lead to the conclusion that brittle fracture has occurred. Brittle fracture occurs when no apparent plastic deformation is observed.

The plastic deformation capability of zinc oxide nanowires were explored by performing indentation creep tests using two different loading schemes. A peak indentation load of 20µm was applied to an indenter with and without the holding segment of 5s.
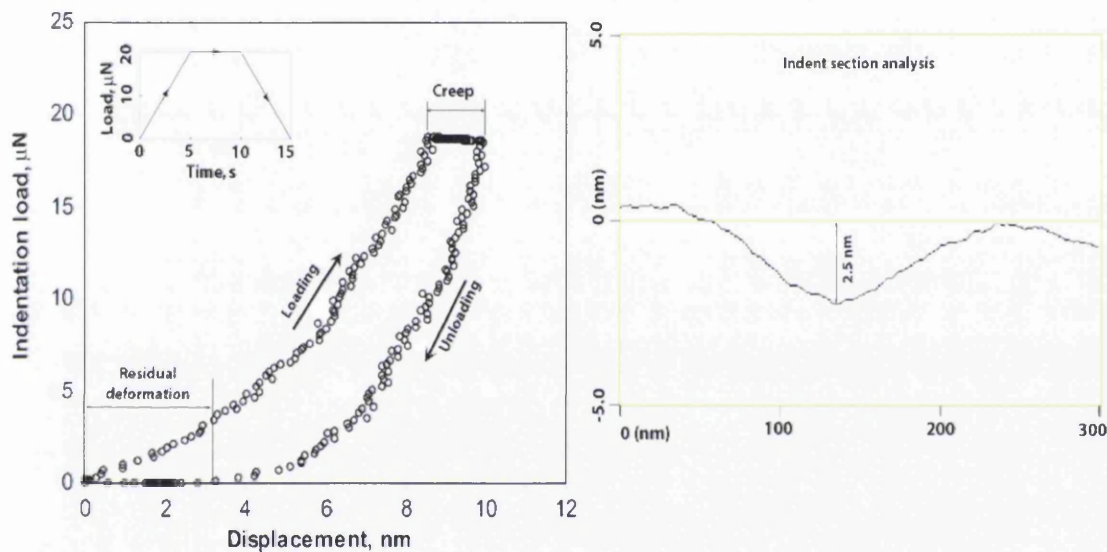
Figure 2.12 (a) nanoindentation load-displacement curve with holding segment (b) AFM Line profile of the indentation [33].

A permanent deformation occurred at room temperature after the load was removed. This deformation is shown in the line profile (Figure 2.12 (b)) and measures 2.5-3nm deep. This result is consistent with the result obtained from the curve of indentation load and displacement (Figure 2.12 (a)) and is labelled on the graph as residual deformation. The creep observed where the displacement continues to increase without any addition load. This is believed to be due to the generation of dislocations within the nanowire structure. The fact that residual deformation and creep suggests that plastic deformation is not present under the three point bending test.

The mechanical characteristic of zinc oxide have been compared to those of tin dioxide nanowires in a comprehensive study [34, 35]. The characteristics were explored using a similar method as the one described above. Tin dioxide nanowire was found to be stiffer and harder than zinc oxide from data of applied load as a function of penetration. The lower the penetration of the indent on the nanowire, the higher the hardness of the material. This property can be attributed to the strain gradient effect during nanoindentation. Bulk zinc oxide was also examined for comparison to zinc oxide nanowire. The nanowire was found to be softer than the bulk probably due to the difference in crystal planes with bulk having <0001>, which may be harder than the <2110> crystal plane along the nanowire. The elastic modulus was found to be higher in tin dioxide than zinc oxide.

2.4.3 Optical

The optical properties of nanowires are important to consider when exploring potential applications for example as photonic devices [3, 7, 11]. Photoluminescence can be described quantum mechanically as excitation to a higher energy state by the absorption of a photon and upon falling back down to the original state emitting a photon of a specific wavelength. Photoluminescence spectra can be helpful in measuring the purity and crystalline quality of semiconductors. Zinc oxide nanowires of varying diameters were examined using a He-Cd laser of wavelength 325nm as the excitation source [36]. Strong emission at 380nm was seen for all belts and yellow-green emission at 520nm was observed to increase as the nanowire size decreased (figure 2.13). The green emission is generally attributed to deep level and trap state emission. In this case of zinc oxide it can be due to the singly ionised O_2 vacancy in zinc oxide and the emission is from the radiative recombination of a photo-generated hole. The increase in green emission with decreasing diameter indicates that a greater proportion of O_2 vacancies in the thinner nanowires due to the increase in surface area to volume ratio.
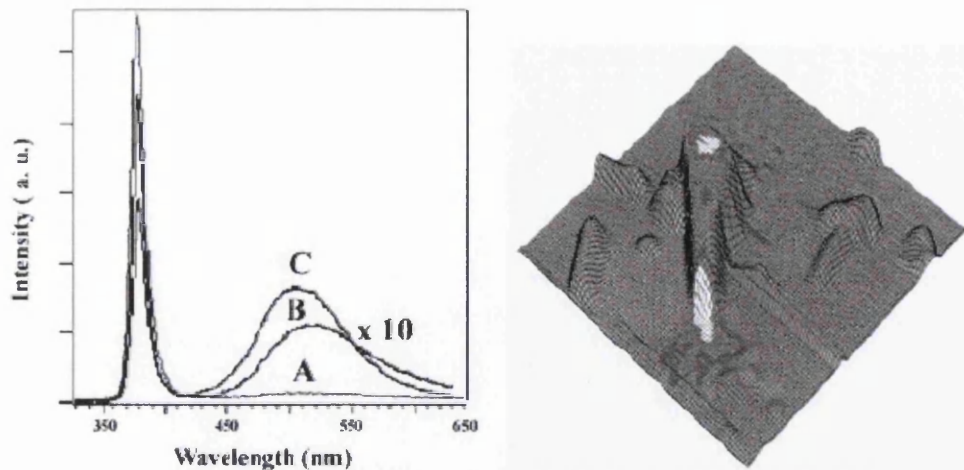
Figure 2.13 (a) Photoluminescence spectra of ZnO nanowires of varying diameter A 100nm, B 50nm and C 25nm and (b) near field scanning microscopy image of a single zinc oxide nanowire [36].

As well as exploring the photoluminescence of zinc oxide nanowires the lasing potential of these nanostructures has also been explored due to the high exciton binding energy (60meV) which would allow excitonic lasing mechanism to operate at room temperature [7]. The lasing properties of single zinc oxide nanowires were explored with the aid of near-field scanning optical microscopy [36]. In the figure 2.13 a strong photoluminescence emission can be clearly seen at the end of the nanowire and only very weak emission was observed at the side surfaces.

2.5 Applications

2.5.1 Nanoresonators and Nanocantilevers

Nanowires can be excited by an applied electric field to resonate at a specific frequency if the applied frequency matches that of the natural resonance frequency of the belt [3]. Two fundamental resonance frequencies were given from classical elasticity theory and corresponded to the vibration in the thickness and width directions. These two modes were looked at separately in the experiments with images shown in figure 2.14 (b) and (c). One end of the nanowire was fixed, while the opposite end was free to vibrate.

(a)　　　　(b)　　　　(c)
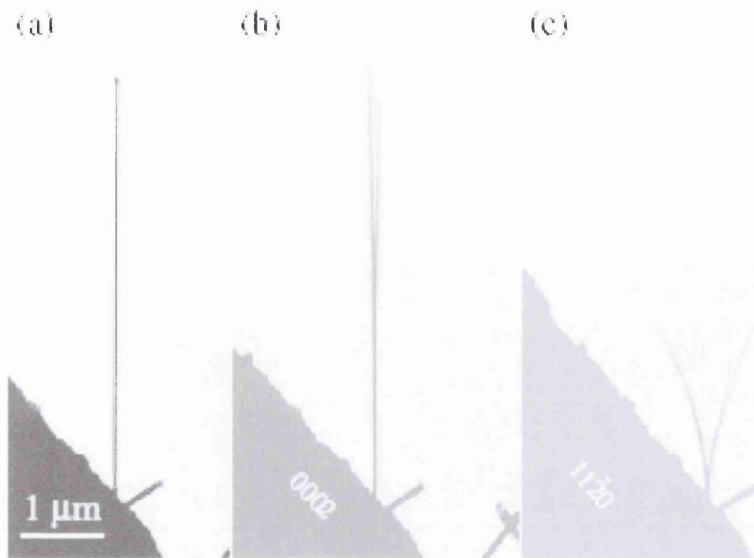
Figure 2.14 Nanoresonators (a) before the application of an electric field (b) and (c) resonating nanowire from two different viewing angles [3].

This vibration was examined and recorded using a transmission electron microscope. The bending modulus of the nanowire was calculated and determined to be of the order of GPa $(1\times10^9 Pa)$. Previous research has allowed the determination of other materials bending modulus, which have all been in the region of MPa $(1\times10^6 Pa)$, an order of magnitude smaller than the calculated value for zinc oxide nanowires. The experiment showed that nanowires can be effective resonators and could have potential applications as probes for scanning probe microscopy experiments.

As cantilever based scanning probe microscopy is the most powerful tool available to image, manipulate and measure nanoscale properties the discovery of more sensitive cantilevers is paramount [37]. Nanowires are idea cantilevers due to their single crystal structure, which nearly void of defects, and the excellent mechanical properties they have been shown to exhibit. The nanoscale dimensions of the belts, approximately 35-1800 times smaller that conventional cantilevers, have the potential to improve sensitivity whilst scanning. Figure 2.15 shows the ability of the atomic force microscope to pick up selected nanowires, which would be a potential method in mounting a nanowire as a probe. Another attractive feature is the ability to tune the resonance frequency of each cantilever in order for use in different imagining modes of microscopy i.e. contact, tapping or non-contact as shown by Wang et al.
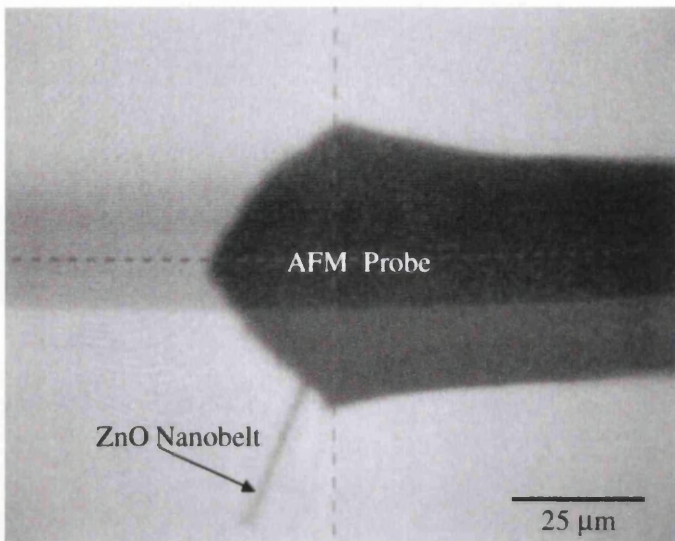
Figure 2.15 Optical image of a ZnO nanowire connected to an AFM probe [37]

2.5.2 Nanogenerators

The powering of nanodevices needs to be solved in order to make practical applications of the devices into society [2, 38]. A nanogenerator based on zinc oxide nanowires requires an external disturbance such as movement to bend the aligned arrays converting mechanical energy into electric power. Previous studies have shown that a voltage drop occurs when a nanowire is bent laterally which results in positive voltage observed on the tensile side and a negative voltage on the compressive side [39]. One end of the zinc oxide nanowire is stuck to a silicon substrate with silver paste, which leaves only one end free to move. A conductive tip of an atomic force microscope was scanned over the nanowire and the output voltage was recorded but no external voltage was applied to either the sample or the conductive tip of the microscope. When the tip made contact with the wire and pushed it but didn't scan over the top surface of the wire, no voltage output was recorded. This result leads to the conclusion that the stretched side of the nanowire did not produce a piezoelectric discharge (figure 2.16 (a)). However once the tip was scanned over the top surface of the wire and touched the other side, which was now under compression, a sharp voltage peak was observed as shown in part (b) of figure 2.16.
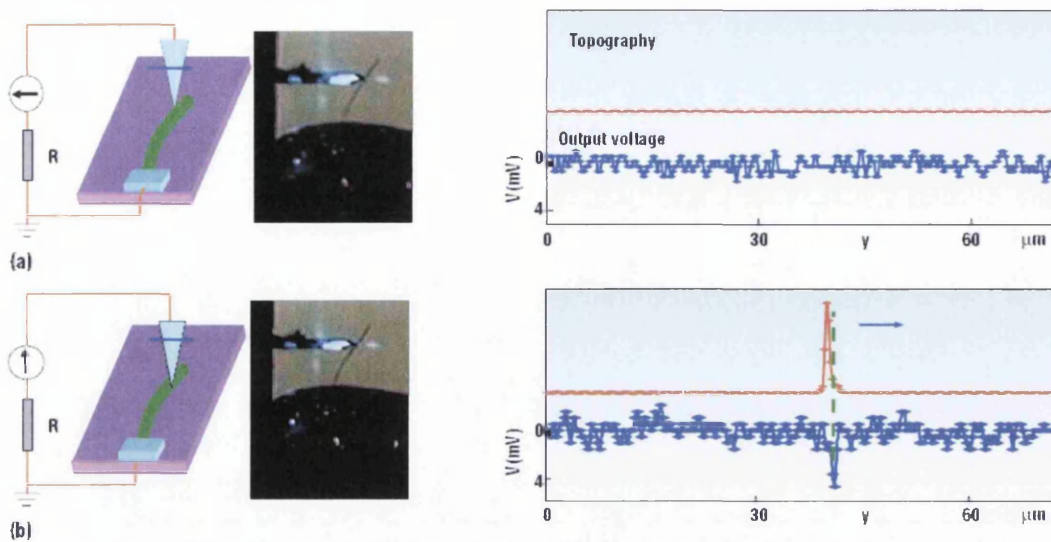
Figure 2.16 (a) the tip touching the stretched side of the nanowire producing no output voltage (b) tip touching the compressed side producing a sharp peak in the output voltage [38].

This result occurred as the tip had almost crossed the width of the wire. This would indicate that unlike the previous result a negative piezoelectronic discharge voltage was produced.

In order to be applied in industry applications this technique requires up scaling to include an array of nanowires in order to not only produce more output but to also be more robust. A silicon electrode with a zigzag shape was coated with platinum metal and covers an array of aligned nanowires as illustrated in figure 2.17. The platinum coating enhances the conductivity and also is required to create a Schottky diode at the interface with zinc oxide nanowire array [40]. Another electrode was placed above the nanowire array and was manipulated from a controlled distance. This electrode plays the role that the atomic force microscope tip did in the previous experiment.

The zigzag shaped electrode was excited by an externally applied ultrasonic wave. This pushed the nanowires resulting in lateral bending creating a strain field across the nanowire width. As in the previous experiment the outer surface of the nanowire was in tensile strain and the inner surface was in compressive strain. When the electrode contacted the stretched surface, with a positive piezoelectric potential, the metal-zinc oxide interface is reverse biased resulting in very little current flowing. The electrode was pushed further and the bent nanowire now reached the other side of the adjacent tooth of the zigzag electrode. This process allowed the electrode to be in contact with the compressed side of the nanowire and the metal-zinc oxide interface is now a forward biased Schottky barrier. This produces a sudden increase in output current flowing from the top electrode.
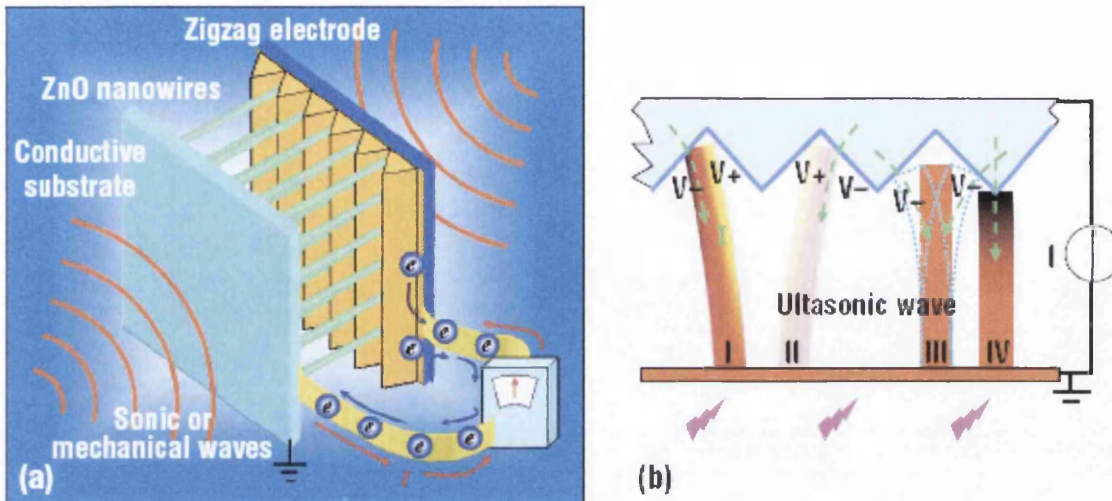
Figure 2.17 (a) Diagram illustrating the nanogenerator using an array of aligned nanowires (b) Schematic showing the interaction of the nanowire and zig-zag electrode and the resulting output [38].

Nanogenerators could be used to convert a range of different sources of energy into electrical energy [2] for example

- Mechanical energy from body movement, muscle movement or blood vessel contraction.

- Vibration energy from acoustic or ultrasonic waves.

- Hydraulic from the flow of bodily fluids or blood.

The main challenge is to efficiently convert these sources of energy into electrical energy.

A movement driven nanogenerator converts the biomechanical energy into electricity. This occurs with a single wire generator where a zinc oxide nanowire is fixed laterally at both ends on a flexible substrate (polyimide film) and the entire single wire generator is packaged with a flexible polymer[5, 41]. This is then attached to a human finger and the muscle movement results in the stretching of the substrate and hence the nanowire laterally as shown in figure 2.18. The single wire generator was attached to the top side of the joint position of an index finger. The nanowire was approximately 100-800nm in diameter and 100-500μm in length. The repeated bending of the finger produces a cycled strain in the nanowire. The movement of the device and the subsequent deformation of the nanowire generated a piezoelectric potential, driving the flow of external electrons which produces an electric power output.
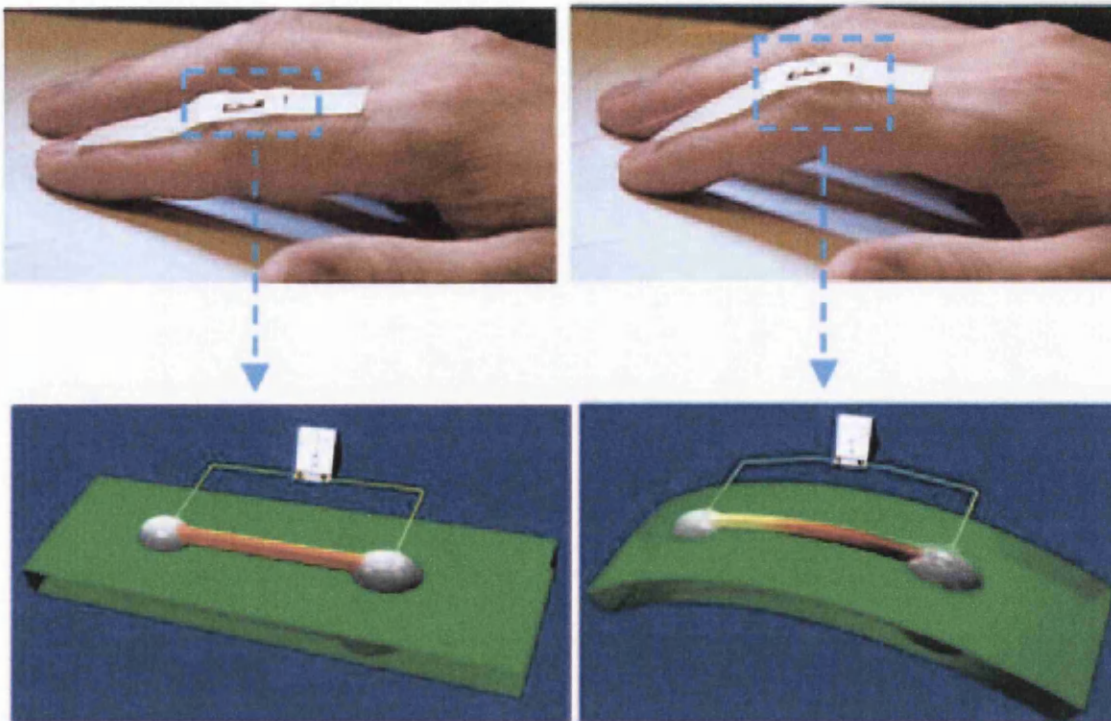
Figure 2.18 A nanowire fixed laterally to a flexible substrate and attached to a human finger [42].

As the finger oscillates at a slow pace the voltage and current output is recorded, results shown in figure 2.19. The voltage output was at a maximum value of 20mV when the finger was bent to the maximum point. The current output had a maximum value of more than 150pA from a single nanowire generator device.
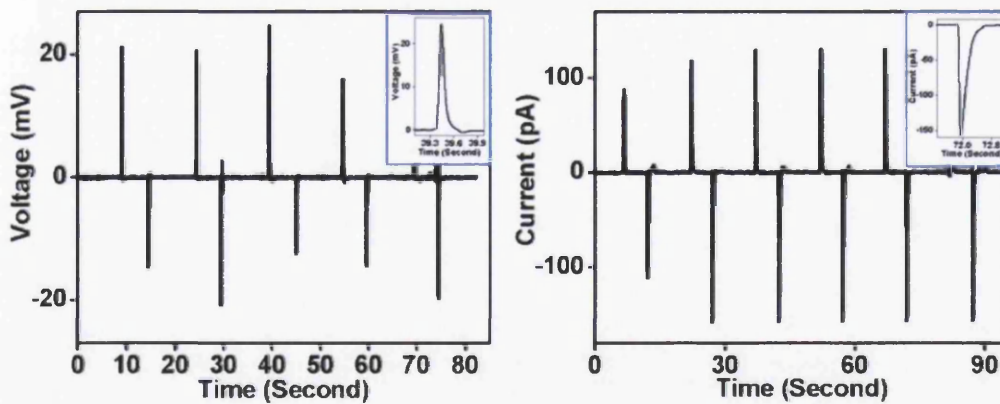
Figure 2.19 Open circuit voltage and a short-circuit current power output from deformation of the nanowire through movement of an index finger [42].

A yellow jacket was made consisting of single nanowire generators lying on the top surface. This jacket was worn by a dwarf hamster with the nanogenerators attached to the back. As the hamster moved and it's back moved forwards and backwards, the jacket with the nanowire generators attached became wrinkled and produced the same movement in the single nanowire generators. This movement of the hamster caused the deformation of the nanowires which generated an output. The hamster and the corresponding output current and voltages are shown in figure 2.20. When the hamster ran in the specially designed wheel, it produced an oscillating current and voltage output. Figure 2.20 (a) and (d) shows the variety in the output when the hamster was running at a fairly constant frequency and when the hamster was scratching. The movement when the hamster was scratching did not produce the large output seen when the hamster is running, this is to be expected as the extent to which the hamster moves is lower. Figure 2.20 (b) and (d) are enlarged views of the corresponding voltage and current. The maximum current produced was approximately 0.5nA and the voltage reached 50-100mV. The results produced are much larger than the output voltage and current generated from the movement of a human finger due to a much higher stress and strain rate.

The experiment with the hamster was extended to increase the number of single nanowire generators. The integration of four single nanowire generators raised the output voltage up to 0.1-0.15V. This increases the possibility of real applications of the single nanowire generator technology. However synchronization of these individual generators in order to produce maximum output voltage and output current needs to be carefully considered.
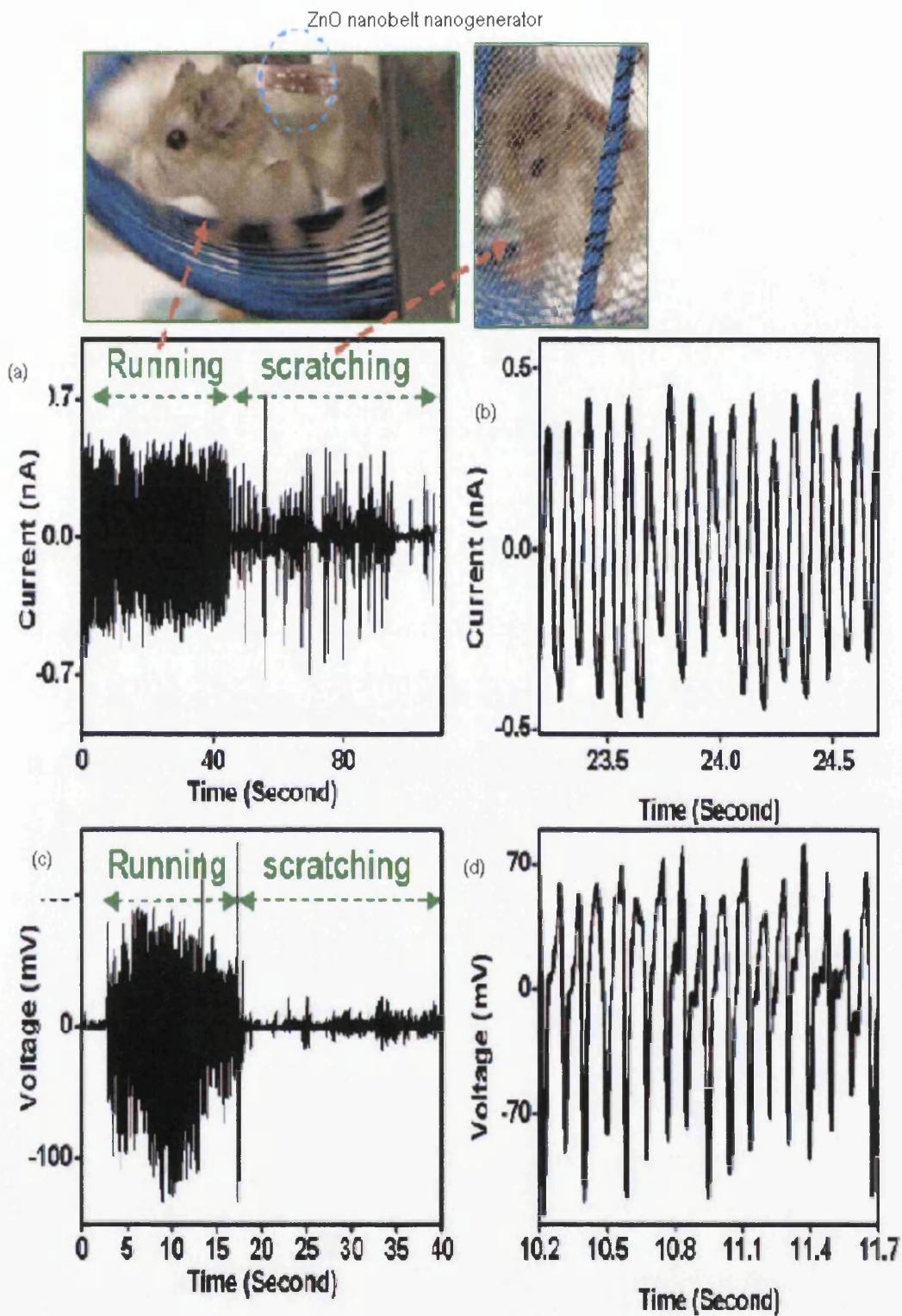
Figure 2.20 ZnO nanogenerator jacket worn on a hamster (a) current output when the hamster is running and scratching (b) enlarged view of current output (c) voltage output when hamster is running and scratching (d) an enlarged view of voltage output [5].

2.6 Comparison to Silicon Nanowires

As shown later in the results chapter, silicon nanowires were also explored and compared to zinc oxide nanowires with regards to their dielectric constant and how they behave when examined by electric force microscopy. In order to understand these results the properties of these silicon nanowires were looked at and compared to those described above for zinc oxide nanowires.

The silicon nanowires were sourced from Max Planck Institute of Microstructure Physics in Germany. The nanowires were 50-250nm in diameter and 100-400nm in length and were grown under ultrahigh vacuum in a Riber SiVa45 MBE chamber using gold as a grown initiator [43]. The nanowires were doped according to whether they were to be p-type or n-type. The p-type nanowires were doped by boron and the n-type were doped with phosphorous.

Unlike zinc oxide, silicon nanowires have an indirect band gap which limits their applications as they will be unable to function in optoelectronics [44]. Silicon nanowires have been found to be much stronger than silicon in bulk form which is often brittle and fractures easily. The atomic force microscope has been used to characterize the elasticity and many of the physical properties outlined here [45]. The Youngs Modulus has been estimated for silicon nanowires to be around 186 GPa. In response to applied force the silicon nanowires behaved in a highly non-linear manner ending in brittle fracture. Thermal conductivity for silicon nanowires were found to be more than two orders of magnitude lower than the value determined for bulk silicon. As expected as the nanowire diameter decreases the thermal conductivity also decreases which could be a direct result of an increase in surface-scattering effects. Silicon nanowires were also found to have extremely large piezoresistance effect when compared to bulk silicon. This property is very similar to that seen for zinc oxide and recently enabled research into zinc oxide piezoelectric-gated diodes. Silicon nanowires show excellent field emission properties including a low turn-on field and threshold field as well as a high field enhancement factor.

Compare the properties outline above to those described for zinc oxide and the major similarity is how the properties change by such a degree from bulk to nanowire. The Youngs Modulus of silicon nanowires is 186GPa which is over five times larger when compared to that seen for zinc oxide nanowires (38.2 GPa).

2.7 Summary

Zinc oxide is an II-IV semiconductor with a band gap of 3.37eV and exciton binding energy of 60meV. Zinc oxide is able to form many interesting and varied nanostructures such as belts, wires, rings and helixes. The growth of zinc oxide nanostructures has been widely explored and mechanisms include vapour transport either with or without the presence of a catalyst, laser ablation, template directed and wet chemical. The mechanism used to synthesise the nanostructures heavily depends upon the type of nanostructure required and the subsequent application.

Zinc Oxide nanowires exhibit intriguing and varied properties for example being able to probe nanowires mechanical properties by indentation with an AFM tip to calculate the Youngs modulus of the belt. Zinc oxide nanowires were also shown to have lasing potential when imaged by near-field scanning microscope illustrated by the areas of strong photoluminescence at the terminus of the belt.

Recent applications for the synthesised zinc oxide nanowires include nanogenerators, resonators and cantilevers. The most promising of these being nanogenerators are able to convert a variety of sources of energy for example mechanical from body movement or hydraulic from blood flow into electrical energy.

2.8 References

1. Bunn C. W., *The Lattice Dimensions of Zinc Oxide.* Proc. Phys. Soc, 1935. **47**(5): p. 835-842.

2. Wang Z. L. and Song J., *Piezoelectric Nanogenerators based on zinc oxide nanowire array.* Science, 2006. **312**: p. 242-246.

3. Wang Z. L., *Zinc Oxide nanostructures: Growth, properties and applications.* J. Phys. Condens. Matter., 2004. **16**: p. 829-858.

4. Wang Z. L., *Nanobelts, Nanowires and nanodiskettes of semiconducting oxides-From materials to nanodevices.* Adv. Mater, 2003. **15**(5): p. 432-436.

5. Wang Z. L., *ZnO nanowire and nanobelt platform for nanotechnology.* Materials Science and Engineering R, 2009. **64**: p. 33-71.

6. Li Z., et al., *Cellular Level Biocompatibility and Biosafety of ZnO Nanowires.* Phys. Chem. C: Letts, 2008. **112**: p. 20114-20117.

7. Karpina V.A.; Lashkarev C.V.; Dobrowolski V.D., K.L.I., Baturin V.A., Pustovoytov S.A., Karpenko A. J., Eremin S.A., Lytvyn P.M., Ovsyannikov V. P., and Mazurenko E. A., *Zinc Oxide analogue of GaN with new perspective possibilities.* Cryst. Res Technol., 2004. **39**(11): p. 980-992.

8. Rogers C. E., *Introduction to Coordination, solid state and descriptive inorganic chemistry.* 1994, Singapore: McGraw-Hill Inc. 172-175.

9. West A. R., *Basic Solid State Chemistry.* 2nd ed. 1999, Chichester: Wiley & Sons. 67-124.

10. Kirkham M.; Wang Z. L. and Snyder R. L., *In Situ growth kinetics of ZnO nanobelts.* Nanotechnology, 2008. **19**(445708): p. 1-4.

11. Fan Z. and Lu J. G., *Zinc Oxide Nanostructures: Synthesis and Properties.* Journal of Nanoscience and Nanotechnology, 2005. **5**(10): p. 1561-1573.

12. Wang X., et al., *Large scale synthesis of six-nanometer-wide ZnO nanobelts.* J. Phys. Chem. B, 2004. **108**: p. 8773-8777.

13. Park W., Y.G., Kim M., and Pennycook S., *ZnO nanoneedles grown vertically on Si substrates by non-catalytic vapor-phase epitaxy.* Adv. Mater, 2002. **14**(24): p. 1841-1843.

14. Ogata K., M.K., Fujita Sz., Fujita Sg., *Growth mode control of ZnO toward nanorod structures or high-quality layered structures by metal-organic vapor phase epitaxy.* J. Cryst. Growth, 2003. **248**: p. 25-30.

15. Pan Z., Dai Z., and Wang Z. L., *Nanobelts of Semiconducting Oxides.* Science, 2001. **291**: p. 1947-1949.

16. Huang M., et al., *Room temperature UV nanowire nanolaser.* Science, 2001. **292**: p. 1897-1899.

17. Li S., Lee C., and Tseng T., *Copper-catalysed ZnO nanowires on silicon (100) grown by vapor-liquid-solid process.* J. Cryst. Growth, 2003. **247**: p. 357-362.

18. Lee C., et al., *Field emission from well-aligned zinc oxide nanowires grown at low temperature.* Appl. Phys. Letts, 2002. **81**(19): p. 3648-3650.

19. Ding Y., Gao P., and Wang Z. L., *Catalyst-Nanostructure Interfacial Lattic Mismatch in Determining the shape of VLS Grown Nanowires and Nanobelts: A Case of Sn/ZnO.* J. Am. Chem. Soc., 2004. **126**(7): p. 2066-2072.

20. Gao P., Ding Y., and Wang Z. L., *Crystallographic Orientation-Aligned ZnO Nanorods Grown by a Tin Catalyst.* Nano Letts, 2003. **3**(9): p. 1315-1320.

21. Gao P. and Wang Z. L., *Self Assembled Nanowire-Nanoribbon Junction Arrays of ZnO.* J. Phys. Chem., 2002. **106**(49): p. 12653-12658.

22. Wagner R. S. and Ellis W. C., *Vapor-Liquid -Solid Mechanism of single crystal growth.* Appl. Phys. Letts, 1964. **4**(5): p. 89-90.

23. Chang P., et al., *ZnO nanowires synthesised by vapor trapping CVD method.* Chem. Mater, 2004. **16**: p. 5133-5137.

24. Jiang Y., et al., *Zinc Selenide Nanoribbons and Nanowires.* J. Phys. Chem. B, 2004. **108**: p. 2784-2787.

25. Duan X. and Lieber C., *Laser-assisted Catalytic growth of single crystal GaN nanowires.* j. Am. Chem. Soc., 2000. **122**: p. 188-189.

26. Premkumar T., et al., *Particulate assisted growth of ZnO nanorods and microrods by pulsed laser deposition.* Appl. Surf. Sci, 2009. **255**: p. 6819-6822.

27. Fan H., et al., *Template-assisted large scale ordered arrays of ZnO Pillars for optical and piezoelectric applications.* Small, 2006. **2**(4): p. 561-568.

28. Lazareck A., et al., *DNA-directed synthesis of zinc oxide nanowires on carbon nanotube tips.* Nanotechnology, 2006. **17**: p. 2661-2664.

29. Hossain M. K., et al. *Novel Sol-gel Route for the Growth of ZnO nanoparticles, nanowires and nanobelts.* in *The 2nd International Conference on Structure, Processing and Properties of Materials.* 2004. Dhaka, Bangladesh.

30. Wu J. J., et al., *Well-aligned ZnO nanorods via hydrogen treatment of Zinc Oxide films.* Adv. Funct. Mater, 2004. **14**(8): p. 806-810.

31. Sakurai M., W.Y., Uemura T., Aono M.,, *Electrical Properties of Individual ZnO nanowires.* Nanotechnology, 2009. **20**(155203): p. 6.

32. Fan Z., L.J.G., *Electrical Properties of ZnO nanowire field effect transistors characterised with scanning probes.* Appl. Phys. Lett, 2005. **86**(032111).

33. Ni H. and Li X., *Youngs Modulus of ZnO nanobelts measured using atomic force microscopy and nanoindentation techniques.* Nanotechnology, 2006. **17**: p. 3519-3597.

34. Zhao M., et al., *Nanomechanical characterisation on Zinc and Tin Oxide nanobelts.* Mat. Res. Soc. Symp. Proc., 2003. **740**: p. 19.5.1-19.5.9.

35. Zhao M., et al., *Probing Nanoscale mechanical characteristics of individual semi-conducting nanobelts.* Materials Science and Engineering A, 2005. **409**: p. 223-226.

36. Yang P., et al., *Controlled Growth of ZnO nanowires and their optical properties.* Adv. Funct. Mater, 2002. **12**(5): p. 323-331.

37. Hughes W. and Wang Z. L., *Nanobelts as Cantilevers.* Appl. Phys. Letts, 2003. **82**(17): p. 2886-2888.

38. Wang Z. L., et al., *Piezoelectric nanogenerators for self powered nanodevices,* in *Pervasive computing.* 2008. p. 49-55.

39. Qin Y., Wang X., and Wang Z. L., *Microfibre-nanowire hybrid structure for energy scavenging.* Nature, 2008. **451**: p. 809-813.

40. Wang X., et al., *Direct-current nanogenerator driven by ultrasonic waves.* Science, 2007. **316**: p. 101-105.

41. Zhou J., et al., *Flexible Piezotronic strain sensor* Nano Letts, 2008. **8**(9): p. 3055-3040.

42. Yang R., et al., *Converting Biomechanical Energy into Electricity by a muscle-movement-driven Nanogenerator.* Nano Letts, 2009. **9**(3): p. 1201-1205.

43. Ou X., K.P., Kogler R., Werner P., Gosele U., Skorupa W., Wang X.,, *Carrier Profiling of Individual Si Nanowires by Scanning Spreading Resistance Microscopy.* Nano Letts, 2010. **10**(1): p. 171-175.

44. Qu Y., L.L., Li Y., Zhang H., Huang Y., Duan X.,, *Electrically Conductive and Optically Active Porous Silicon Nanowires.* Nano Letts, 2009. **9**(12): p. 4539-4543.

45. Chen L., *Silicon Nanowires: the key building block for future electronic devices.* J. Mater. Chem, 2007. **17**: p. 4639-4643.

Chapter 3

Scanning Probe Microscopy

3.1 Introduction

The atomic force microscope (AFM) was developed approximately 5 years after the scanning tunnelling microscope. Binnig, Quate and Gerber designed the AFM with the aim of allowing the imaging of both conducting and insulating samples with the same microscope [1]. At the time, conducting samples were examined using the scanning tunnelling microscope (STM) and insulating samples were imaged using the stylus profilometer. The group extrapolated ideas from both of these imagining techniques to develop the AFM. Their results showed a lateral resolution of 30Å and a vertical resolution of 1Å. Over 20 years later vast improvements have been made to this microscope, so much so that the lateral resolution of this instrument is less than 10 nm. These improvements have allowed the imaging of biological samples in their natural environment including liquid imaging and the direct quantification of surface interactions of a variety of substances.

3.2 Theory

A schematic diagram illustrating the basic principle of AFM is shown in figure 3.1. A sharp tip is mounted at the end of a force-sensing cantilever. The cantilever can be placed at a position of interest on the sample using the light microscope. Once a suitable place of interest is found the cantilever is incrementally lowered towards the surface. As this is brought into close proximity to the sample surface, forces between the atoms of the tip and the atoms of the surface cause the cantilever to deflect.

These deflections and the type of force sensed are dependent upon the distance between the tip and the sample. At small tip-sample distances interatomic forces are dominant and consist of short range Born repulsive forces ($\leq$ 0.1nm) and long range Van der Waals forces (> 10-15nm) [2]. If the tip sample distance is significantly increased as in non-contact mode of operation (see Section 3.4.2) the Van der Waals forces decay and long range forces dominate such as electrostatic, magnetic and electromagnetic and in some cases capillary.

A laser is positioned onto the back of the cantilever, which detects changes in deflection resulting from the tip interacting with the surface. This is achieved by reflecting the laser beam on to a position sensitive photodiode (PSPD), which can measure displacements to an accuracy of less than 1nm. This signal is then sent to the feedback electronics.
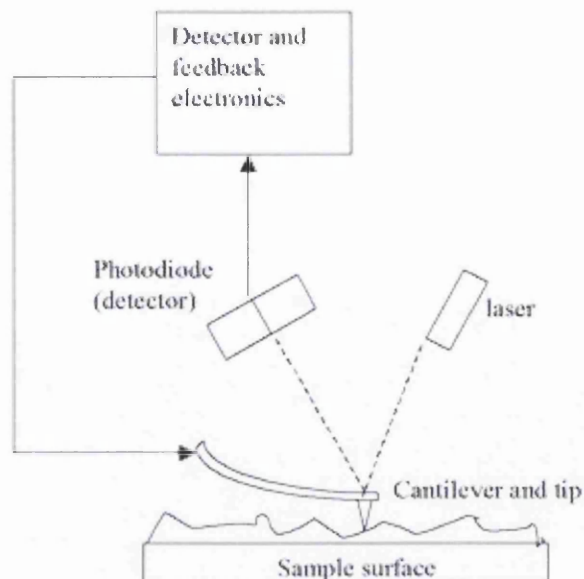
Figure 3.1 Illustration of the set-up of the Atomic Force Microscope [3].

The feedback monitors the tip-sample force and alters the z-position accordingly in order for the force to remain constant. Once the required force is reached a raster scan can start and a topographic image is produced from the data collected concerning the z position of the tip.

The Lennard-Jones potential is a mathematical simple model that describes the interaction between two uncharged molecules or atoms [4]. This can be used to help interpret AFM/EFM images by relating tip-sample interactions to the relevant forces. This is illustrated in Figure 3.2, which shows the characteristic Lennard-Jones potential shape. The figure is annotated to show the different portions of the graph associated with each mode of operation, which will be discussed later in section 3.4. The potential describes the interaction between the two neutral atoms and is attractive at long range, which could be due to Van der Waals forces of attraction. However as the tip-sample separation decreases the force becomes increasingly repulsive due to the overlapping of valence electron orbitals, which is explained by the Pauli principle of exclusion. This theory states that no two electrons in an atom can have the same four values for quantum numbers. The quantum numbers are n the principle quantum number, L angular momentum (determines the sub shell), M_l magnetic quantum number (energy shift determines the shape of the sub shell) and M_S the spin projection. An electron in an atom can differ by only one of these quantum numbers to exist. This exclusion principle explains the sharing of electrons between atoms and the electronic shell arrangement.

At tip-sample distances of a few nanometers (tapping and contact) the Van der Waals forces experienced are usually attractive between atoms on the sample and atoms at the end of the tip [2]. These forces are strong enough to give a detectable deflection of the cantilever.

For two interacting molecules the Van der Waals potential is given by

$$U_{vdw} \approx \frac{-C_1}{Z^6}$$

Equation 3.1

$C1$ is a constant whose value depends upon the depth of the energy well and the equilibrium separation of the two atoms Z is the distance between the two molecules. At these smaller separation distances the wave functions of the electrons situated in the atoms at the end of the tip overlap with the wave functions of the electrons located on the surface of the sample. The strong electrostatic repulsive forces produced are termed Born forces and the potential of these forces are determined by the equation

$$U_{born} = \frac{C_2}{Z^{12}}$$

Equation 3.2

Therefore the total intermolecular potential is

$$U = U_{born} + U_{vdw}$$

Equation 3.3

$$U = \frac{C_2}{Z^{12}} - \frac{C_1}{Z^6}$$

Equation 3.4

This equation (3.4) describes the Lennard-Jones potential. C_1 and C_2 are constants therefore it can be determined that as the radius of the atom increases the Lennard-Jones potential decreases in size. The force detected by the AFM is due to all the attractive and repulsive potentials experienced between the tip and the sample during their interaction.

Hence equation 3.4 becomes;

$$U = \frac{1}{r^{12}} - \frac{1}{r^6}$$

Equation 3.5

Differentiating equation 3.5 produces an expression for the force interaction F (eqn 3.7).

$$F = -\frac{dU}{dr}$$ *Equation 3.6*

$$F = 12\frac{1}{r^{13}} - 6\frac{1}{r^7}$$ *Equation 3.7*

Taking the second differential of equation 3.7 yields an equation determining the force gradient which is used as feedback in both non-contact atomic force microscopy (section 3.4.2) and electric force microscopy (section 3.5).

$$\Delta F \propto \frac{d^2U}{dr^2}$$ *Equation 3.8*

$$\Delta F = 156\frac{1}{r^{14}} - 42\frac{1}{r^8}$$ *Equation 3.9*

The results for the potential (u), the force (F) and the force gradient (ΔF) can be plotted on the same graph of force against tip-sample separation.
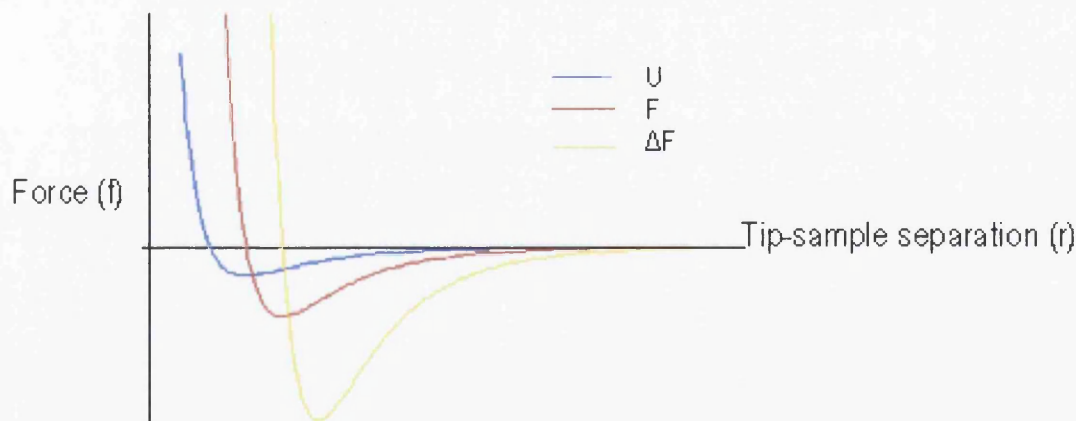
Figure 3.2 Force (F) against tip-separation(r) for potential, force and the force gradient of the interaction between the atoms of the tip and the atoms of the sample during AFM.

By examining the force gradient graph it can be determined which points illustrate the different modes of contact (figure 3.3). The steep initial slope of the graph with a positive force gradient and a small tip-sample separation is indicative of contact mode and illustrates

repulsive force acting. Below the tip-sample separation axis, when the force gradient is negative it is said that an attractive force is acting between the tip and the sample. It is this portion of the graph which shows non-contact mode where the tip-sample separation is at its greatest. The intermittent contact or tapping mode covers both of these areas illustrating the movement of the tip as it starts from a large tip-sample separation to a very small separation and back again.
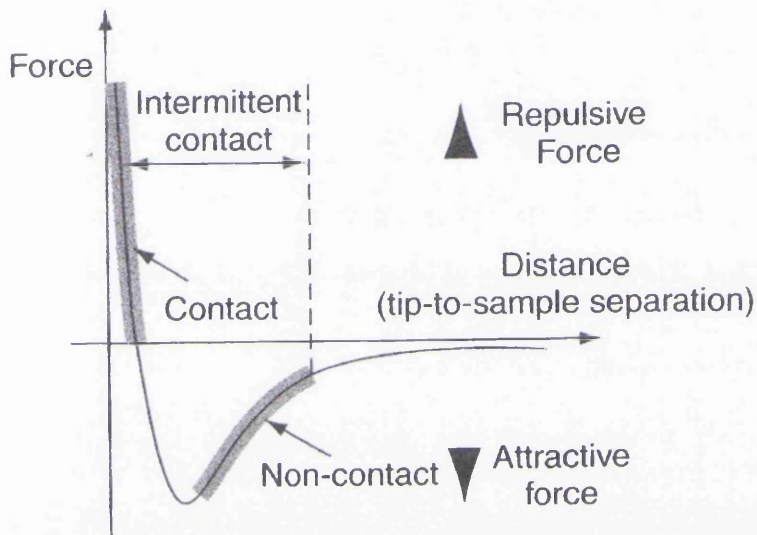
Figure 3.3 Lennard-Jones Potential showing the different modes of operation of the microscope and the corresponding force [5].

3.3 Tips and Cantilever

In the early development of AFM, tips were produced by hand from a thin metal wire, which were electrochemically etched to a sharp point. This is obviously not a viable synthesis route to produce tips on mass [6]. Cantilevers are micro fabricated on silicon chips (or silicon nitride) chips and are sourced from an external supplier. The cantilevers themselves can vary in size (and shape) depending on the application, but are typically <300μm long, <50μm wide and < 4μm thick. Tips are situated on the underside of the cantilever and can vary greatly in terms of hardness and aspect ratio. The mechanical properties of the cantilever are a very important consideration in the operation of the microscope. They are defined by the dimensions (width, length and thickness) as well as the geometry and the type of material used to make the cantilever.
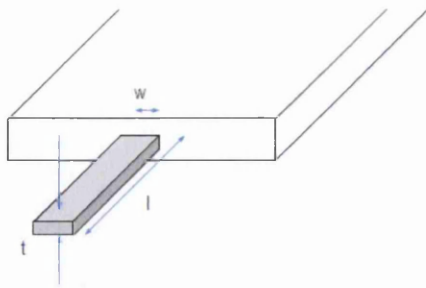
Figure 3.4 Schematic of a beam-shaped cantilever with width (w), thickness (t) and length (l).

The beam shaped cantilever as illustrated in figure 3.4 is the fundamental type of cantilever as is treated as a classical one-dimensional fixed-free beam and the behaviour can be described but the analogy of a spring, hence the spring constant of the cantilever is given by

$$k = \frac{E}{4}\left[\frac{wt^3}{l^3}\right]$$
Equation 3.10

Where k is the spring constant, E is the Young's modulus and w, t and l are the dimensions width, thickness and length respectively. The resonant frequency of a spring is determined by equation 3.12, taking into account the density, ρ and the spring mass m.

$$f_{res} = \frac{1}{2\pi}\sqrt{\frac{E}{\rho}\frac{t}{l^2}}$$
Equation 3.11

Therefore
$$f_{res} = \frac{1}{2\pi}\sqrt{\frac{k}{m}}$$
Equation 3.12

The parameters outlined by the equations above are used to manufacture cantilevers with a variety of spring constants and resonant frequencies depending upon the type of intended application. The exact cantilever and tip used in the experiments outlined in this work are discussed in chapter 5.

In order for the tip to respond quickly and efficiently to changes in the surface the cantilever must have a relatively high resonant frequency. Also it is beneficial for the cantilever to be

flexible in order to withstand scanning without damaging the tip or the sample. To achieve this, the cantilever must have a low spring constant in the order of 0.1 Nm^{-1}. From equation 3.12 it can be determined that for the cantilever to have both a low spring constant and a high resonant frequency the mass must also be extremely small.

The resolution of an AFM image is ultimately determined by the radius of curvature of the tip. Bustamante and Keller determined a geometric model of the tip resolution as outlined in figure 3.5 [7]. Two sharp peaks are separated by a certain distance, d. The tip has been assumed to be parabolic in shape and with a terminal radius of R. The small depression between the images of the tips is labelled Δ Z and the two spikes are resolved if ΔZ is greater than the instrumental noise in the Z direction.
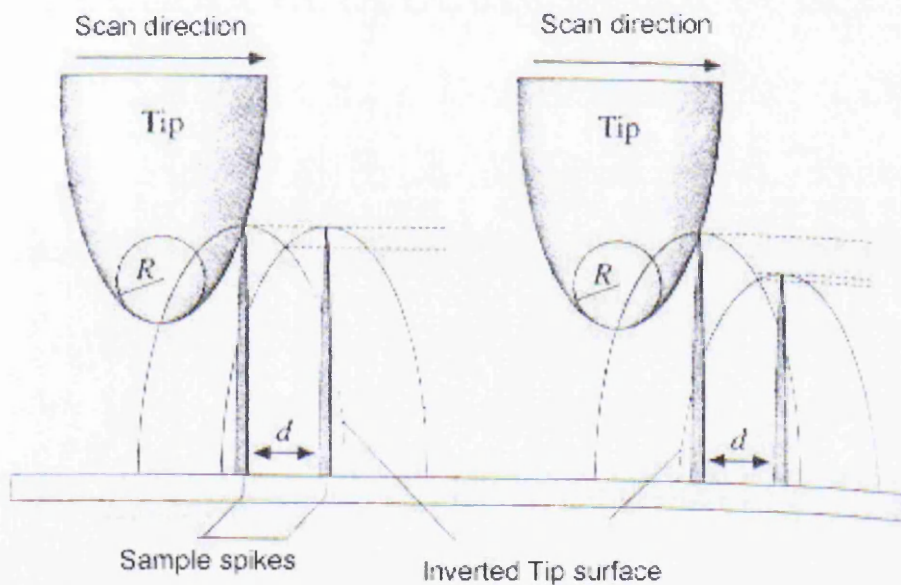
Figure 3.5 The resolution capabilities of a topographic image with R, radius of the tip and d, the distance between peaks on the samples surface [6].

$$d = 2\sqrt{2R(\Delta Z)}$$

<div align="right">*Equation 3.13*</div>

Where d is the minimum separation at which the spikes are resolved, R is the radius of tip and ΔZ is the minimal detectable depression. For example if the tip has a radius of 4nm and a minimum detectable ΔZ of 0.5nm the resolution can be calculated to be 3.5nm.

The spikes in figure 3.5 are not the same height hence the difference in this height, Δh, must also be taken into account.

$$d = \sqrt{2R}\left[\sqrt{Z} + \sqrt{\Delta Z + \Delta h}\right]$$ *Equation 3.14*

The theory put forward by Bustamante and Keller does not, however, take into account the affect of the compression and deformation of the tip and the sample.

3.4 Modes of operation

There are three modes of operation of the AFM are illustrated in figure 3.6. The application of the different techniques depends heavily upon the sample to be imaged [8]. A soft sample would be better imaged in non-contact mode so as to not damage and lose surface information. A harder sample would be able to withstand tapping or even contact modes.
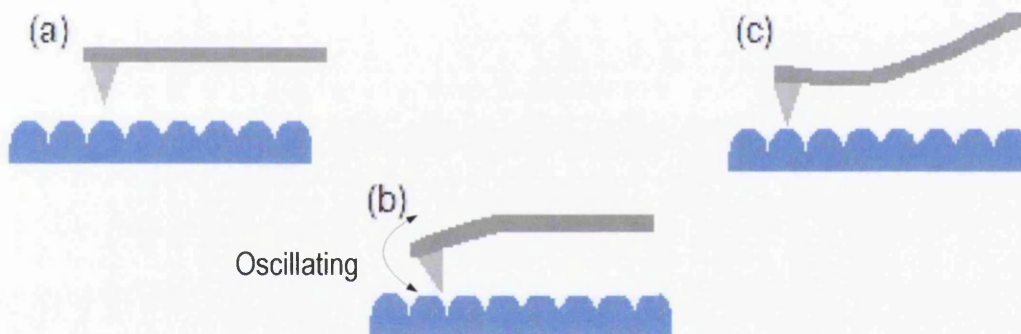
Figure 3.6 Modes of operation of AFM (a) non-contact mode, (b) tapping mode and (c) contact mode.

3.4.1 Contact Mode

Contact mode involves the tip making a constant soft physical contact with the surface of the sample [8]. The deflection of the cantilever produced by the interaction between the tip and the surface is proportional to the force applied to the cantilever, which is predetermined by the user. The tip is rastered across the surface and the feedback mechanism alters the height of the tip to keep the applied force constant. The majority of contact mode AFM is conducted in air, where the capillary forces can affect the tip whilst scanning. In air, the sample surface is covered with a thin layer of absorbed gases of water vapour and nitrogen. When the tip touches the surface, a meniscus forms and the cantilever is pulled towards the surface due to surface tension. This capillary force can be as great as 100mN. To alleviate this affect, a

sample can be imaged when fully immersed in liquid or by scanning in a UHV environment. The main disadvantage of using contact mode is that if the sample is made of softer material then damage will be caused by the tip rastering across the surface.

3.4.2 Non-contact Mode

Non-contact mode requires the tip to be a set distance approximately 50-150 Å away from the surface and the cantilever is driven to vibrate at a high frequency (f) [2]. There are two possible methods of operating in non-contact mode, Frequency Modulation and Amplitude Modulation. In frequency modulation technique the resonant frequency (f_0) of the cantilever is slightly shifted due to the interaction between the tip and the sample as illustrated in the diagram.
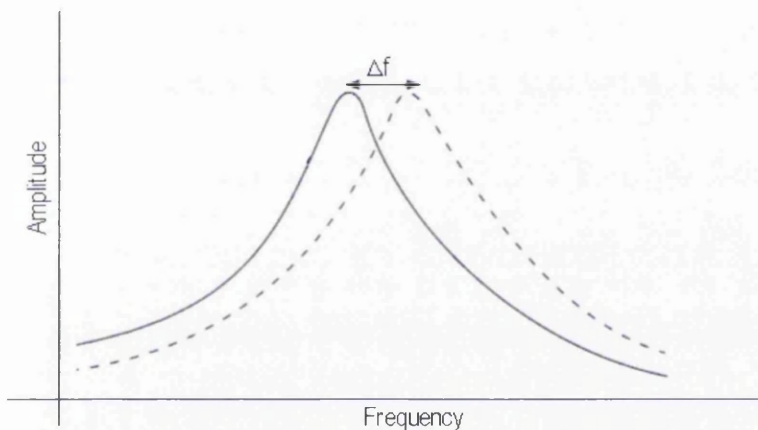
Figure 3.7 Plot of amplitude and frequency illustrating the frequency shift when operating the AFM in non-contact frequency modulation mode.

Δf is directly proportional to the gradient of the force of interaction between the tip and the sample. This frequency shift can be measured and from this the interacting force can be determined by integration. Amplitude modulation describes the gradient force between the tip and the sample is directly proportional with the amplitude of the cantilever and the phase of the deflected signal is monitored with the assistance of the lock-in amplifier. In both of the cases described the feedback signal is used to keep either the frequency or the amplitude of the cantilever constant.

The attractive Van der Waals forces acting between the tip and the sample are detected and a topographic image is obtained. The forces experienced by the tip in this mode are much weaker than the forces experienced by the tip in contact mode, which would be expected. As

discussed previously the fluid layer naturally occurring on the sample is much thicker than the reach of the Van der Waals forces. This increases the difficulty in imagining the true surface features.

This technique relies upon the detection of van der Waals forces of attraction. The majority of this force is due to dispersion forces, induced dipole-induced dipole interactions [9]. For a neutral atom at an instantaneous time a dipole is present. This dipole influences a nearby neutral atom inducing a dipole. The resulting interaction produces an attractive force between the two atoms. In the case of scanning the sample, an interaction occurs between the end atom of the tip and the atoms on the surface of the sample. The force of van der Waals (F) is described in equation 3.15 as being inversely proportional to the distance of the atom from the surface of the sample (D).

$$F \propto \frac{1}{D^4}$$
<div align="right">*Equation 3.15*</div>

Van der Waals forces are involved in adhesion, surface tension, wetting and the strength of solids. The AFM measures the force of this interaction between the end atom of the cantilever and the atoms on the surface.

3.4.3 Tapping Mode
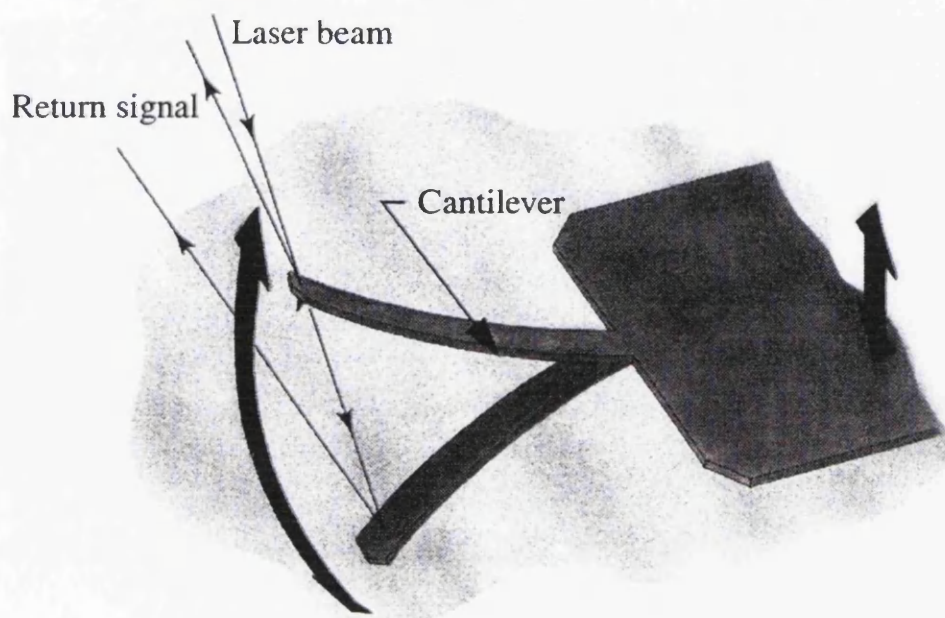
Figure 3.8 Cantilever deflection in tapping mode AFM showing the laser signal reflection off the cantilever [8].

Tapping mode is a compromise between contact and non-contact modes and allows the imaging of a vast array of samples. This mode overcomes problems associated with friction, adhesion and electrostatic forces. This occurs because the tip-sample adhesion forces are greatly reduced in tapping mode. The cantilever oscillates near the resonance frequency with large amplitude. The resonance frequency is the frequency of free vibrations and can range from 50 KHz to 500 KHz. As the cantilever approaches the surface of the sample, the tip will lightly contact the surface in a tapping motion. The intermittent contact between the sample and the surface will cause a reduction in the amplitude of oscillation due to ionic repulsion and the loss in energy. The data collected from this reduction in amplitude is used to provide information on surface features.

3.5 Electric Force Microscopy

Electric Force Microscopy (EFM) can also be termed Scanning Conductance Microscopy, Electrostatic Force Microscopy or Kelvin Probe Microscopy but in this work this technique will be referred to as EFM. EFM is based on a 2-pass lift mode where the same section of the sample is imagined twice. The sample is initially scanned in tapping mode by the AFM (section 3.4.3) to produce a topographical image of the substrate [8]. A topography scan must be completed first and be of good quality in order to determine the optimum lift height, otherwise the tip will crash into the surface. The scanning is then stopped and the tip is raised to a user set height above the sample, normally in the range of 5-100nm (figure 3.9). A large lift height is better in order to pull the tip from the sample and prevent sticking. Determining the lift height is very difficult as the vertical and lateral resolution depends upon the tip sample distance, the lower the tip the higher the resolution. The sample is then rescanned at this preset height, termed interleave scan, and the electrostatic forces causing a deflection in the cantilever are measured.
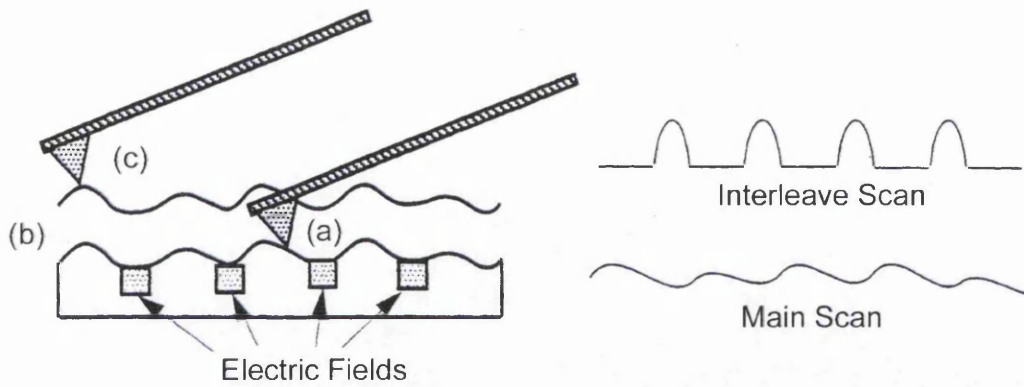
Figure 3.9 Illustration of the topographic and interleave scans. (a) representation of the topographical scan, (b) Cantilever lifts to the user-set height and (c) cantilever rescans the sample at this preset height recording the electronic influences [8].

During imaging the cantilever is vibrated by the piezoelectric element close to the resonant frequency. This frequency changes with a change in the force gradient as shown in figure 3.10.
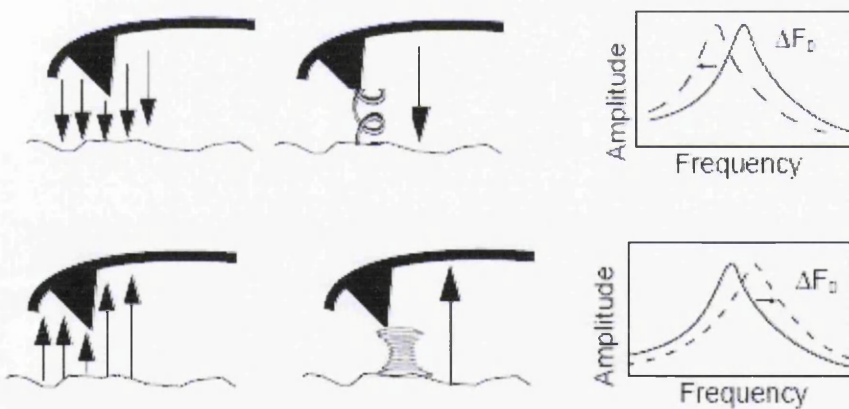
Figure 3.10 Illustration of the effect of changes in force gradients upon the cantilevers resonant frequency [8].

Figure 3.10 (a) describes the attractive forces between the tip and the sample make the cantilever softer and hence reducing the resonant frequency as shown in the amplitude-frequency graph. Alternatively in 3.10 (b) the cantilever experiences repulsive forces, making the cantilever harder and thus increases the resonant frequency.

These changes in the resonance frequency of the cantilever can be detected by phase detection, frequency modulation or amplitude detection. When the changes are detected by

either phase or amplitude detection the feedback is turned off as shown in figure 3.11 where the amplitude and phase signals by-pass the servo controller. The drive signal oscillates the cantilever at a constant frequency monitoring any changes in amplitude or phase to generate a scan. For frequency modulation the difference between the phase of the cantilever oscillation and the phase of the drive signal is monitored. The preferred method is phase detection as the response is faster to changes in tip-sample interactions and they are also less susceptible to height variations on the surface [10].
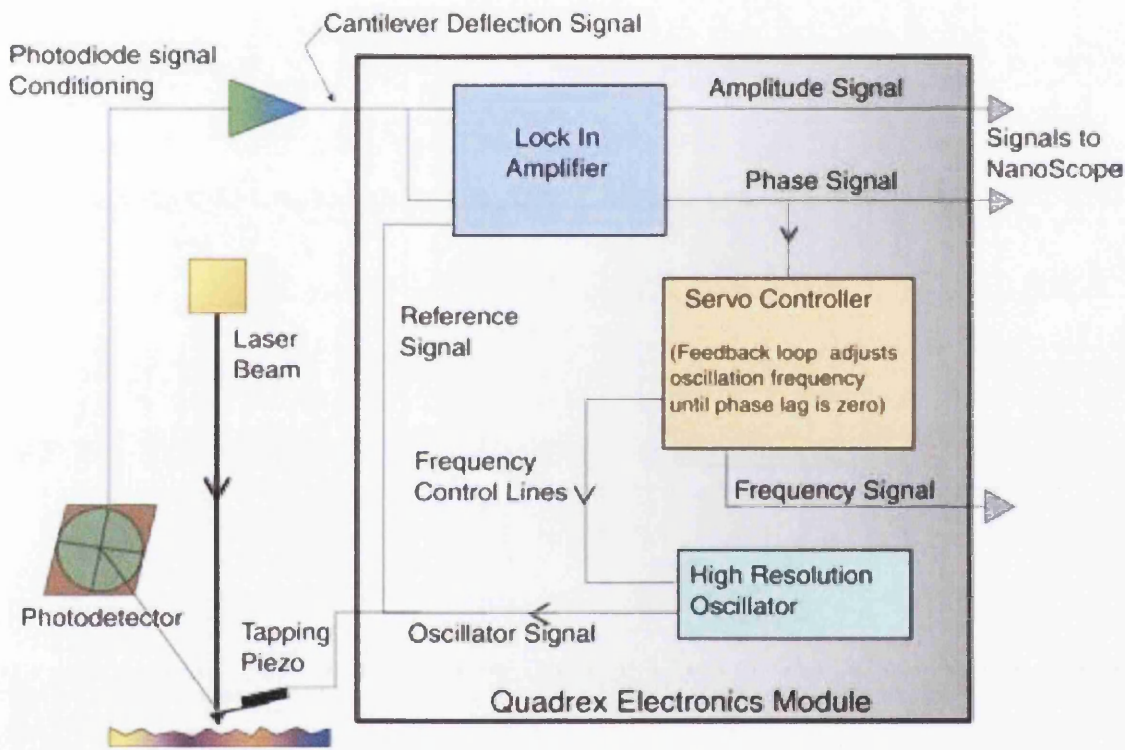
Figure 3.11 Feedback signal for the electronics module using the electric force microscopy technique [10].

The ideal sample to imagine using EFM must have large contrasts in the force gradient due to material differences or sample regions of varying potential [11]. The sample must also be fairly smooth as topographical features will appear in the image, and they heavily influence the local force gradients. Also shape features of the sample concentrate the local force gradient producing false and misleading results.

In order to overcome the influence of topographical features on local force imaging a voltage can be applied across the tip or the sample. Many research groups have chosen this route and apply a voltage by biasing the tip with a desired voltage and contacting the surface for a

few seconds. This charges the surface at the point of contact, which is then subsequently imaged.

The cantilever and the metallic tip can be modelled as a harmonic oscillator of mass m and spring constant k.

$$F = -kx$$

Equation 3.16

And $$F = ma$$

Equation 3.17

Therefore $$ma = -kx$$

Equation 3.18

$$m\frac{d^2x}{dt^2} = -kx$$

Equation 3.19

If as in the case for EFM, the harmonic oscillator is forced to oscillate by an applied external driving force then the equation 3.24 will become

$$m\frac{d^2x}{dt^2} = -kx + F(t)$$

Equation 3.20

The applied force is said to be oscillating and is expressed as

$$F(t) = F_0 Coswt$$

Equation 3.21

3.5.1 Recent Literature using EFM imaging technique

Electric Force Microscopy has been used to image a variety of samples including DNA [12-14] and Proteins [15, 16] and non-biological including thin films [17-19] carbon nanotubes [14, 20, 21] and silicon nanoparticles [22]. Zdrojek et al used EFM to imaged carbon nanotubes (CNT) both before and after charging [20]. The nanotubes were charged by contacting the Pt-Ir coated cantilever, which was bias with between -2V and -12V, with the nanotubes. The contact with the tube was determined by reducing the z distance until the minimum is tuned to reach a permanent contact regime. The recorded EFM data consists of the cantilever frequency shift which is induced by electrostatic forces acting on the tip from the surface (figure 3.12). In the results shown the uncharged carbon nanotubes appear as dark features on a relatively light background and when the nanotubes were negatively charged they appeared as bright features.
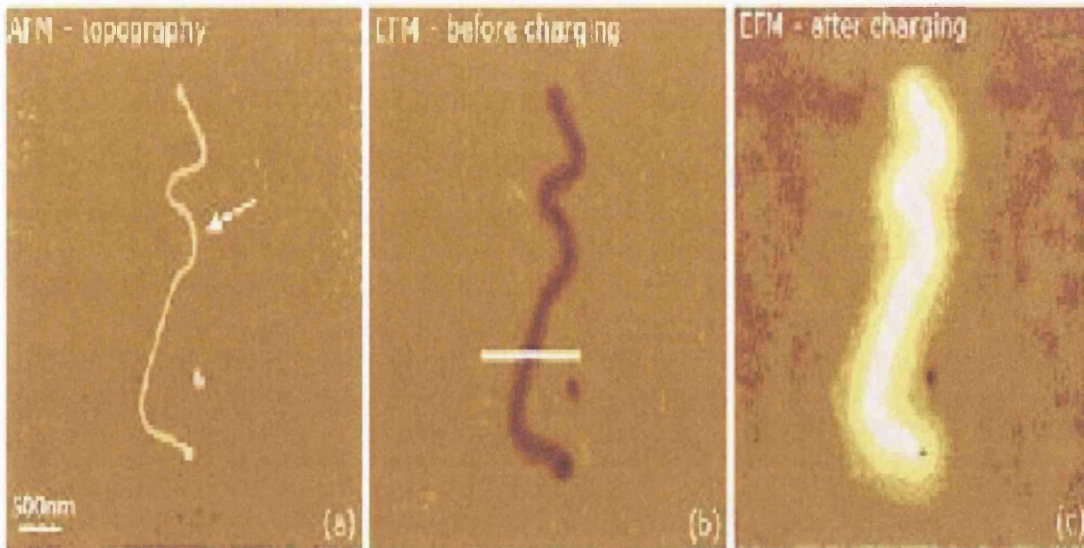
Figure 3.12(a) Topography image of carbon nanotubes, (b) EFM image of carbon nanotubes before charging and (c) EFM image of carbon nanotubes after charging clearly showing the nanotubes brighter than before [20].

It is important to note that the EFM images shown in figure 3.12 have a lower spatial resolution when compared to the topographical image obtained. However the images clearly show a difference between the carbon nanotube and the silicon dioxide substrate. It is also evident that the charging of the carbon nanotube through contact with the tip was successful.
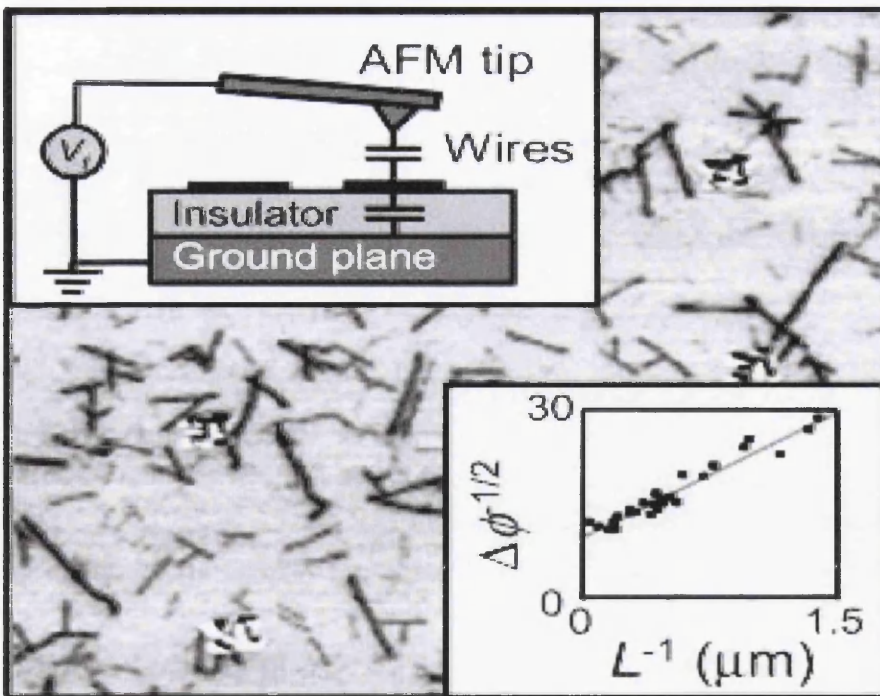
Figure 3.13 (Upper insert) AFM experimental set-p, (main panel) SCM image of SWNT's on silicon surface, (lower insert) Plot of conductance against tube length [14].

EFM has also been utilised to examine the difference in conductance between single walled carbon nanotubes and λ-DNA and to determine the length scales of detectible nanotubes [14]. The conductance was probed at length scales as small as 400nm and as this paper illustrates this can be reduced further by altering the samples geometry. Figure 3.13 (a) shows the experimental set-up of the AFM with the grounded silicon wafer and the nanotubes on top of the silicon dioxide insulating layer and the sample was scanned using a silicon AFM tip. Figure 3.13 (b) shows an EFM image, taken at a lift height of 30nm, of individual single walled carbon nanotubes as dark lines on a lighter background. The change in colour shows a shift in the phase. Comparing these EFM images to topographical images which were simultaneously obtained showed the darker lines occur over nanotubes and that shorter tubes appeared fainter than longer ones.

The behaviour observed can be examined quantitatively by considering the tip, nanotube and silicon as capacitor elements. A voltage is applied between the tip and the silicon substrate and the electrostatic forces on the tip alter the frequency of the cantilever f and the phase lag ø. When the tip is far from a nanotube the electrostatic forces are independent of the horizontal displacement of the tip, hence phase ø takes a position independent background value of ø$_0$. However when the tip is over a nanotube, the charge modulation produces an additional electrostatic tip-sample force. The magnitude of these forces and the phase is described by the electric field between the tip and the nanotube. The electric field is dependant upon the division of the voltage applied to the tip (V$_t$) between the tip-tube capacitor and the tube-ground-plane capacitor.

Using a capacitive voltage divider, the tip-tube voltage V_{tt} is given by equation 1 where V_t is the applied voltage, C_0 capacitance per unit length of the nanotubes, L is the tube length and C_{tt} the tip-tube capacitor.

$$V_{tt} = V_t \frac{C_0 L}{C_0 L + C_{tt}}$$

Equation 3.22

Treating the cantilever as a harmonic oscillator and considering the addition of the electrostatic energy $\frac{1}{2} C_{tt} V_{tt}^2$ to its mechanical energy yields the result that

$$(\phi - \phi_0) \approx \frac{Q}{2k} \frac{d^2 C_{tt}}{dz^2} V_{tt}^2 \qquad \qquad \textit{Equation 3.23}$$

$$\frac{Q}{2k} \frac{d^2 C_{tt}}{dz^2} V_{tt}^2 = \frac{Q}{2k} \frac{d^2 C_{tt}}{dz^2} V_t^2 \frac{C_0 L}{C_0 + L^{-1} C_{tt}^2} \qquad \textit{Equation 3.24}$$

Q is cantilever quality factor, k is the spring constant and z is the vertical deflection of the cantilever.

Rearranging the above equation gives

$$(\phi - \phi_0)^{-1/2} = a + bL^{-1} \qquad \qquad \textit{Equation 3.25}$$

$$a = \left(\frac{Q}{2k} \frac{d^2 C_{tt}}{dz^2} \right)^{-1/2} V_t^{-1} \qquad \qquad b = a \frac{C_{tt}}{C_0} \qquad \qquad \textit{Equation 3.26}$$

The equations above indicate the plotting $(\phi - \phi_0)^{-1/2}$ against L^{-1} for tubes of varying length would give a straight line. This linear behaviour indicates that as the length of the tubes increases so does the difference in phase. This would explain why shorter wires appeared fainter in phase images. The final result indicates that plotting $(\phi - \phi_0)^{-1/2}$ versus L^{-1} for tubes of different lengths should give a straight line with gradient equal to b and the intercept being a. The result is plotted in figure 3.14 (c), which illustrates this linear behaviour so, as $(\phi - \phi_0)^{-1/2}$ becomes larger as L^{-1} also increases. This result would explain why shorter tubes give fainter features in the phase image (figure 3.14 (b)).

Previous work on charging nanoparticles have resulted in low retention times ranging from a few minutes up to several hours [22]. These retention times will need to be increased in order for charged nanoparticles to have any practical applications. In this case EFM was ultilised to image the sample topography, inject charge into individual nanoparticles and also to detect the amount of stored charge in the nanoparticles.
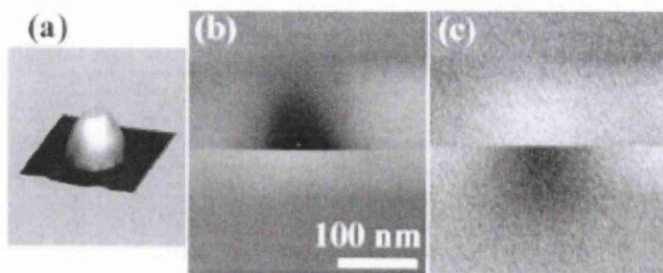
Figure 3.14 (a) topographical scan of 45nm high silicon nanoparticle (b) results after injection of +6V with the higher scan using a tip bias of -2V and the lower scan using a tip bias of +2V (c) Silicon nanoparticle after injection of -6V with the same scanning routine as in (b)[22].

In order to inject charge into individual nanoparticles the EFM tip was located above the desired nanoparticle. The tip oscillation is set to zero until permanent contact is made between the nanoparticle and the tip. The tip is then biased whilst in contact for approximately a minute. The tip is then brought back up to the original scanning amplitude and setting the bias to zero. As figure 3.15 shows the silicon nanoparticle was injected with +6V bias for a minute. The lower image in 3.15(b) shows the scan obtained from scanning the nanoparticle with +2V biased tip and the upper image is the scan obtained from scanning at a tip bias of -2V. The result shows a contrast between the images which would indicate that the nanoparticle has been charged as uncharged particles are normally insensitive to the change of sign of the scanning tip. In order to explore this concept further the nanoparticle was injected with an opposite bias charge (-6V) and the same scanning technique was used. As figure 3.15(c) illustrates the nanoparticle experiences the same sensitivity to the change in bias of the scanning tip. The discharging characteristics of the nanoparticle was examined by monitoring the EFM signal as a function of time for an individual particle which had been charged with a +12V bias for one minute. The nanoparticle was then scanned with a tip bias of +6V and the same line scan was continuously recorded so that the y-axis corresponds to time in both the topographical and EFM scans. The results indicated that the nanoparticle discharged over the time to complete the scan. This charge leaking was attributed to the tunnelling through the native silicon oxide layer of the underlying substrate.

3.6 Summary

AFM allows the imagining of biological and non-biological samples irrespective of the sample's conductivity. AFM can be operated in liquid which allows the exploration of biological samples in the natural environment and it can observe conformation changes in real time. The AFM can be operated in contact, non-contact and tapping mode. The choice of mode is heavily dependent upon the type and fragile nature of the sample. The development of the AFM has lead to the ability to not only image previously unseen substrates but also be able to manipulate individual atoms/molecules. This ability to manipulate molecules brings the nanoscience world closer to bottom-up assembly of devices.

The AFM is a versatile imaging tool which can use many techniques such as EFM and SCM. Each tool has an optimum use. EFM to image conducting samples, to record the charging and discharging of nanoparticles and to explore local charges. SCM is more useful in imagining samples such as MOSFETS, with excellent detail.

3.7 References

1.   Binnig G., Q.C.F., and Gerber Ch., *Atomic Force Microscope.* Phys. Rev. Letts, 1986. **56**(9): p. 930-933.

2.   Dragoman M., a.D.D., *Nanoelectronics Principles and Devices.* 2009, Norwood MA: Artech House Inc.

3.   [cited; Available from: www.edinformatics.com/nanotechnology/atomic_force_microscope.htm.

4.   Lennard-Jones J. E., *Cohesion.* The Proceedings of the Physical Society, 1931. **43**(240): p. 461-482.

5.   Kelshall R., H.I., and Geoghegan M., , *Nanoscience and Technology.* 2005, John Wiley & Sons: London UK. p. 32-54.

6.   Busham B., *Handbook of Nanotechnology.* 2004, Springer-Verlag Berlin Heidelberg: Berlin, Germany.

7.   Bustamante C., a.K.D., *Scanning Force Microscopy in Biology.* Phys Today, 1995. **48**(12): p. 32-38.

8.   Instruments, D., *Dimension 3100 Series SPM instruction manual.* 1998, Santa Barbara, California USA.

9.   Israelachvili J., *Intermolecular and Surface Forces (2nd Ed).* 1992, Academic Press: London.

10.   Serry F. M., et al. *Electic Force Microscopy, Surface Potential imaging and Surface Electric modifications with the AFM.* Veeco Manual 2004 [cited; Available from: http://www.veeco.com/pdfs/appnotes/AN27_EFMSurfPot_260.pdf.

11.   Melin T., et al., *Electric force micrcoscopy of individually charged nanoparticles on conductors: An analytical model for quantitative charge imaging.* Phys. Rev. B, 2004. **69**(035321): p. 1-8.

12.   Heim T., M.T., Deresmes D., Vuillaume D.,, *Localisation and delocalisation of charges injected in DNA.* Appl. Phys. Lett, 2004. **85**(13): p. 2637.

13.   Jeon D., K.C., Son J., Lee N., Kang C., and Kim Y.,, *Electrostatic Force Microscopy of Metallic ion-intercalated DNA.* Jpn. J. Appl. Phys, 2006. **45**: p. 513-514.

14.   Bockrath M., M.N., Shepard A., Tinkham M., Gurevich L., Kouwenhoven L., Wu M., and Sohn L., *Scanned conductance microscopy of carbon nanotubes and DNA.* Nano Letts, 2002. **2**(3): p. 187-190.

15.   Oh Y. J., et al., *Nanoscale observation of local bound charges of patterned protein arrays by scanning force microscopy.* Nanotechnology, 2008. **19**(365302): p. 5.

16.   Choi J., N.Y., Lee B., Ahn D., and Nagamune T.,, *Charge trap in self-assembled monolayer of cyto chrome b562-green fluorescent protein chimera.* Current Applied Physics, 2006. **6**(4): p. 760-765.

17.   Olbrich A., Ebersberger B., and Boit C., *Conducting atomic force microscopy for nanoscale electrical characterisation of thin SiO2.* Appl. Phys. Lett, 1998. **73**: p. 3114.

18.   Cho S., G.S., Sabuktagin S., Reshchikov M., Johnstone D., and Morkoc H.,, *Surface band bending in as grown and plasma-treated n-type GaN films using surface potential electic force microscopy.* Appl. Phys. Lett, 2004. **84**: p. 3070.

19.   Bridger P. M., B.Z.Z., Piquette E. C., and McGill T.C.,, *Measurement of induced surface charges, contact potentials, and surface states in GaN by electric force microscopy.* Appl. Phys. Lett, 1999. **74**: p. 3522.

20.   Zdrojek M., M.T., Diesinger H., Stievenard D., Gebicki W., and Adamowicz L., *Charging and discharging processes of carbon nanotubes probed by electrostatic force microscopy.* J. Appl. Phys, 2006. **100**(114326): p. 1-10.

21.   Yaish Y., P.J.R.S., Sazonova V., Brink M., McEuen P.,, *Electrical Nanoprobing of*

Semiconducting Carbon Nanotubes using an Atomic Force Microscope. Phys. Rev. Lett, 2005. **92**(046401): p. 4.

22. Melin T., Deresmes D., and Stievenard D., *Charge injection in individual silicon nanoparticles deposited on a conductive substrate.* Appl. Phys. Letts, 2002. **81**(26): p. 5054-5056.

Chapter 4

Electronic Devices and

Chemical Sensors

4.1 Introduction

Moores' Law describes the trend in integrated circuitry where the number of transistors doubles approximately every two years [1]. However, this trend, which has continued for four decades, will eventually reach a limit whereby the fundamental principles at the nanoscale will control and potentially bring a halt to this trend.
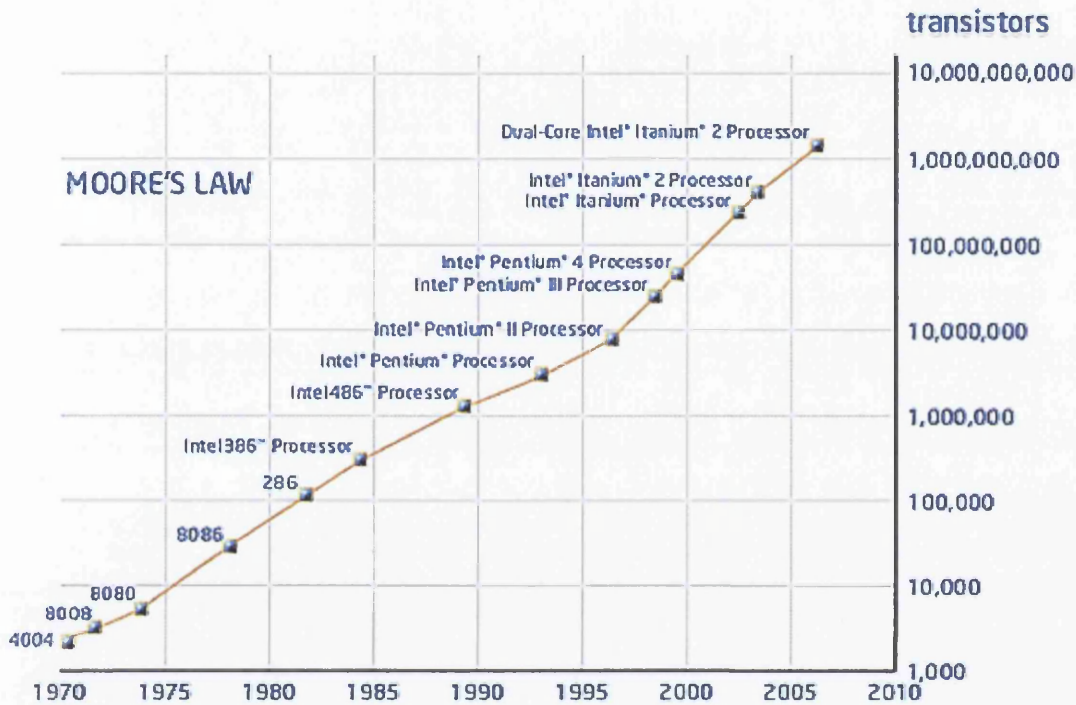
Figure 4.1 Graphical representation of the exponential growth of the density of components in integrated circuits [2].

Moore described the future of integrated electronics in his ground breaking paper in published in Electronics journal in 1965 [3]. He foresaw the advancement of home computers, automatic controls in cars and personal portable communication equipment such as mobile phones and palmtops. He envisaged more powerful computers, manufactured at lower cost and faster turn around. The microelectronics world at the time was focused on miniaturising electronics equipment to achieve increasingly complex electronic function whilst being smaller and lighter than previous systems.

Moore predicted the exponential growth of the density of components contained in integrated circuits for the next 10 years as illustrated in Figure 4.1. Throughout the academic world it was not conceived that this trend would continue for 40 years after Moore made his initial prediction.

However it is not expected to maintain its relevance past the next 10-15years due to the ultimate limits of fundamental physics down at the nanoscale. Moore touched upon the complex issue of heat dissipation from microelectronics; he suggested that as integrated circuits were two dimensional, a surface is available for cooling. However recent research has suggested heat dissipation along with fundamental physics will be the limiting factor in the growth of integrated circuits. The limits on scalability also encompass effects such as device cross talk and material property limits. Device cross talk occurs when the separation between devices reaches ~ 100Å and electrons can tunnel from one device to a neighbouring device. This issue is likely to have more influence in the future as the packing density increases and the distance between adjacent devices become smaller and smaller. Nanomaterials no longer posses the properties of the bulk material and are now surface and interfaced dominated. More recently the focus has been on manufacturing nanoscale electronic devices using techniques such as electron beam lithography, photolithography, and etching. Current research has included field effect transistors (FET) and metal oxide semiconductor field effect transistor (MOSFET) utilising a range of semiconducting materials but the majority still contain silicon as the base material.

The following chapter describes the arrival and development of the field effect transistor into nanowire devices. The massive potential application of this new range of electronics is in chemical sensing. This could impact on a variety of different industries ranging from chemical to environmental to personal for example smoke detectors and breathalysers.

4.2 Field Effect Transistors

In 1925 Lilienfeld patented a semiconductor device which used a gate electrode [4]. He described how the gate electrode would control the flow of current and he was fully aware of the practical applications of his device [5]. Lilienfelds device structure was not clear in his first patent however in later patents the device was described as using a dielectric layer of thickness ~10^{-5}cm which insulated the metal gate electrode from the semiconducting copper sulphide channel. This design provided high input impedance. It can be determined that the devices illustrated by Lilienfeld are surface controlled field-effect transistors which are similar to ones produced later improved by advancements in masking and epitaxial growth techniques.

The transistor as it is known today was developed in Bell Laboratories by Bardeen, Brattain and Shockley in 1947 [2]. They were awarded the Nobel Prize in 1956 for this work. The transistor was envisaged to be a replacement for bulky and often inefficient vacuum tubes and mechanical relays. The initial device produced results which were discouraging and found that only 10% of the induced charge was effective in altering the conductance. Shockley continued his efforts and produced a theoretical report describing how the majority carriers are altered by changing the thickness of a conducting channel by narrowing or widening the p-n junction depletion layer [5].
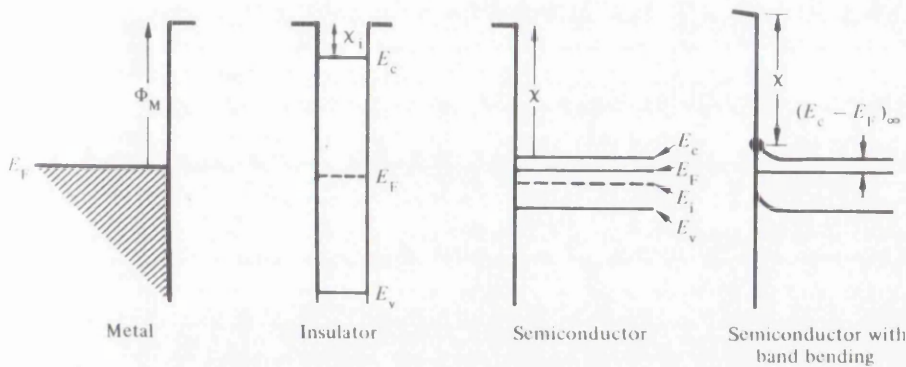
Figure 4.2 Energy band diagrams for metal, insulator and semiconductors [7]

To determine the internal condition of the field effect transistor under static biasing restrictions the energy band diagram of all materials involved must be examined thoroughly. Figure 4.2 illustrates the energy band diagrams for the separate components of the transistor. The vertical termination line indicates the surface and the horizontal line at the top of each diagram implies the vacuum level. The vacuum level describes the minimum energy an electron must possess to completely free itself from the material, similar to the ionisation potential.

In the metal energy diagram the difference in energy between the Fermi level (E_F) and the vacuum level is the work function of the metal (Φ_M). The work function is a fundamental property of any material with a conduction band whether it is partially filled (metal) or empty (insulator).

In the semiconductor illustration the energy difference between the vacuum level and the conduction band is the electron affinity (χ). The electron affinity is defined as the energy released for example $E_{initial} - E_{Final}$. In the diagram above this quantity would be $E_{vacuum} - E_F$ as the Fermi level is not constant for semiconductors and changes depending upon the material, the amount of

doping (n-type or p-type) and the quantity of band bending near the surface. The electron affinity is positive for most elements, which have been measured and this would indicate that energy is released. The insulator has been modelled as an intrinsic wide-gap semiconductor where the surface barrier is described by the electron affinity (x_i), the difference in energy between the conduction band and the vacuum level.

The final diagram illustrates the energy levels of a semiconductor with band bending. Band bending is a local change in energy of electrons at the surface of the semiconductor. Band bending occurs when two materials are placed in contact, which have different Fermi levels and will equilibrate to the same level through a local exchange of charge, which leads to curvature of the energy levels in the diagram. Understanding how bands bend is paramount when exploring whether a junction between two materials is rectifying (Schottky) or ohmic. The amount of band bending experienced will depend upon the relative Fermi energies and carrier concentrations of both materials forming the junction.

A typical field effect transistor would have a structure similar to the one illustrated in Figure 4.3 with a p-type bulk silicon substrate. Metallic source (S) and drain (D) contact points are deposited on top of an oxide insulating layer (SiO_2) which has been grown on the surface of the p-type silicon.

An ideal field effect transistor would have a metallic gate which is thick enough to be equipotential under ac and dc conditions and an oxide layer with zero current flowing under all static biasing conditions i.e. a perfect insulator. One other condition for an ideal transistor would be the uniform doping of the semiconductor and that it would be thick enough so that when a large gate voltage is applied, the bulk region is reached before the back contact.
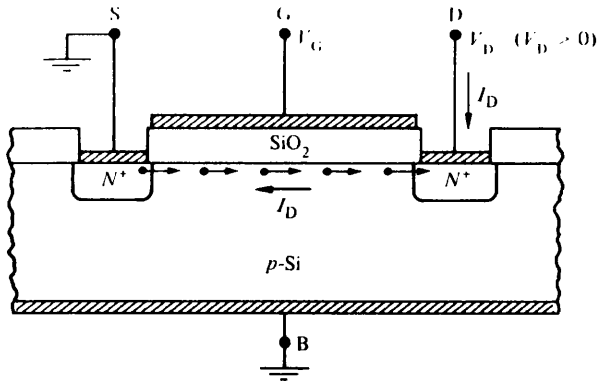
Figure 4.3 A cross-section of basic p-type field effect transistor [8]

The figure illustrates the direction of flow of the drain current (I_D) which flows in response to changes in the applied voltage at the terminals. The set-up shows the current entering the structure through the source (S), subjected to control by the gate (G) and finally leave the device through the drain (D). The voltage applied to both the gate and drain is labelled V_G and V_D, respectively. When the gate voltage (V_G) is accumulation or depletion biased, the region between the source and drain islands contains either an excess or deficit of holes. Under these conditions an open circuit exists between the islands of N+ charge. However when the gate voltage is inversion biased, greater than the depletion-inversion transition point voltage, an inversion layer containing mobile electrons forms parallel to the silicon surface. An inversion layer is now formed between the N+ regions as described in Figure 4.4. The inversion layer (conducting channel) connects the source and drain islands. As the inversion bias increases, the number of electrons situated at the silicon surface increase and this intensifies the conductance of the inversion layer.

(a) $V_D=0$ Inversion layer

S   D

N+   N+

Depletion region

(b) $V_D > 0$

V_{Dsat} V_D

S   D

N+   L   N+

ΔL
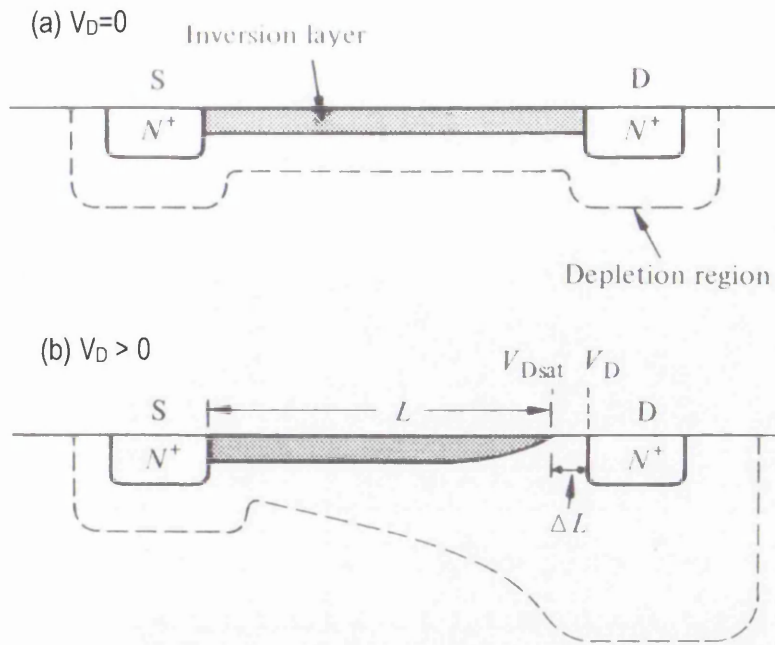
Figure 4.4 Illustration of the inversion layer and depleted region changing under varying circumstances. [8]

Figure 4.4 also illustrates the affect of altering the drain voltage has on the inversion layer. 4(a) is the inversion layer and depletion region at a zero drain voltage. As the drain voltage is increased gradually the depletion region widens and the number of inversion layer carriers decreased. The reduced number of carriers means that the conductance observed has also decreased and is reflected in a decreased slope in the I (V) characteristics.

4.2.1 Nanowire Field effect Transistors

Nanowire field effect transistors have been synthesised from a variety of semiconducting materials. The most promising transistors having been made from tin dioxide (SnO_2) and zinc oxide (ZnO) nanowires as these exhibit the most attractive properties.

SnO_2 nanowires are synthesised by thermal evaporation of tin oxide powders without the presence of a catalyst by Arnold et al [13]. The SnO_2 nanobelts were dispersed in ethanol and deposited on to a p-type silicon substrate with a grown silicon dioxide layer. The sample was treated in an oxygen atmosphere at approximately 800°C for two hours. The sample was then spin coated with PMMA and electron beam technique was used to define an electrode array.

Finally 30nm of Titanium was deposited to make the electrode contacts. It was indicated by the authors that depositing the electrode contacts after the nanobelts was an unusual technique due to the complexity of ensuring the electrodes were in the correct position on top of the nanobelts to make maximum contact. This would also indicate that SnO_2 nanobelts are robust enough to withstand high temperatures and lithography techniques as they remained intact after the experiment and their conductivity was able to be examined.
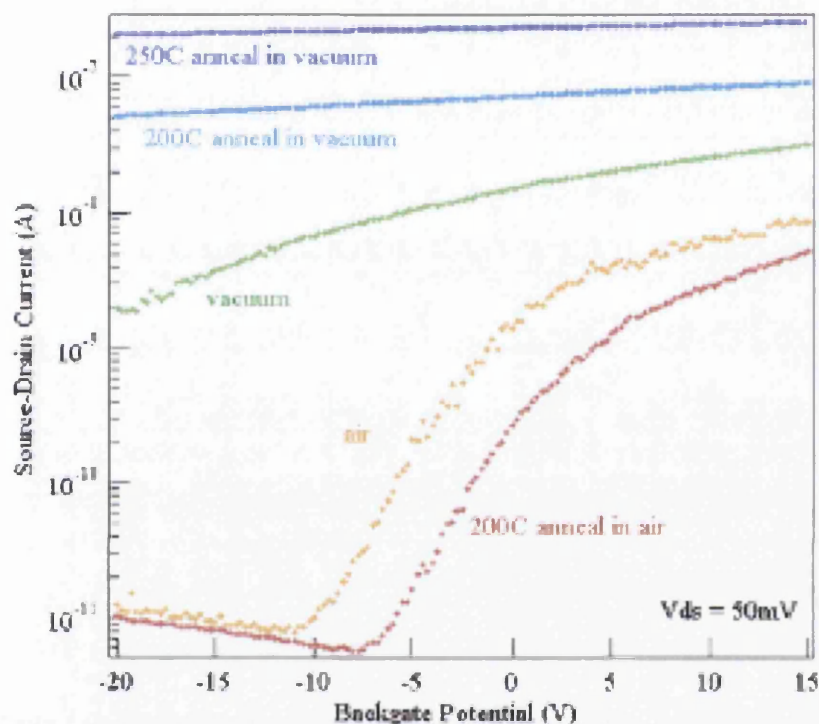
Figure 4.5 Graphical results of SnO2 Nanobelt FET oxygen sensitivity experiments after various treatments [13].

Conductivity experiments were completed and the results showed that without the annealing step at 800°C the nanobelts showed no measurable conductivity. This result indicated that further annealing at lower temperatures in vacuum, oxygen or air would allow the tuning of the electrical properties of the nanobelts. At 200°C in a vacuum environment the conductivity of the nanobelts increased and a negative shift was observed in the threshold voltage (Figure 4.5). Conversely at 200°C in ambient conditions the conductivity decreased and a positive shift in the threshold voltage was seen. These results could be attributed to the variations in the number of oxygen species adsorbed on to the SnO_2 surface. Due to the small dimensions of the nanobelt it has been approximated that 10^{20} surface oxygen sites per cm^3 exist which would indicate that any

small changes in the concentration of adsorbed oxygen species would lead to large changes in nanobelt conductivity. Therefore the increase in conductivity in a vacuum is due to an increase in the number of bulk oxygen vacancies in the nanobelts as bulk and surface oxygen vacancies act as electron donors, contributing to the number of electrons hence increasing conductivity. It is also worth noting that the presence of water on the surface of the transistor could also act as a mask thus decreasing the sensitivity to environmental oxygen until it is removed though annealing.
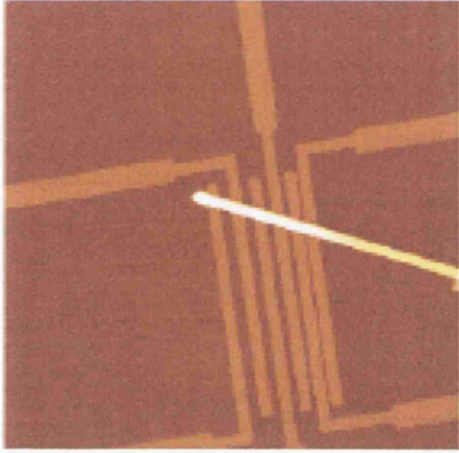
Figure 4.6 10µm non-contact AFM image of ZnO FET across gold electrodes [13]

Zinc Oxide nanobelts field effect transistors were produced in a slightly different way. The nanobelts were dispersed in ethanol and deposited directly on to a pre-defined gold electrode array (Figure 4.6). The ZnO nanobelts transistor was exposed to photoconductivity experiments using a shutter and UV radiation. The results showed steady current flow when the shutter is open. When the shutter was closed two regimes were observed in the time before the shutter was re-opened. Initially there was a sharp drop in conductivity immediately after the shutter was closed. This regime could be attributed to the recombination of the previously photo-generated electrons; hence the electron looses energy and drops back down into its original lower state. After this initial sharp decline a steadier decline was observed. This steady decay in current would suggest a surface chemical reaction occurs which would lose more current. The process of the shutter opening and closing was consistent when repeated over a period of time. The photoconductivity experiments are intriguing and could lead to potential applications in photo-electronics.

ZnO nanowires can also be grown in the presence of a catalyst for example gold film [14]. The nanowires were dispersed in alcohol and deposited on to silicon wafer with oxide layer (Figure 4.7). Prefabricated chromium/ gold pads have previously been patterned on to the silicon wafer by optical lithography. After nanobelt deposition, electron beam lithography was used to define contacts between the nanowires and existing probe pads and finally titanium/gold contacts were deposited. This meant that the nanowires were sandwiched between chromium/gold and titanium/gold pads to encourage a more conductive contact.
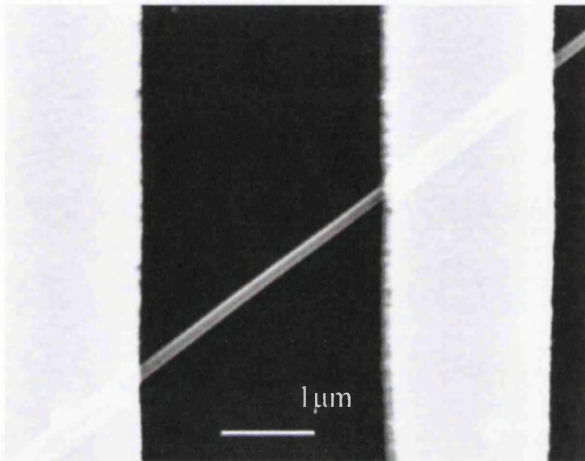
Figure 4.7 SEM image of a ZnO nanowire with a diameter of 101nm [14].

The I (V) characteristics for various gate voltages showed ohmic behaviour up to 2 volts. This would indicate that sandwiching the nanowire between contacts produces an ohmic contact. The dependence of nanowire FET on temperature was also examined. The wire conductivity was found to decrease upon cooling which could be attributed to a lower carrier concentration and an increase in contact resistance.

Chang et al experimented with passivating ZnO FET devices with polyimide (Si_3N_4) in a bid to improve the device performance [15]. The nanowire suspension was deposited on to a P^{++} silicon substrate with a thermally grown 500nm thick silicon dioxide layer. The metal contacts were 10nm of titanium and 100nm of gold. The device was placed in a vacuum chamber and evacuated down to 10^{-6} Torr to remove and surface adsorbents such as oxygen and water. 100nm of silicon dioxide was deposited on to the surface device to prevent subsequent chemical re-adsorption and 50nm of Si_3N_4 was grown on top using the plasma enhance chemical vapour

deposition technique at a temperature of 250°C. A schematic is shown in Figure 4.8. The silicon nitride layer is also an insulating later and is thought of as superior to silicon dioxide in its insulating ability.
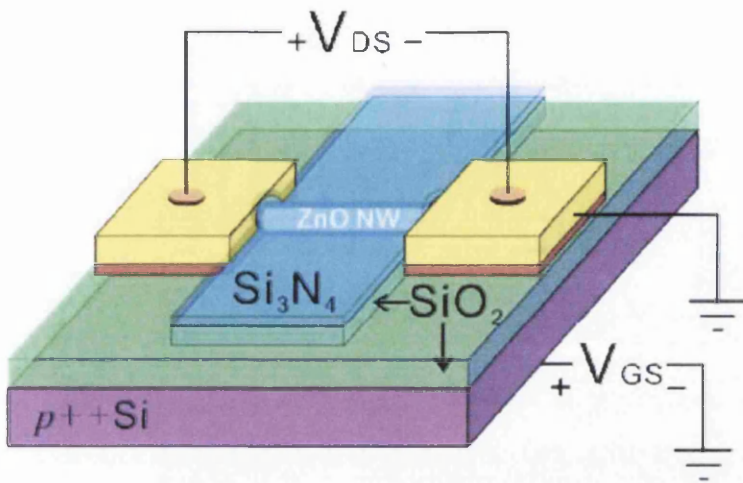
Figure 4.8 Schematic of surface passivated nanowire FET [15].

The increased temperature produces an additional annealing effect and improved the contact between the nanowire and the Ti/Au electrodes producing a low resistive ohmic contact. The electrical results illustrated an obvious saturation region, enhanced I_{ON}/I_{OFF} ratio, and increased field effect mobility to a maximum of 4000cm^2/Vs. Increasing the field effect mobility is crucial as it determines both the carrier velocity and the switching speed. The results were due to the passivation of surface defect states, which normally would act as scattering and trapping centres. The reduction of the surface chemisorption processes at oxygen vacancy surface sites also contributed to improving results.

The work illustrated by Chang et al. was built upon in 2008 by Hong et al [16]. However in the later journal the ZnO FET device was passivated using a Poly (methylmethacrylate) (PMMA, $[C_5O_2H_8]_n$). The device was fabricated using Ti/Au electrodes on a p-type silicon wafer with a 100nm silicon dioxide layer. The 200nm thickness of PMMA was spin coated at a speed of 4000rpm on to the device and then soft-baked at 90°C for 10minutes. The unpassivated devices showed results with lower conductivity, lower I_{ON}/I_{OFF} ratio and overall poor electrical performance. Passivated devices also showed a higher mobility and a reduced threshold voltage when compared to unpassivated devices. Hong contributed these effects to the adsorption of oxygen

molecules at the surface creating a new surface path for the drain current. These results are consistence with the results published from the earlier journal.

4.3 Chemical Sensing

Chemical sensing with nanowire devices whether it is FET or MOSFETS is determined by analysing the change in conductance of the nanowires during exposure to target chemicals. These nanobelts undergo chemisorption with the target chemicals that can either increase or decreased the conductance. The chemisorption induced surface states alter the electronic property of the entire system leading to enhanced sensitivity [17]. This enhance sensitivity can be used in applications such as alcohol breathalysers and Carbon monoxide detectors.

Chemical sensing experiments have previously been explored with a variety of chemicals including oxygen [17], nitrous oxide [17], ammonia [17, 18] and ethanol [19]. Fan and Lu performed O_2, NO_2 and NH_3 chemical sensing with ZnO nanowire Field-Effect Transistors. A p-type Si substrate was capped with a 500nm SiO_2 layer and a square array of 100um^2 areas 3-5um spaced was defined using photolithography [18]. The electrodes were formed by a bilayer evaporation of 10nm Ni and 100nm of Au. The ZnO nanowires were dispersed in isopropyl and this suspension was deposited on top of the substrate. A schematic of the FET is shown in Figure 4.9.
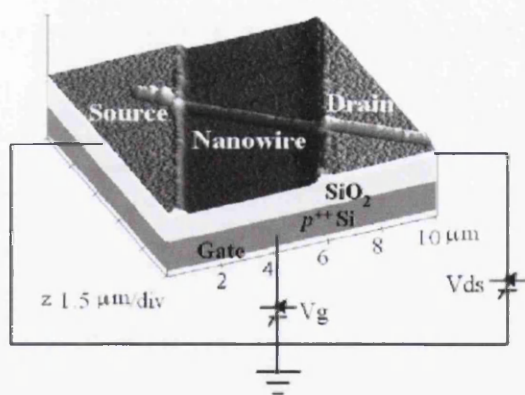
Figure 4.9 AFM image and Schematic of the nanowire field effect transistor [17].

The FET was then placed into a vacuum chamber and under pressure was baked at 200°C in order to remove any surface adsorbents. The chamber was then purged with pure argon. The

concentration of target gas was controlled by adjusting the flow rate of argon gas and the flow rate of target gas to a desired ratio.

On exposure to O_2, NO_2 and NH_3 at room temperature the observed conductance decreases. Due to a higher binding strength between NO_2 and the ZnO nanowire the results showed increased sensitivity to NO_2.

However the sensing experiment with NH_3 as the target gas was repeated at an elevated temperature of 500K. The conductance increased which inferred a temperature dependant Fermi level shift as illustrated in Figure 4.10. As gas molecules adsorb onto the nanowire surface electrons transfer from the material with a higher chemical potential to the lower chemical potential until equilibrium is reached. As shown at room temperature the Fermi level lies above the chemical potential of NH_3. Hence the electrons will move from the nanowire channel to the NH_3 molecules giving a reduction in conductance. At the elevated temperature of 500K the Fermi level has downshifted and now lies below the NH_3 energy level. Electrons now transfer from NH_3 molecules to the nanowire increasing the conductance. This reversal of electron transfer illustrates a switching response from oxidising to reducing behaviour. The increased adsorption/desorption rates of chemical molecules at an elevated temperature could contribute to the conductance.
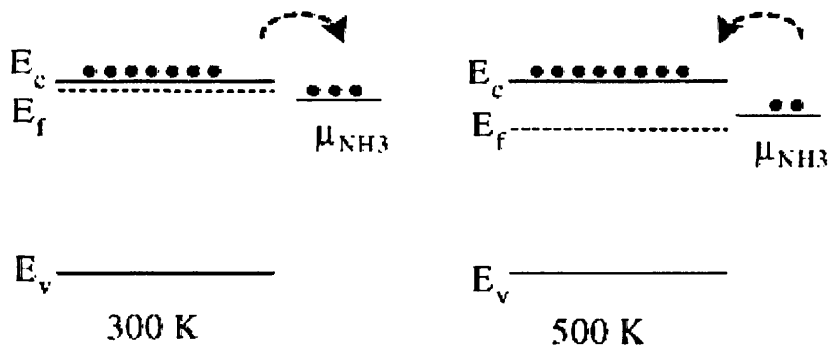
Figure 4.10 Illustration of Fermi Level temperature dependence shift [17].

This report also showed the dependence of nanowire radius on the sensitivity of gas sensing experiments. As the nanowire radius increased, the sensitivity decreased illustrated in Figure

4.11. This behaviour can be explained by the following equation that has been derived from the Drude model.

Equation 4.1

$\Delta G/G_0 = 2/r \ . \ \acute{a} \ Ns/\eta_0$

ΔG: Change in conductance

G_0: Conductance before exposure

R: radius

$\acute{a}$: Charge transfer coefficient

Ns: Surface density of adsorbed molecules

η_0: Electron concentration before exposure
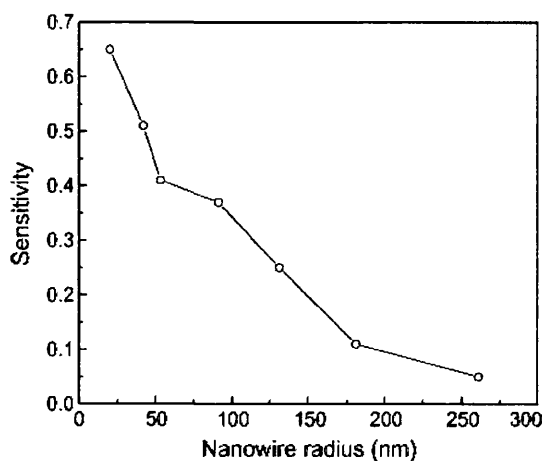
Figure 4.11 Nanowire radius dependence of sensitivity [17]

Equation 4.1 clearly shows that conductance is inversely proportional to the radius of the nanowire. Hence as the radius of the nanowire increases the conductance decreases.

ZnO nanowire gas sensors fabricated on silicon based membrane embedded with platinum electrodes were used to sense ethanol at a range of operating temperatures [19].

As previously discussed when a ZnO nanowire is exposed to air, oxygen molecules adsorb on to the surface forming an oxygen ion through capturing an electron from the conduction band (Figure 4.11). The ZnO nanowire is subsequently in a highly resistive state in ambient air. However when the nanowire is exposed to a reductive gas, the gas reacts with the surface oxygen species decreasing the concentration of oxygen ions. This increases the concentration of electrons and leads to an increase in conductivity. The small diameter of the nanowire (<50nm) indicates that the bulk electronic transport properties are also expected to change. It can be determined that the entire conductivity is determined by the surface.
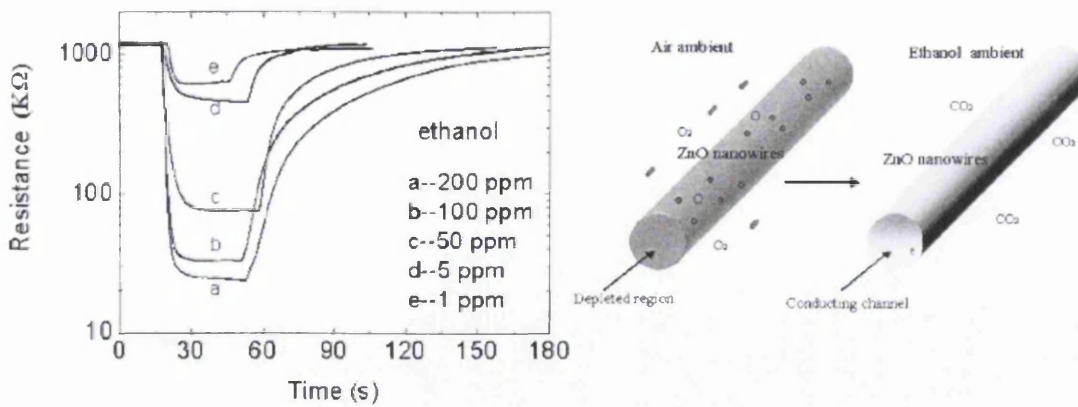
Figure 4.12 Response time of ZnO nanowires to ethanol at 300 ℃ and the sensing mechanism of ZnO nanowires to ethanol [19]

The results for this experiment indicate that the sensitivity is higher than previous experiments, which could be attributed to a larger surface to volume ratio of the nanowire. The sensitivity increased with increasing ethanol concentration. The response time for sensing ethanol was much improved on previous experiments and showed a good recovery (Figure 4.12). The results overall showed an enhanced reaction at elevated temperature between ethanol and oxygen. The best working temperature was to be 300°C as this showed high sensitivity to ethanol presence and a fast response time.

The ability to manufacture a new age of chemical sensors would have potential applications in a range of areas including chemical process controlling, environment monitoring and personal safety. The development of nanowires and nanobelts will move forward the applications into industry and increase scope of devices that will benefit.

4.4 Summary

Much advancement has been made over recent decades in the area of electronics. The ability to manipulate materials at the atomic scale is paramount to the advancement and development in this area. Research must continue in order to manufacture ever-smaller devices. Nanowires are becoming more and more useful in electronics due to their nanoscale size and their robustness, withstanding techniques such as electron beam lithography. Nanowires have shown a wide range of interesting properties including mechanical deformation. Semiconducting nanowires have been synthesised using a variety materials including single elements, compound semiconductors and

metal oxides including zinc oxide and tin dioxide. Recent research in the area of nanowires/ belts has begun to focus on zinc oxide and it is widely being investigated for physical and chemical properties. One of the main attractions of zinc oxide as a semiconducting nanobelt is the wide band gap of 3.37eV due to electronegative atomic bonds. There are advantages for having a wide band gap semiconductor such as increased power capabilities, able to operate at high temperature and at a high frequency. Zinc oxide has also proved to have high biocompatibility, leading to bridging the gap between nanoscience and biotechnology.

One area in which nanobelts have been utilised is in field effect transistors with high conductivity and increasingly good switching ratios. Nanobelt field effect transistor devices have been explored as chemical sensors. Research exposing these devices to a range of chemical stimulus such as ethanol, oxygen and carbon monoxide has shown promising results.

4.5 References

1.   Cobbold R., *Theory and Applications of Field Effect Transistors.* 1970, USA: Wiley-Interscience. 1-26.
2.   Wilson M., et al., *Nanotechnology: Basic science and emerging technology.* 2002: Chapman & Hall/CRC.
3.   [cited; Available from: www.intel.com/technology/mooreslaw/.
4.   Moore G. E., *Cramming more components onto Integrated circuits.* Electronics, 1965. **38**(8).
5.   Lilienfeld J. E., *Method and Apparatus for controlling electric circuits.* 1930: US.
6.   Atalla M. M., *Semiconductor Triode.* 1962: USA.
7.   Pierret R. and Neudeck G., *Field Effect Devices (2nd Ed)* Solid State Devices 1990, USA: Addison-Wesley Publishing Company.
8.   Weimer P.K., *The Thin Film Transistor.* PROC IRE, 1962. **50**: p. 1462-1469.
9.   Kanoh H., et al., *Amorphous-Silicon/Silicon-Nitride Thin Film Transistors Fabricated by Plasma-Free CVD Method* IEEE Electron Device Letters, 1990. **11**(6): p. 258-260.
10.   De Baets J., et al., *High Voltage Polycrystalline CdSe Thin-Film Transistors.* IEEE Electron Device Letters, 1990. **37**(3): p. 636-639.
11.   Weng T., *The Characteristics of CdSxSe1-x Thin Film Transistors.* Proceeding of the IEEE 1974. **1401**.
12.   Garnier F., *Thin Film transistors based on molecular semiconductors.* Pure and Applied Chemistry, 1996. **68**(7): p. 1455-1462.
13.   Arnold M., et al., *Field effect transistors based on single semiconducting oxide nanobelts.* J. Phys. Chem., 2003. **107**: p. 659-663.
14.   Goldberger J., et al., *ZnO Nanowire Transistors* Phys. Chem. B: Letts, 2005. **109**: p. 9-14.
15.   Chang P., et al., *High performance ZnO nanowire field effect transistors.* Appl. Phys. Letts, 2006. **89**(133113): p. 1-3.

16.   Hong W., et al., *Electrical properties of ZnO nanowire field effect transistors by surface passivation.* Colloids and Surfaces A: Physiochem. Eng. Aspects, 2008. **313-314**: p. 378-382.

17.   Fan Z. and Lu J. G., *Chemical sensing with ZnO nanowire field effect transistor.* IEEE transactions on Nanotechnology, 2006. **5**(4): p. 393-396.

18.   Fan Z., et al., *ZnO Nanowire field effect transistor and oxygen sensing property.* Appl. Phys. Letts, 2004. **85**(24): p. 5923-5925.

19.   Wan Q., et al., *Fabrication and ethanol sensing characteristics of ZnO nanowire gas sensors.* Appl. Phys. Letts, 2004. **84**(18): p. 3654-3656.

Chapter 5

Experimental Techniques

5.1 Introduction

Zinc oxide nanowires and nanobelts were synthesised and used for the experiments outlined in chapter 6 and chapter 7. The differences between these nanostructures are illustrated schematically in figure 5.1 which shows their corresponding growth directions. Nanobelts are generally rectangular in shape and are synthesised by a thermal evaporation method. Nanowires are more hexagonal in cross section and have a more cylindrical shape and are grown with gold catalyst particles using a thermal evaporation method.
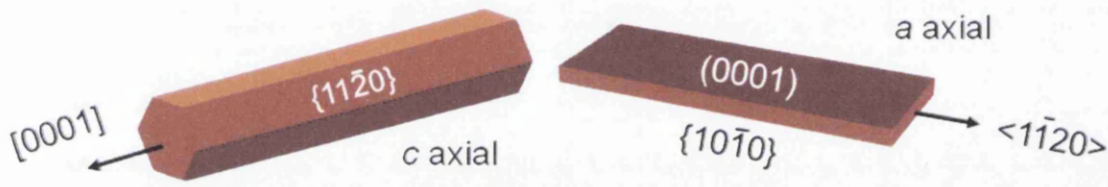
Figure 5.1 Schematic illustrating the difference between nanowires and nanobelts regarding their growth directions.

The nanowires with a moderate growth rate and can be vertically aligned depending upon choice of substrate. Nanobelts have a regular cross section with an aspect ratio of 1:2 or 1:20 with a very high growth rate and can be millimeters in length.

After growth the nanostructures were deposited onto substrates and the photolithography processes, as outlined in section 5.3, were undertaken to make titanium metal contacts on top of the nanostructures.

The nanowires were examined with a Dimension 3100 atomic force microscope and the polarizing experiments shown in chapter 6 were completed. Nanowires prior to wire bonding were also examined in tapping mode AFM to ensure that both ends of the nanobelt were contacting both titanium electrodes.

5.2 Thermal evaporation of Nanostructures
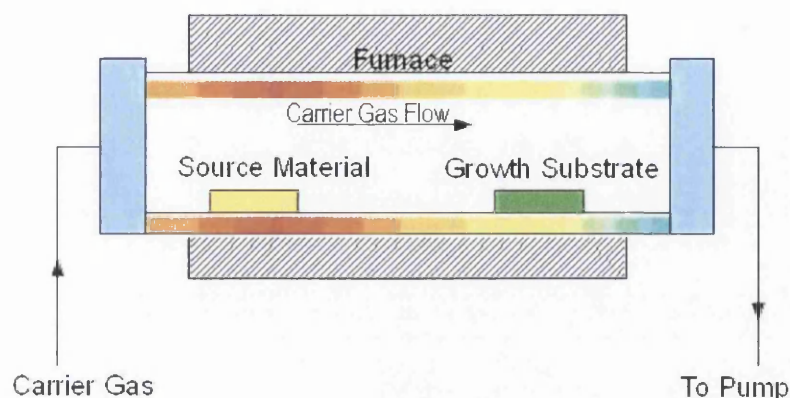
Figure 5.2 Schematic of growth chamber illustrating the change in temperature from left to right inside the horizontal tube furnace.

The furnace used in the synthesis of nanobelts was a Carbolite tube furnace SFT 16/75 which has a maximum operating temperature of 1600°C. The source material is placed in a ceramic boat at the central hot zone of the furnace, which is typically set to 975°C. The source material is a 1:1 mixture (0.6g of each) of zinc oxide power (99.99% purity) mixed with graphite powder, and placed in a ceramic boat of dimensions 9cm x 1cm. The growth substrates are placed, downstream at a specific distance from the source material boat, which is dictated by the temperature profile of the furnace. Argon is used as the carrier gas with 2% oxygen which is controlled by mass flow controllers. An Edwards RV3 rotary pump is placed at the opposite end of the furnace, to evacuate the tube for cleaning procedures and maintain the operating growth pressure of 30mbar. The flow rate of argon gas is an important parameter in the growth mechanism as it is responsible for the transportation of evaporated zinc and oxygen ions to the cooler end of the furnace for deposit onto the growth substrate. If the flow rate of the carrier gas is too low the nanobelts grow on the source material boat and not are carried downstream to the growth substrate. The gas flowing in must be at the same rate as the gas being pumped out in order to maintain a constant pressure within the growth chamber, this is achieved by using a metering valve to restrict the pump. However, at a pressure just below atmospheric pressure, the mobility of zinc and oxygen ions is increased which increases the nucleation probability of the

metal oxide nanobelts. The temperature that was determined to be sufficient is between the minimum evaporation and the melting point of zinc (419.53°C)
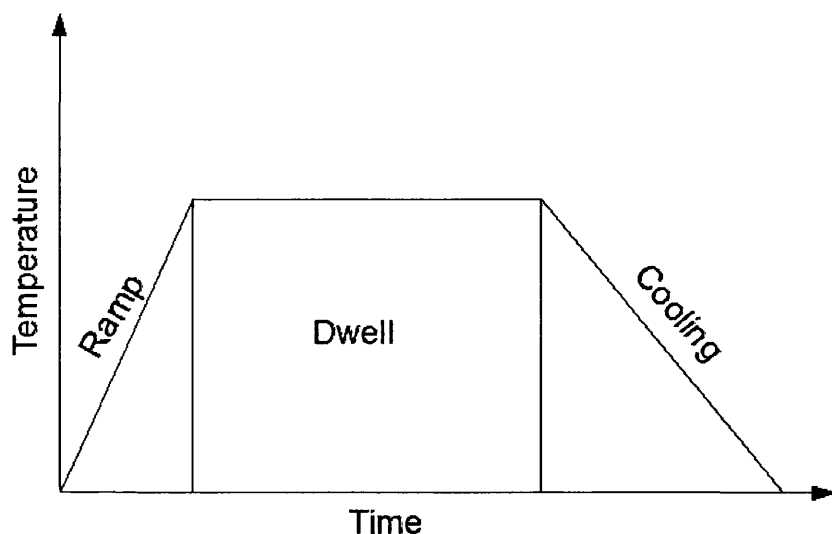
Figure 5.3 Temperature versus time plot of furnace operation.

The operation of the furnace occurs in three stages ramp period, dwell period and cooling period (figure 5.3). During the ramp period the temperature is increased at a rapid rate until a specific temperature is reached. Once this temperature is reached it is maintained for a predetermined time, this is termed the dwell period. Once the evaporated molecules are starting to form nanobelts the length and width of the product is not dependant on the duration of the dwell period, but the concentration of the source material

The presence of oxygen is essential in the production of nanobelts, <2% concentration of O_2 is sufficient during the growth process. The operation efficiency and the temperature distribution along the tube are checked using a thermocouple within a small ceramic tube, which showed a smooth distribution along the tube of the furnace. The curve in figure 5.4 depicts the variance of temperature with distance from the centre of the tube furnace. The graph shows the temperature decreases further away from the centre of the tube. This data can be used to place the growth substrate in a specific temperature range in order to grow the desired nanostructures.
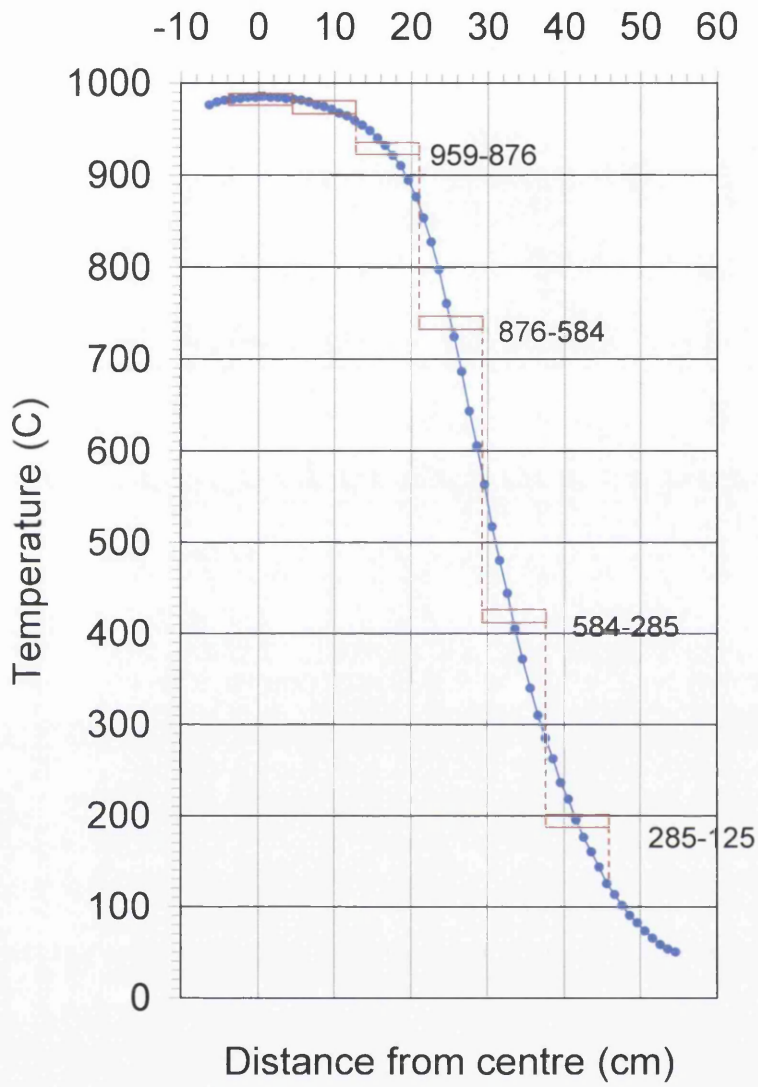
Figure 5.4 Curve illustrating how the temperature inside the Carbolite tube furnace varies with increasing distance from the centre.

5.3 Photolithography

The photoresist used was Shipleys Microposit S1813 acidic resist, chemical name Propylene glycol monomethyl ether acetate (chemical formula $C_6H_{12}O_3$). A few drops of the resist were pipetted on to the silicon wafer and spin coated using a Convac1001s, spun at 4000rpm for 40s. The photoresist layer was measured to be approximately 14000Å (1.4µm) thick. The sample was then soft-baked on a flat hotplate for 3 minutes at 70°C.

The sample was then transferred to a Karl Suss MJB3 mask aligner to expose a pattern on to the photoresist coated sample. Once the desired patterned was chosen (Figure 5.5), the sample was placed in the mask aligner and exposed to UV radiation of 25mW/cm^2 for 9s. The UV irradiates the photoresist which was not covered by the chrome pattern, forming a latent image in the photoresist as shown in step 1 of Figure 5.6.
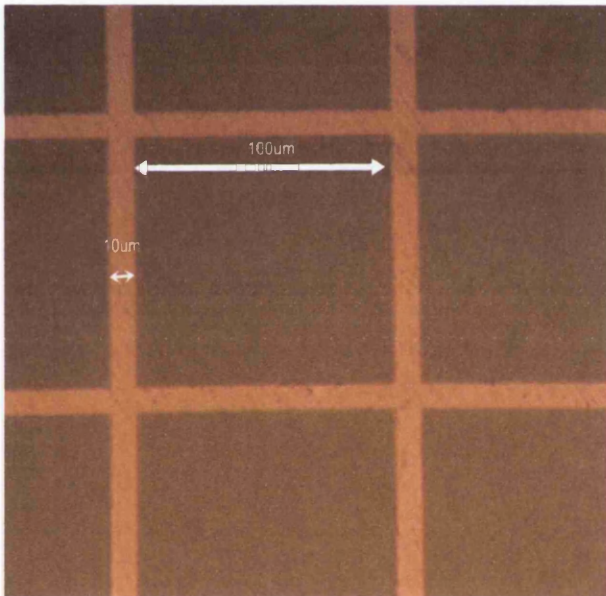
Figure 5.5 Optical microscope image of Mask with width and gap measurements.

The sample is then placed in a beaker of Shipley MF319 basic developer, chemical name Tetramethylammonium hydroxide (chemical formula $(CH_3)_4NOH$). The exposure decomposes a development inhibitor and the developer dissolves any remaining photoresist, leaving only the

pattern determined by the chrome plate. The sample is then washed with deionised water and dried using N_2 gas.
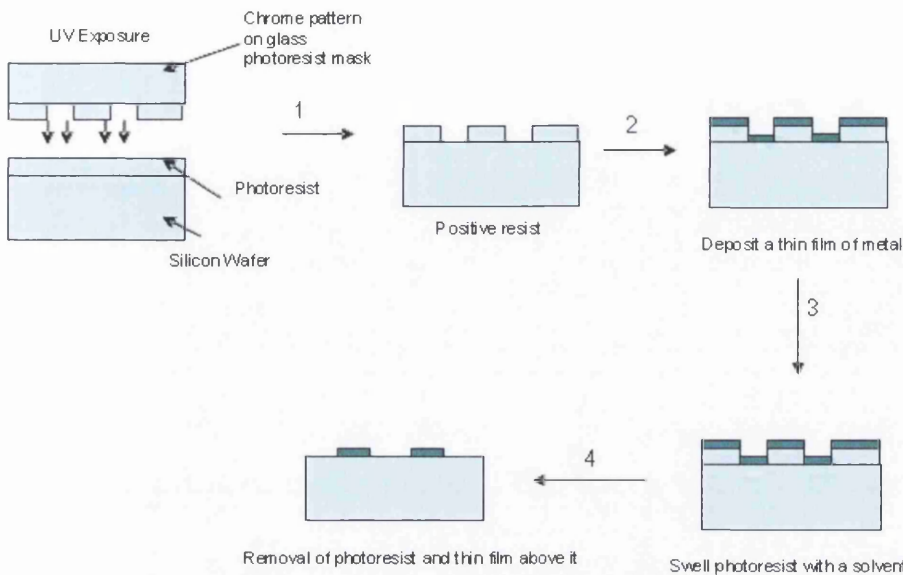
Figure 5.6 Schematic diagram of the photolithography process used to synthesis nanobelt devices.

The sample was then placed in a Kurt J Lesker PVD75 system for the deposition of the thin film of titanium metal by physical vapour deposition (step 2). A variety of recipes were experimented with when depositing the metal and the parameters such as power and flow rate of argon gas were altered to achieve the most productive deposition rate. The most productive deposition rate was defined by incorporating the recorded deposition rate and the required flow rate of gas and temperature. Obviously if the rate of deposition is too fast the pattern will not be covered properly and detail will be missed but if the rate was too slow then not enough metal would be deposited and the time taken for the process to complete would be large. Step 3 in figure 5.6 illustrates the swelling of the resist which has been coated by the deposited metal. The sample was then washed with Acetone and allowed to dry in air (step 4). This step removes the photoresist and the thin film of metal above it leaving a negative resist pattern.

Three different samples were prepared, one with control electrodes (without nanobelts deposited), one with nanobelts on top of electrodes and another one with nanobelts underneath electrodes. For the sample with nanobelts underneath electrodes the silicon wafer was first coated with

nanobelts and then the lift off process was applied. For the other two samples the silicon wafer was bare before the lift off process.

Figure 5.8 An optical microscope image of nanobelts deposited on silicon wafer before photolithography process was started.
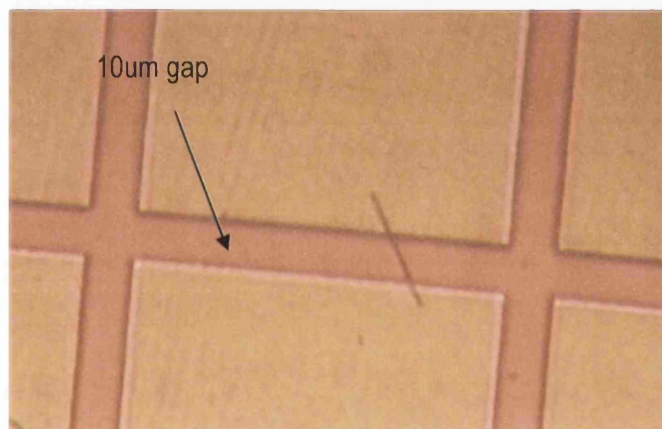
Figure 5.9 Optical microscope image of Nanobelt bridging a gap of 10µm and connecting two 100µm² Titanium contact pads.

The substrate was later changed to glass as during electrical measurements it was discovered that current was tunnelling underneath the titanium pads which led to results showing conduction when no nanobelt was present. Changing the substrate to an insulating material such as glass alleviated this problem.

5.4 Chemical sensing experiments

Wires were manually bonded to the titanium electrode pads using an epoxy alloy as shown in figure 5.10. The wires used were 0.125mm in diameter and composed of Molybdenum metal. They were bonded to the electrode pads using a resin of two parts, one part was epoxy and silver paste and the second part was a hardener and silver paste, and were mixed in a 10:1 ratio respectively.
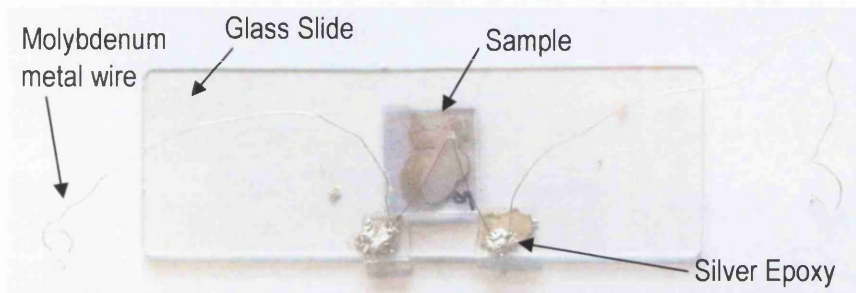
Figure 5.10 A photograph of the sample showing the location of the wires and silver epoxy.

A micromanipulator was used to apply the epoxy to the sample in the desired place and the molybdenum wire was manoeuvred into the correct position using tweezers. The sample was then heated to 100°C for an hour and then allowed to cool naturally until the resin had hardened. The wires coming from the sample where then mounted to a small piece of glass slide and connected to another wire at this point. The idea behind this was that if during the measurement the wires moved or broke then replacing these would be easier in the set up in 5.10 where by the wires connected to the electrode pads would still be in place. The whole sample was mounted on an uncut microscope glass slide to give a sturdy sample.

(b)

Horizontal tube furnace

Sample

Gas feed throughs

Electrical feed throughs
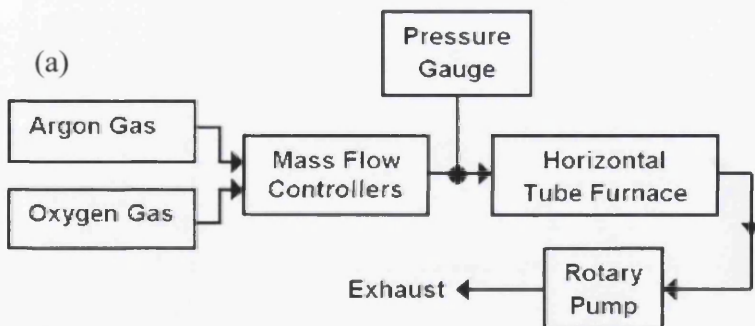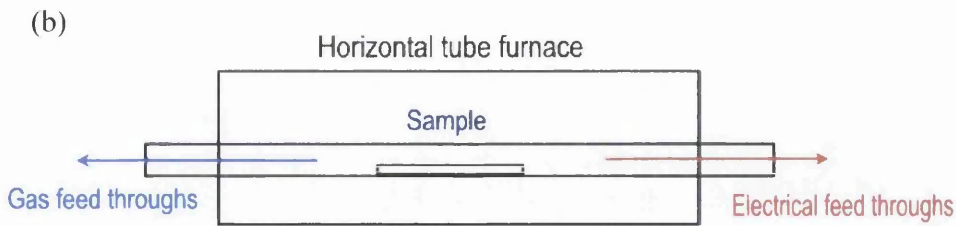
Figure 5.11 (a) schematic of experimental set-up for gas sensing experiment and (b) location of the sample inside the horizontal tube furnace.

The sample was mounted inside a sealed ceramic tube with gas feed through at one end and the electrical feed through at the opposite end. The amount of gas flow into the horizontal tube furnace was controlled by mass flow controllers. The ceramic tube was connected to a rotary pump at the opposite end to the mass flow controllers and placed inside the horizontal tube furnace. The general set up of the experiment is illustrated in figure 5.11 (a) and a schematic representation of the sample inside the horizontal tube furnace in 5.11 (b). The sample was mounted on to a microscope glass slide, placed inside a ceramic boat and pushed inside the ceramic tube inside the horizontal tube furnace.

5.5 Atomic Force Microscope Dimension 3100
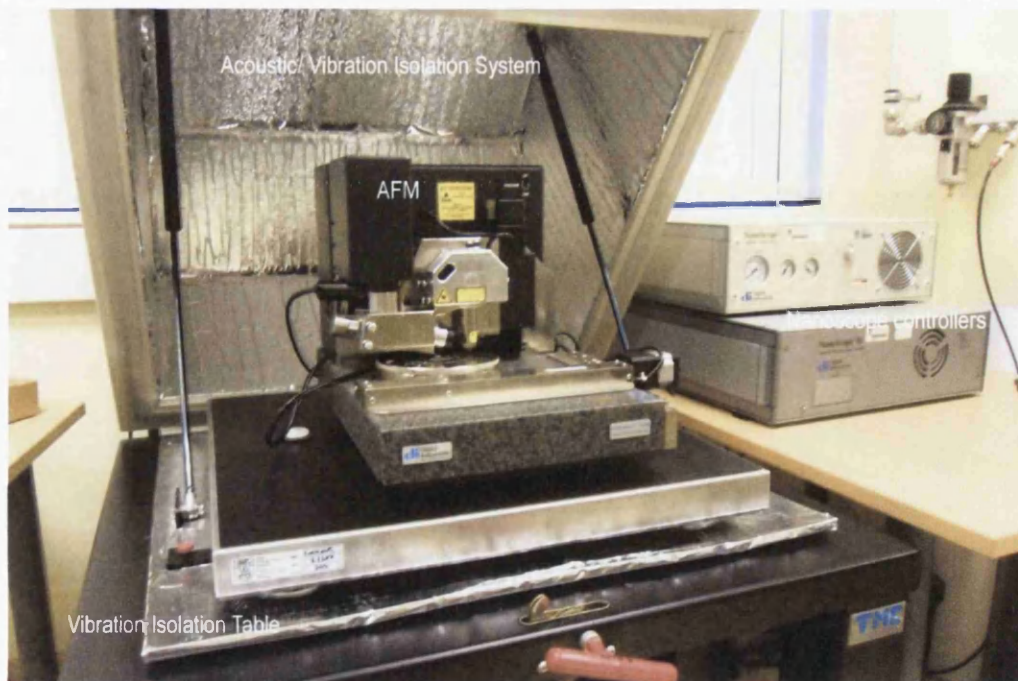
Figure 5.12 Photograph of Dimension 3100 showing the vibration isolation table, the instrument and the nanoscope controllers.

The Dimension 3100 atomic force microscope (AFM) is capable of working in advanced scanning modes such as force modulation, scanning tunneling microscopy, conductance AFM and EFM. A photograph of the dimension is shown in figure 5.12 showing the AFM being housed in an acoustic/ vibration isolation system and situated on a vibration isolation table. These allow the AFM to scan without interference from ground vibration or acoustic noise which can affect the measurements. The nanoscope controller allows multitasking control over the AFM by combining advanced analog and digital circuit designs with real-time software [1]. The AFM consists of a sharp tip mounted at the end of a force-sensing cantilever. The cantilever can be placed at a position of interest on the sample using the light microscope. Once a suitable place of interest is found the cantilever is incrementally lowered towards the surface. As this is brought into close proximity to the sample surface, forces between the atoms of the tip and the atoms of the surface cause the cantilever to deflect. A laser is positioned onto the back of the cantilever, which detects changes in deflection resulting from the tip interacting with the surface. This is achieved by reflecting the laser beam on to a position sensitive photodiode (PSPD), which can measure displacements to an accuracy of less than 1nm. The laser, PSPD and cantilever are all housed in the scanner head as shown in figure 5.13. The signal is then sent to the feedback electronics and any necessary adjustments to the scanner can be made through the electronics.

The piezoelectric scanner expands and contracts proportionally to an applied voltage. It will elongate or contract depending upon the polarity of the AC voltage applied in the range of +220V to −220V. The piezoelectric scanner is made by combining independently operated piezoelectrodes for each dimension (x, y, z) in a single tube.
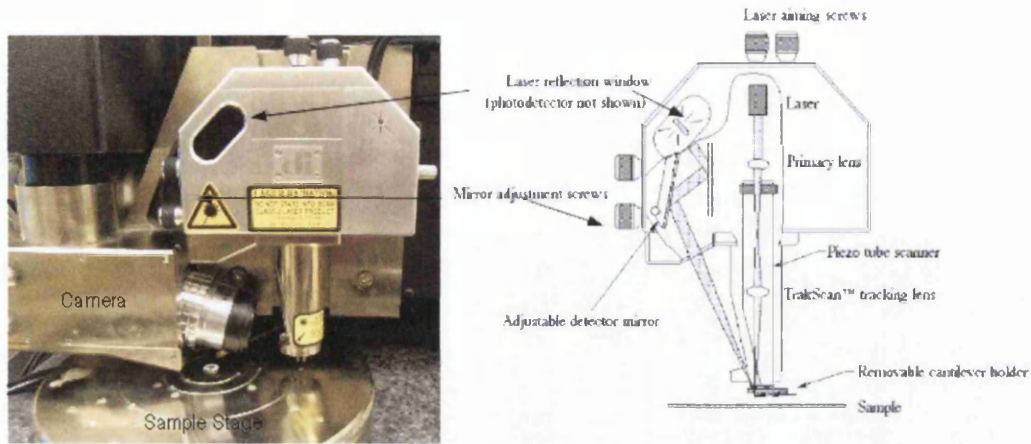
Figure 5.13 Schematic of the scanner head and a photo of the scanner head of the Dimension 3100 [2].

This produces a scanner which can manipulate and explore samples with improved precision. In the case of the Dimension 3100 the sample stage is stationary whilst the scanner moves the tip into the desired location. The scanner is able to raster across the surface by applying the AC voltage to different electrodes of the piezoelectric scanner in x and y. It is also important to note that differences in the material properties and the dimensions of scanners results in each scanner responding differently to an applied voltage (figure 5.14). This sensitivity is described as the distance the piezo extends or contracts per applied volt. The sensitivity described decreases exponentially with operational time and the most variance is observed at the beginning of the scanners life. This means that the scanner will require recalibration during the beginning of operation.
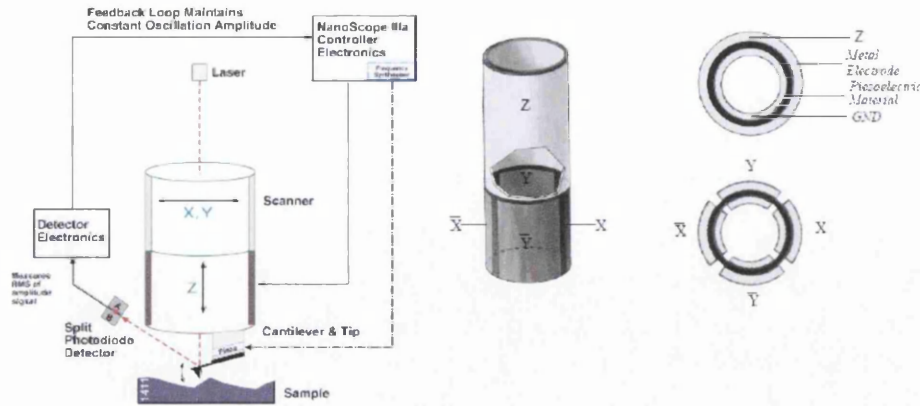
Figure 5.14 Diagram illustrating the piezoelectric element with x, y and z directions[2].

5.5.1 Platinum-Iridium Tips

The tips used for the EFM experiments were sourced from Veeco Probes. The figure 5.15 illustrates the geometries of the cantilever and the tip used. The parameters illustrated in the diagrams are measured in table 5.1.
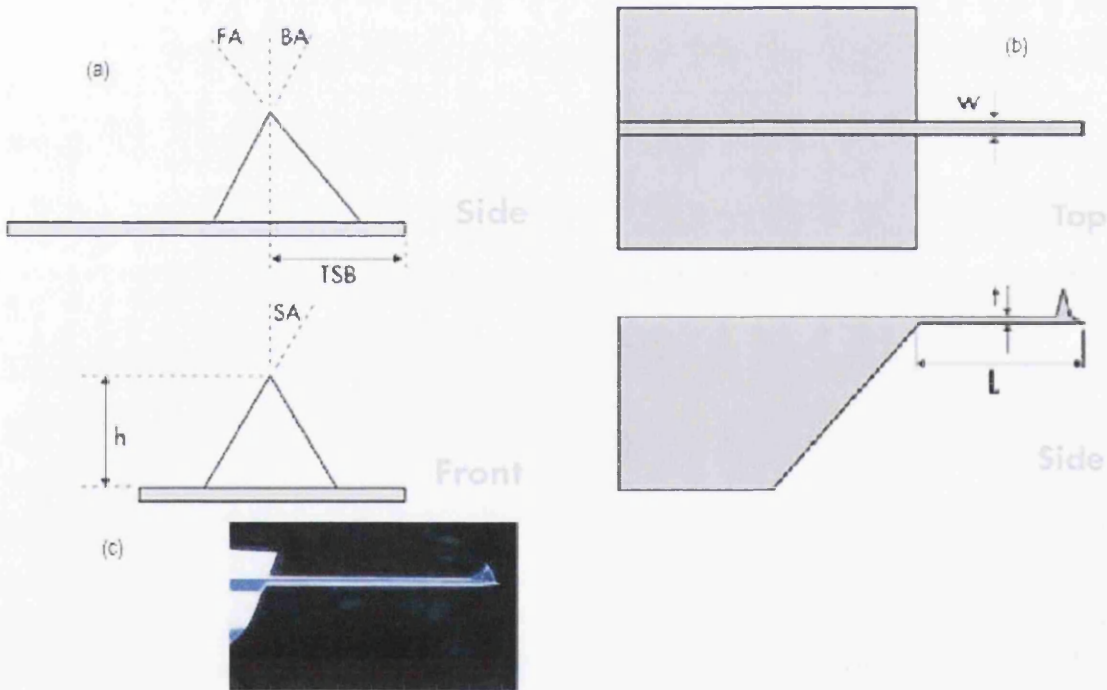
Figure 5.15 (a) Schematic diagram illustrating the front and back profiles of the tip, FA denoting front angle, BA denoting back angle, SA denoting side angle, and h denoting the tip height (b) diagram illustrating the measurements of the cantilever w, width, t, thickness and L, length and (c) an image of the Pt-Ir tip [3].

Tip Specification		Cantilever Specification	
Tip Height (h)	10-15μm	Thickness (nominal)	3μm
Front angle (FA)	25 ±2.5°	Bottom Layer Front	3nm of Cr
Back Angle (BA)	15 ±2.5°	Top Layer Front	20nm of PtIr
Side Angle (SA)	22.5 ±2.5°	Top Layer Back	20nm of PtIr
Tip Radius (nominal)	20 ±5nm		

Table 5.1 Tip and Cantilever numerical specifications for SCM-PIT cantilevers which are used in EFM experiments.

The Pt/Ir coating covers the front side of the cantilever all the way to the apex of the tip. This coating improves the conductivity and allows an electrical path. The backside coating of Pt/Ir is a reflective coating and helps to improve the reflectivity of the laser and hence improve sensitivity of the measurements. The inclusion of Iridium with platinum as the coating increases the durability of the film and allows repeat measurements using the same tip.

The shape of the tip affects the image obtained in two ways. The radius of curvature of the tip affects the feature size which can be resolved hence the smaller the radius the smaller feature size. Secondly the angle of the tips sidewalls affects the ability of the tip to accurately image undulating surfaces, which can result in details of the surface being missed.

5.6 Summary

The nanobelt samples underwent a long process in order to make electrode contacts and conduct gas sensing experiments. This process begins with the thermal evaporation of the zinc oxide nanobelts using a horizontal tube furnace. This technique synthesised zinc oxide nanobelts of varying dimensions as white fluffy powder. These were then deposited on to glass slides and the photolithography process was undertaken where 150nm of titanium metal was deposited in a specific pattern. The titanium electrodes were then connected to molybdenum wires using silver epoxy to enable electrical measurements to be conducted. The nanobelt devices were examined for gas sensing capabilities utilising a horizontal tube furnace and ceramic tube with electrical feed through.

5.7 References

1.   Veeco Instruments (2010) www.veeco.com/dimension-3100-scanning-probe-mircoscope.
2.   Group, D.I.V.M., *Scanning Probe Microscopy Training Notebook V3*. 2001, Santa Barbara USA.
3.   Instruments, V. *SCM-PIT*. 2008 [cited; Available from: https://www.veecoprobes.com/p-3392-scm-pit.aspx.

Chapter 6

Electric Force Microscopy Results and Analysis

6.1 Introduction

The samples of zinc oxide nanowires and silicon n and p type nanowires were explored using electric force microscopy (EFM) as outlined in chapter 3. The results were collected in the format of phase data at varying tip biases and detailed in line profiles and phase images. The data was examined and compared to a similar study published in Nanotechnology Letters (2004) [1] and previous work from a PhD thesis [2]. A value for the capacitance of zinc oxide nanobelts and silicon nanowires were derived and from this a value for the dielectric constant was calculated and compared to the available values for the bulk dielectric constants. These results showed a good agreement with the literature and experimental values.

6.2 Zinc Oxide nanowires

The zinc oxide nanowires were grown using gold catalysts particles in a thermal evaporation process (as illustrated in chapter 5). Nanowires were deposited on to silicon squares (1.5 mm^2) which had a 400nm thick native oxide layer. The Veeco Dimension 3100 (section 5.4) was used to examine the deposited nanobelts with Electric Force Microscopy (EFM) (chapter 2 section 3.5). The tip bias was altered in 2V intervals from -10V to +10V, however when a positive bias was applied the resultant scan was unstable and showed no detail of the nanobelt. One possible explanation was that as the tip was positively biased it electrostatically attracted the nanowires and hence the nanowires became attached to the tip. This would consequently affect the scan and make it blurred and unreadable. As a result only negatively biased scans were explored in detail. The scans are shown below in figures 6.1 and selected tip bias scans are explored in more detail in 6.2-6.4 with the corresponding phase line profiles showing an interesting structure.

Figure 6.1 3μmx3μm size EFM scans of zinc oxide nanowire and gold catalyst particle taken at a tip height of 50nm with (a) tip bias of -2V, (b)tip bias of -4V, (c) tip bias of -6V, (d) tip bias of -8V and (e) tip bias of -10V.

Figure 6.2 shows the EFM image obtained from a tip bias of -2V with the nanobelt having a dark outline and the catalyst particle being a slightly lighter colour. The change in colour reflects the difference in phase as shown by the scale along the side of the image with the lighter colours corresponding to a larger phase and the darker colours being a smaller phase. The image itself is noisy before and after the nanowire with interference lines showing on the scan. This could be due to interference from the substrate sample or an artifact of the tip. On the EFM image a line has been taken across the nanowire and the profile is shown in 6.2 (b). The profile shows an interesting dip-rise-dip profile where the dips correspond to the edges of the nanowire and the rise shows the phase over the nanowire itself. The profile also shows that the width of the nanowire is approximately 320nm. The catalyst particle shows a similar profile in 6.2 (c) however, this time only a small dip is observed either side of the particle. The particle is bigger than the nanowire measuring approximately 400nm wide which is to be expected from the growth mechanism.

Figure 6.2 (a) EFM scan and phase line profiles of the zinc oxide nanowire (b) and (c) gold catalyst particle taken with a tip bias of -2V, scan size 3μmx3μm and lift height of 50nm.

The tip bias was then increased to -8V and the corresponding EFM image is shown in figure 6.3 (a) with the phase line profiles of the zinc oxide nanowire (b) and catalyst particle (c). The EFM image shows the nanowire with much darker characteristics than previous scans with a much more defined outline. The gold particle is also much brighter than previous images indicating an increase in measured phase.
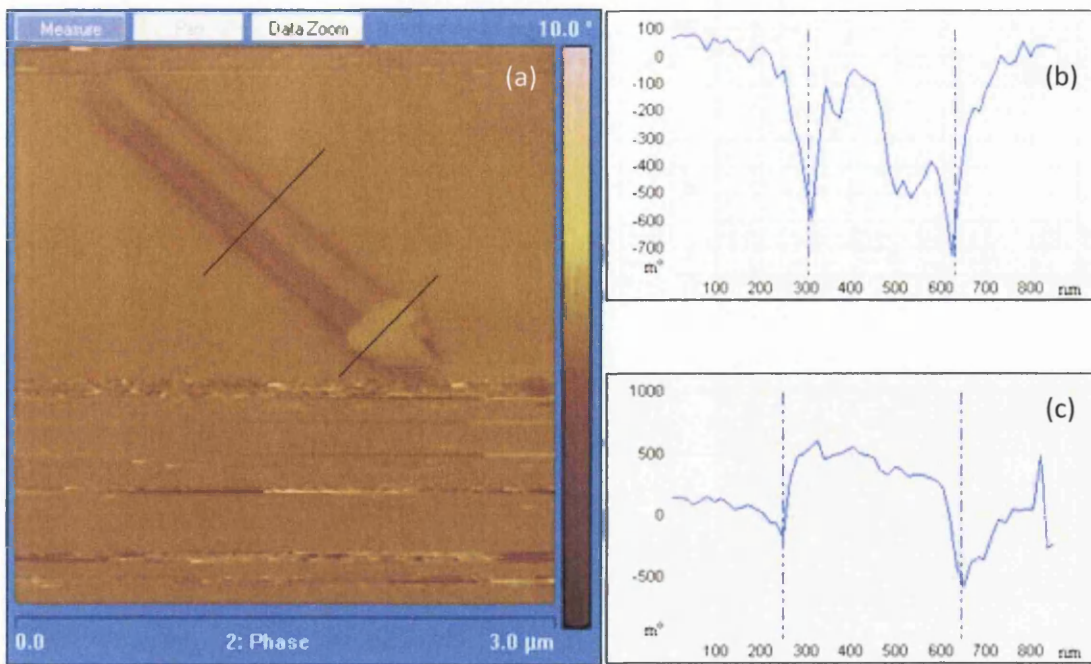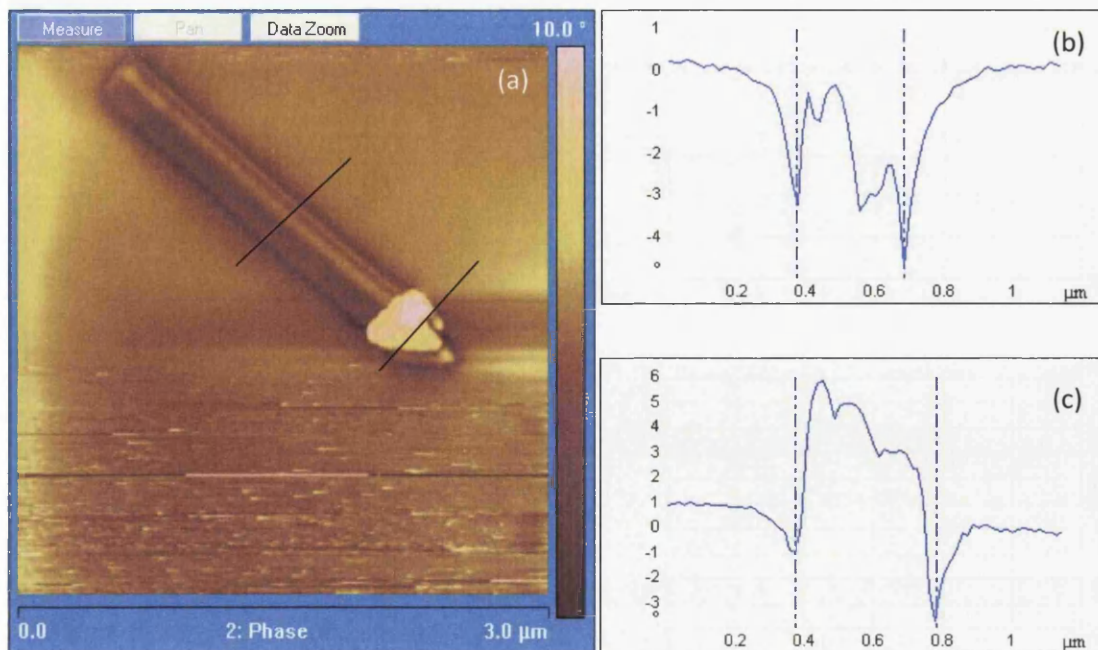

Figure 6.3 (a) EFM scan and phase line profiles of the (b) zinc oxide nanowire and (c) gold catalyst particle taken with a tip bias of -8V, 3μmx3μm scan size and 50nm lift height.

The substrate also appears to be brighter than previously indicating that the substrate has also increased in measured phase. Phase line profiles were taken across the nanowire and the catalyst particle and the corresponding profiles are shown in parts (b) and (c) respectively. The dip-rise-dip characteristic as previously seen is also observed in this profile, however at a tip bias of -8V the dips are more pronounced and the difference between the height of the rise and the trough of the dip is much larger. The profile across the gold catalyst particle still shows a small amount of this characteristic but the rise is much greater than previously seen.

The tip bias was increased by 2V to the maximum voltage of -10. The EFM image of the zinc oxide nanowire is shown in figure 6.4 with the corresponding phase line profiles of the nanowire (b) and gold catalyst particle (c). The image is much brighter than the previous images obtained at a lower tip bias.
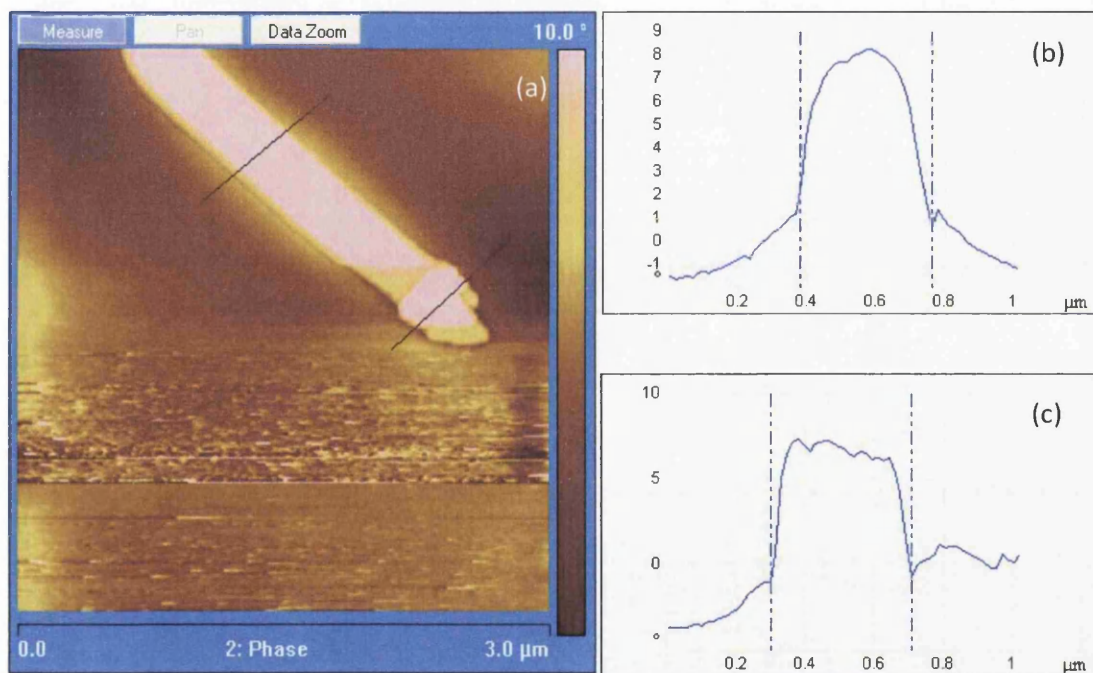
Figure 6.4 (a) EFM image and corresponding phase line profiles of (b) zinc oxide nanowire and (c) gold catalyst particle taken at a tip bias of -10V, scan size of 3μmx3μm and a lift height of 50nm.

6.3 Silicon Nanowire

The silicon nanowire samples were provided by the Max Plank Institute, Hale, Germany and were both p and n-type. The samples were deposited on to silicon squares which had a 400nm native oxide layer, and then examined with EFM using a platinum-iridium tip as described in section 5.4.1.

6.3.1 N-type Nanowires

The silicon nanowires were doped with phosphorous so as to make the wires n-type extrinsic semiconductors. The added phosphorous atoms provide extra conduction electrons to the host silicon material and this creates an excess of negative electron charge carriers. The n-type nanowires were examined in the same way as the zinc oxide nanobelts by imaging the nanowires using EFM. The tip bias was varied between -10V and +10V in 2V intervals and any changes in the phase difference was recorded by capturing the image and completing line profile analysis on the phase scan. Nanowires 1, 3 and 4 are all on the same scan as shown in figure 6.5 and nanowire 2 shown in figure 6.6. The line profiles were obtained from the phase images and hence show the change in phase over the nanowire and therefore do not show the topographical characteristics. All the nanowires were measured using the computer software from the AFM data.
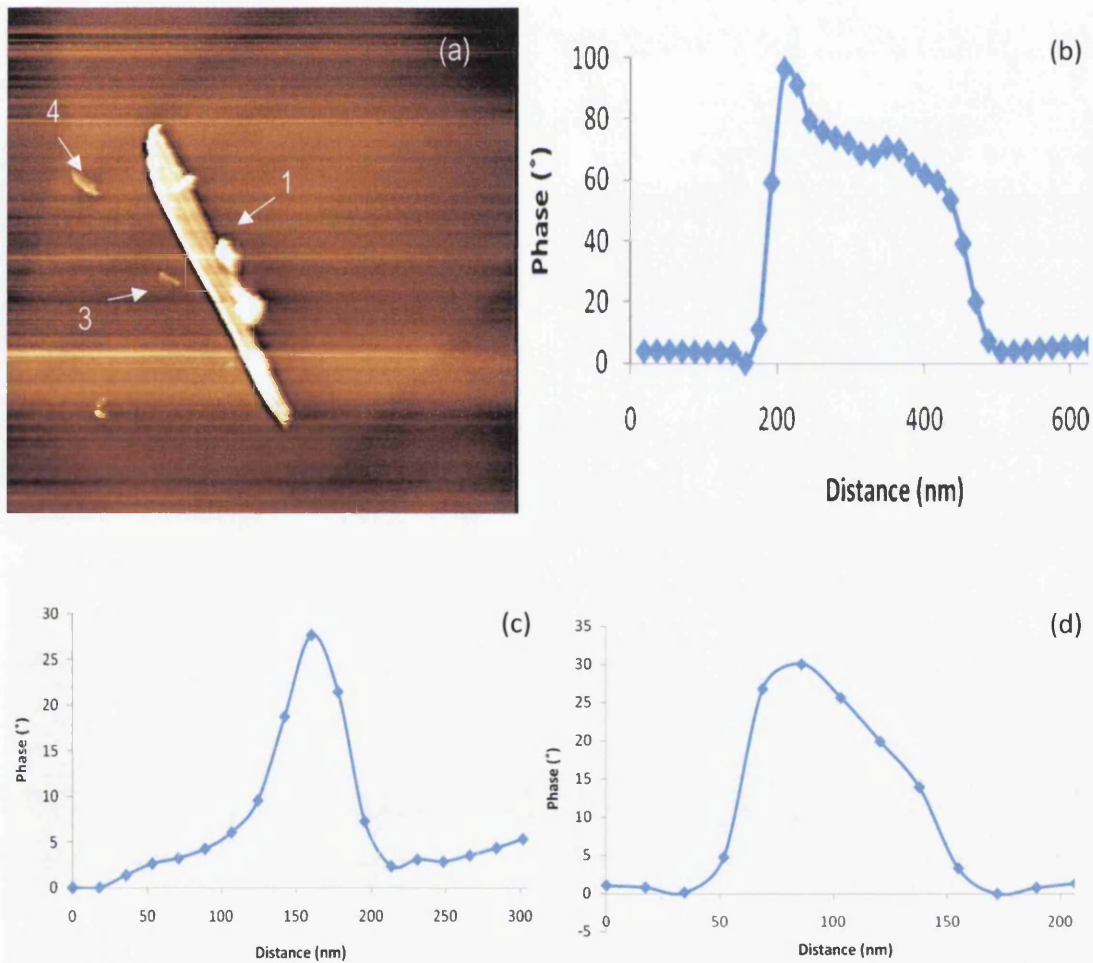
Figure 6.5 (a) EFM image scan size 4.5µmx4.5µm with a lift height of 50nm and tip bias of -6V showing n-type nanowires 1, 3 and 4 as labelled on the scan and (b) phase line profile of nanowire 1, (c) phase line profile of nanowire 3 and (d) phase line profile of nanowire 4.

Nanowire 1 has a almost a rectangular shape with one side being uncharacteristically higher than the other as shown in 6.5 (a). There also appears to be some lumps on the surface of the nanowire and could be a result of the growth process. This could be an imaging artifact and not a true representation of shape. Using the AFM software, nanowire 1 measures 2.8μm in length, 70nm in height and 300nm in width. Nanowire 3 is much smaller than any of the n-type nanowires and a line scan averaged over the nanowire is shown in 6.5 (c). The nanowire does not have the rectangular shape of nanowire 1 and is almost cylindrical and the edges of the nanowire are not clearly defined in the line profile. Nanowire 3 only measures 220nm in length, 25nm in height and 70nm in width. It is almost ten times narrower than nanowire 1. The phase line profile for nanowire 4 is shown in 6.5 (d) and some of the almost rectangular shape has returned and it does not appear to be as narrow as nanowire 3. The edges of the nanowire are almost more clearly defined. Nanowire 4 measures 300nm in length, 30nm in height and 105nm in width which is almost 4 times wider than nanowire 3.
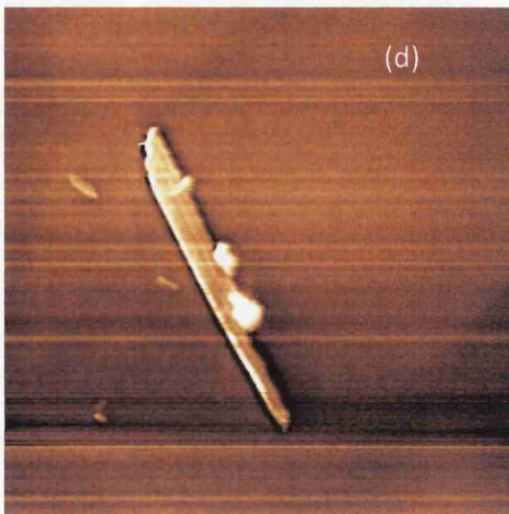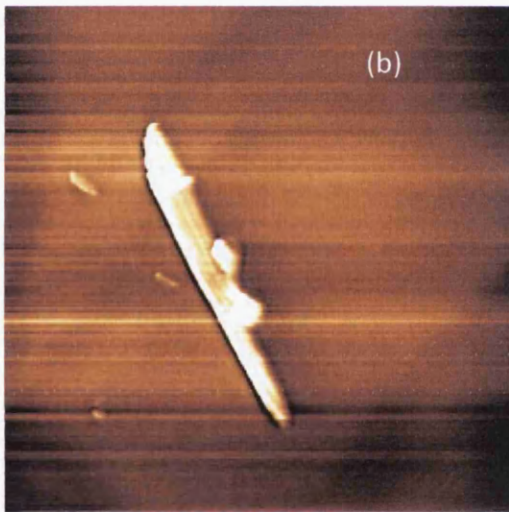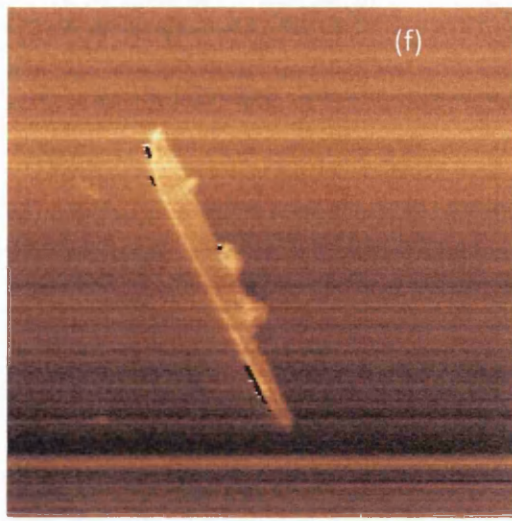
Figure 6.6 EFM images of n-type silicon nanowires 1,3 and 4 taken at a scan size of 4.5µmx4.5µm and a tip height of 50nm with a tip bias of (a) -10V, (b) -8V, (c) -6V, (d) -4V, (e) -2V, (f) 0V, (g) +2V, (h) +4V, (i) +6V, (j) +8V and (k) +10V.

The EFM images shown in figure 6.6 are a complete range of tip bias from -10V to +10V. The most important change observed is that as the tip bias changes the clarity and the features change with the tip bias with the best images being taken with a tip bias of -2V and +2V. The image obtained at 0V appears to be rougher and the features of the nanowires are lost.

Nanowire 2 is shown on a separate EFM scan in figure 6.7 (a) with the line profile averaged over the nanowire shown in (b). Nanowire 2 does not show the same rectangular shape as seen with nanowire 1 but more cylindrical as observed with nanowire 3 however this time the edges of the nanowire are clearly defined.
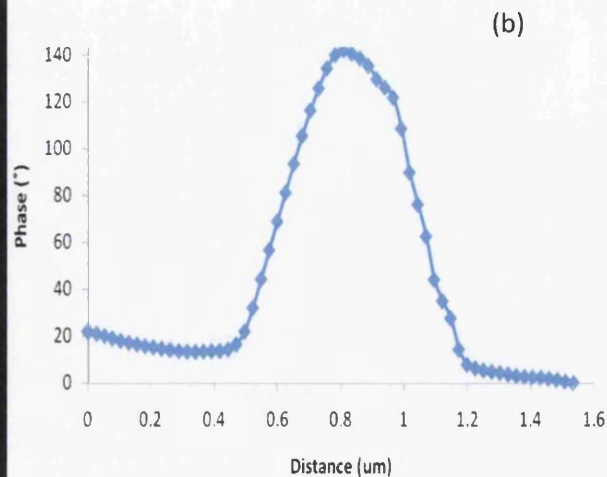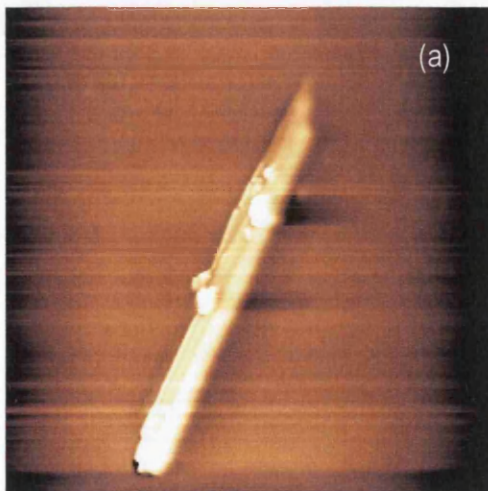
Figure 6.7 (a) EFM image of size 6.5µmx6.5µm with a tip bias of -10V and lift height of 50nm showing n-type nanowire 2 and (b) phase line profile of nanowire 2.

Again as seen with nanowire 1 there appears to be lumps on the surface on the nanowire which could be due to the growth process, such as left over catalyst material. Nanowire 2 is comparable in size to nanowire 1 measuring 5.56µm in length, 660nm in width and only 130nm in height.

Nanowire 2 was examined with a varying tip bias between -10V and +10V and the corresponding EFM images are shown in figure 6.8.
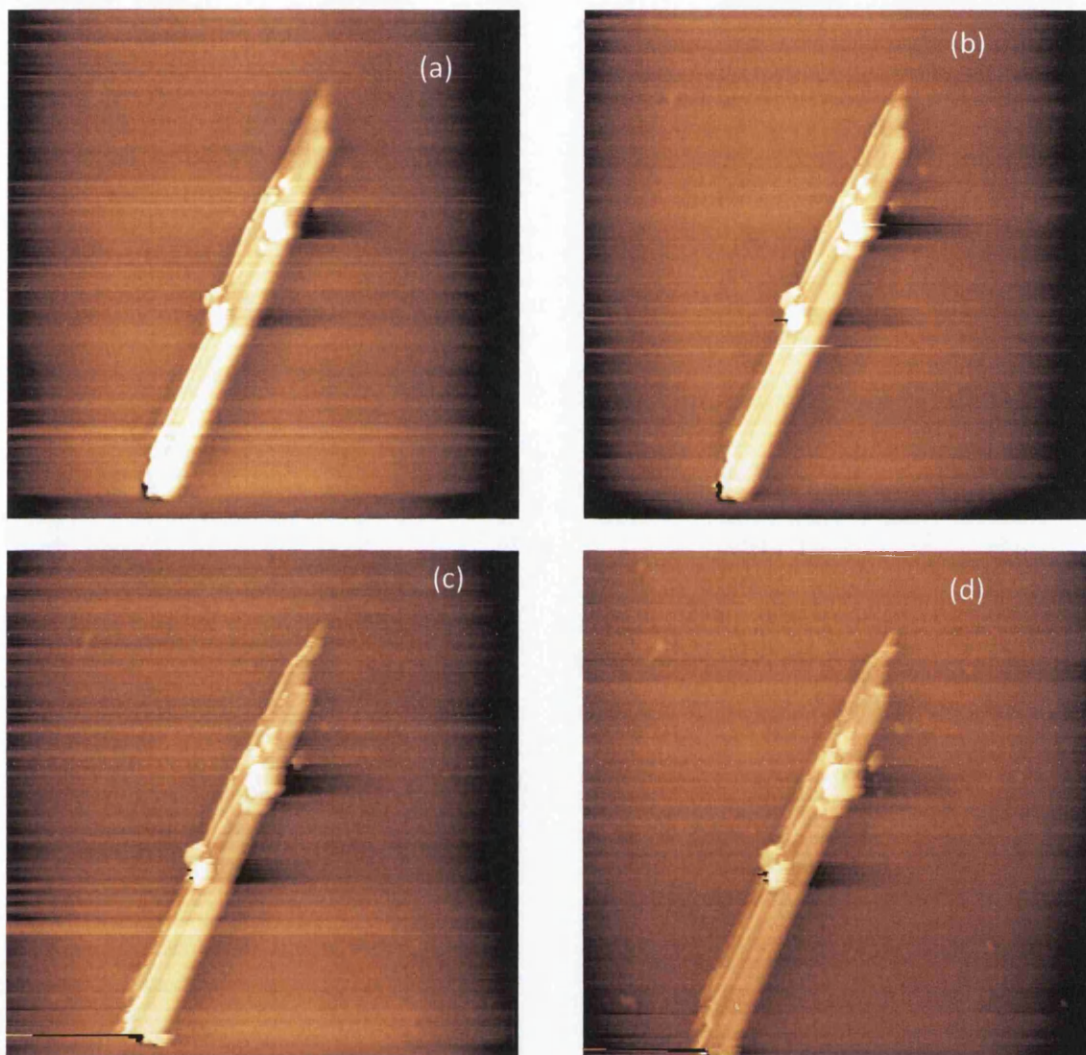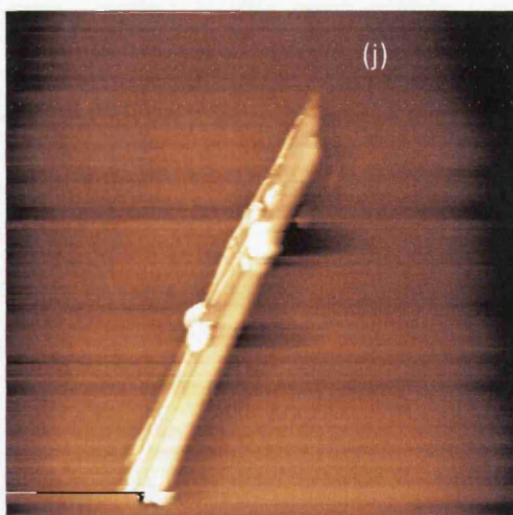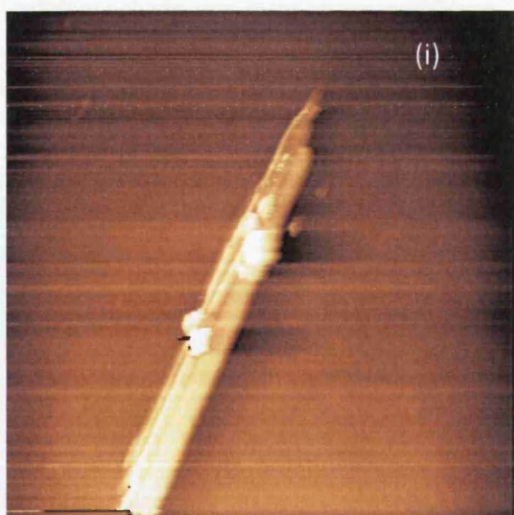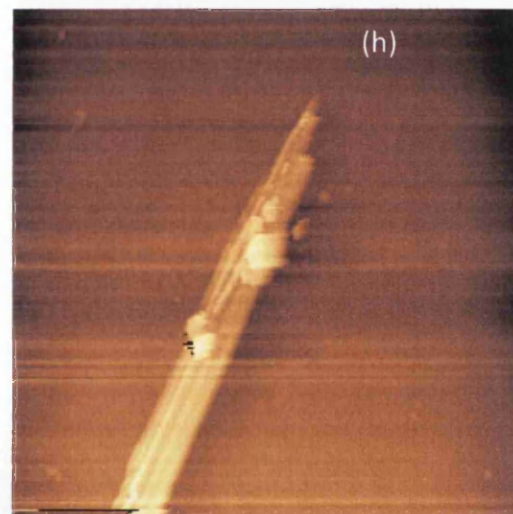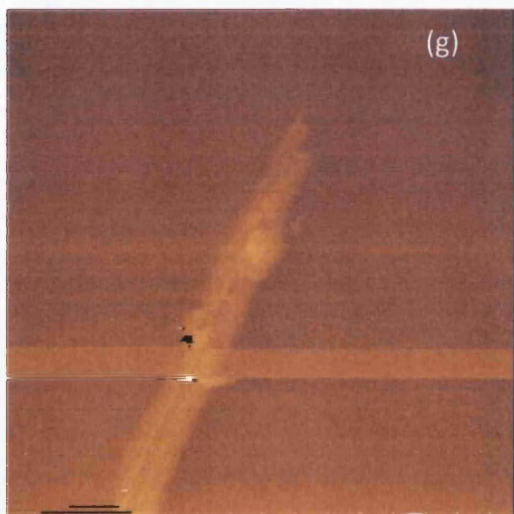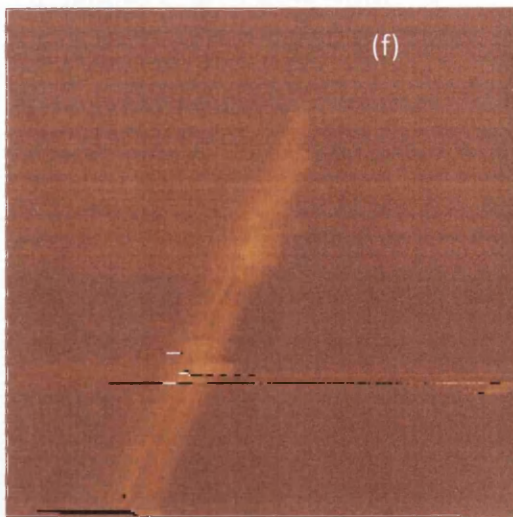
Figure 6.8 EFM images of silicon n-type nanowire 2 taken at a scan size of 6.5μmx6.5μm and a tip height of 50nm with a tip bias of (a) -10V, (b) -8V, (c) -6V, (d) -4V, (e) -2V, (f) 0V, (g) +2V, (h) +4V, (i) +6V, (j) +8V and (k) +10V.

The series of images shown in figure 6.8 show drastic changes in clarity and identifiable features. Some of the images especially with a tip bias of 0V are very rough and show a lot of artifacts which can affect the phase data obtained from the images.

6.3.2 P-type silicon nanowire

The silicon nanowires were doped with boron so as to make the wires p-type extrinsic semiconductors. The added boron creates an abundance of holes which increases the number of free charge carriers. The p-type nanowires were examined in the same way as the n-type silicon nanowires by imaging the nanowires using EFM and varying the tip bias to see changes in the phase difference. Nanowires 2, 3 and 4 are all on the same scan as shown in figure 6.11 and nanowire 1 shown in figure 6.9.
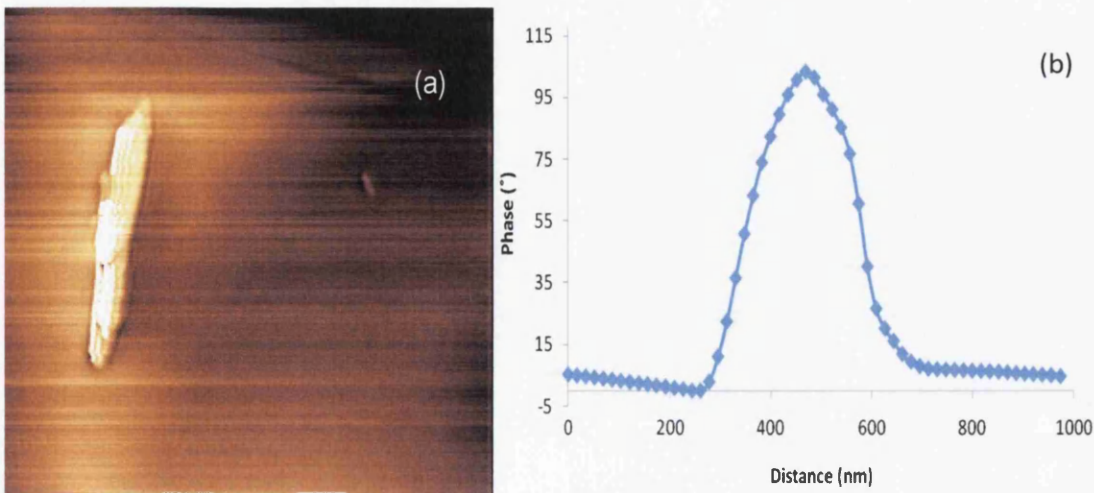
Figure 6.9 (a) EFM image scan size 4.5μmx4.5μm and a tip bias of with a lift height of 50nm of p-type nanowire 1 and (b) corresponding phase line profile for nanowire.

The EFM image of nanowire 1 shows a pattern on the surface of the nanowire which is likely to be a tip artifact rather than real topography. The line profile shows the nanowire having a cylindrical shape with the edges clearly defined. Nanowire 1was measured to be 99nm in height, 320nm in width and 2.5µm in length.

Figure 6.10 shows electric force microscopy phase images of nanowire 1 taken at varying tip bias from +10V to -10V in intervals of 2V.
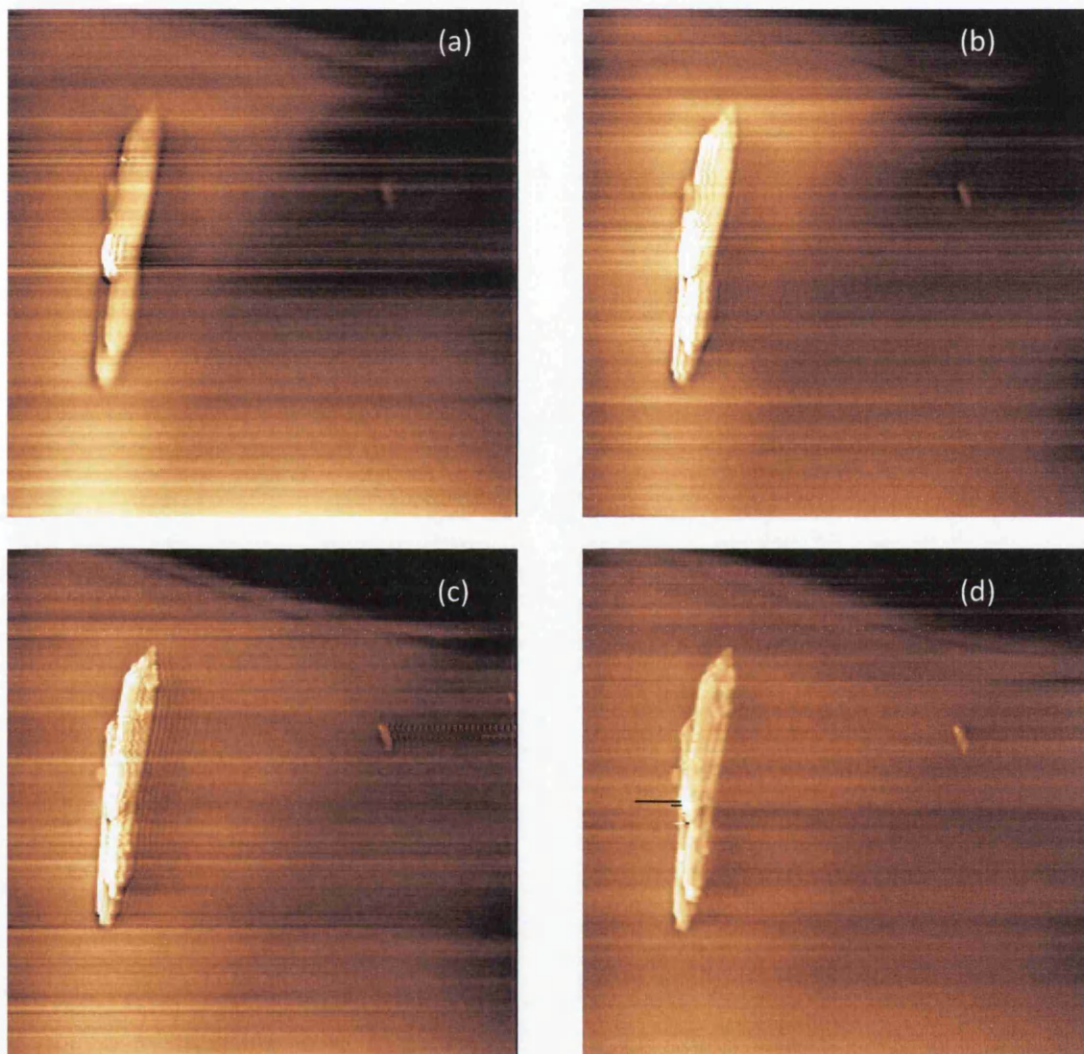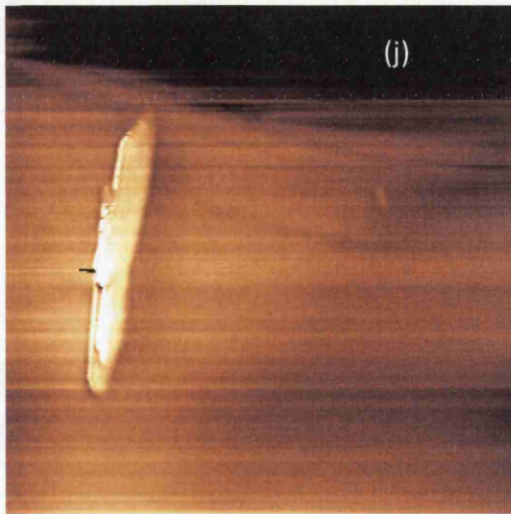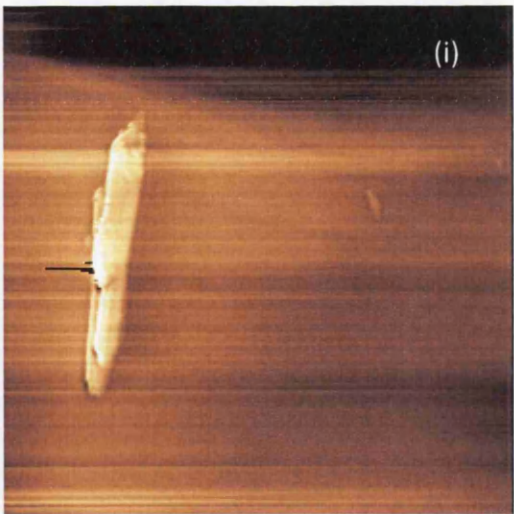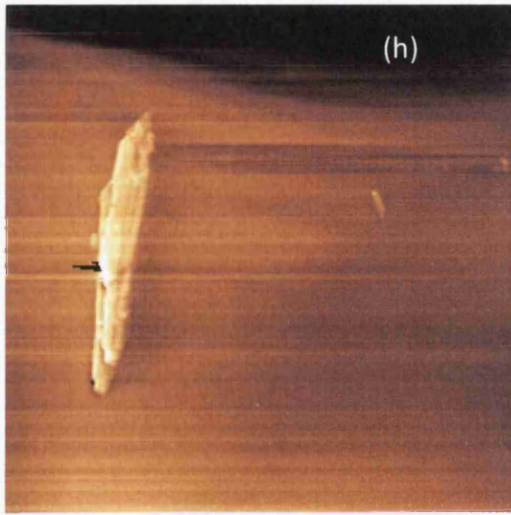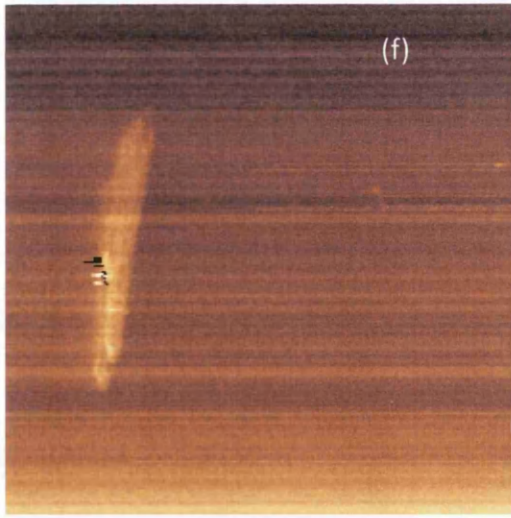
Figure 6.10 EFM images of silicon p-type nanowire 1 taken at a scan size of 4.5µmx4.5µm and a tip height of 50nm with a tip bias of (a) -10V, (b) -8V, (c) -6V, (d) -4V, (e) -2V, (f) 0V, (g) +2V, (h) +4V, (i) +6V, (j) +8V and (k) +10V.

Nanowires 2, 3 and 4 are all shown in figure 6.11 with an EFM image showing all three nanowires and corresponding line scans for each nanowire. Nanowire 2 has a cylindrical shape similar to that shown by nanowire 1 in 6.8. Nanowire 2 was measured to be 214nm in height, 530nm in width and 3.24µm in length which is nearly 1µm longer than nanowire 1. Nanowire 3 appears to be much wider but also much shorter than nanowire 4 from the EFM scan. Nanowire 3 shows an almost triangular shape with a rather pointed top in the line profile in 6.11 (c).
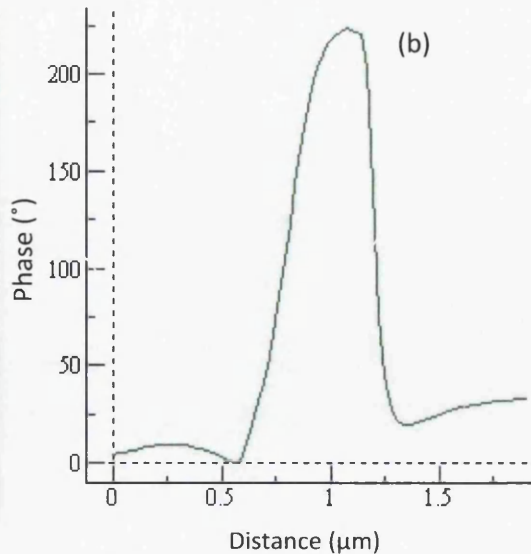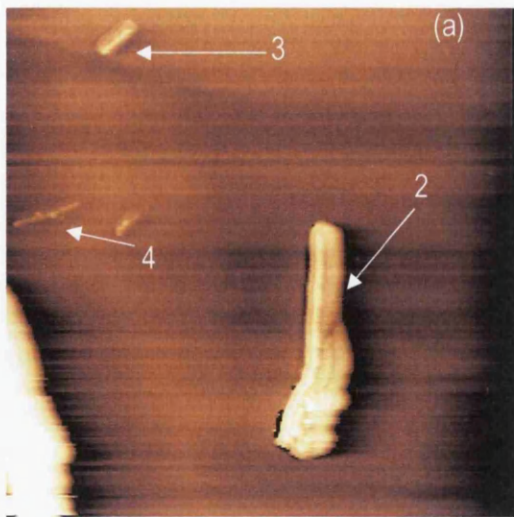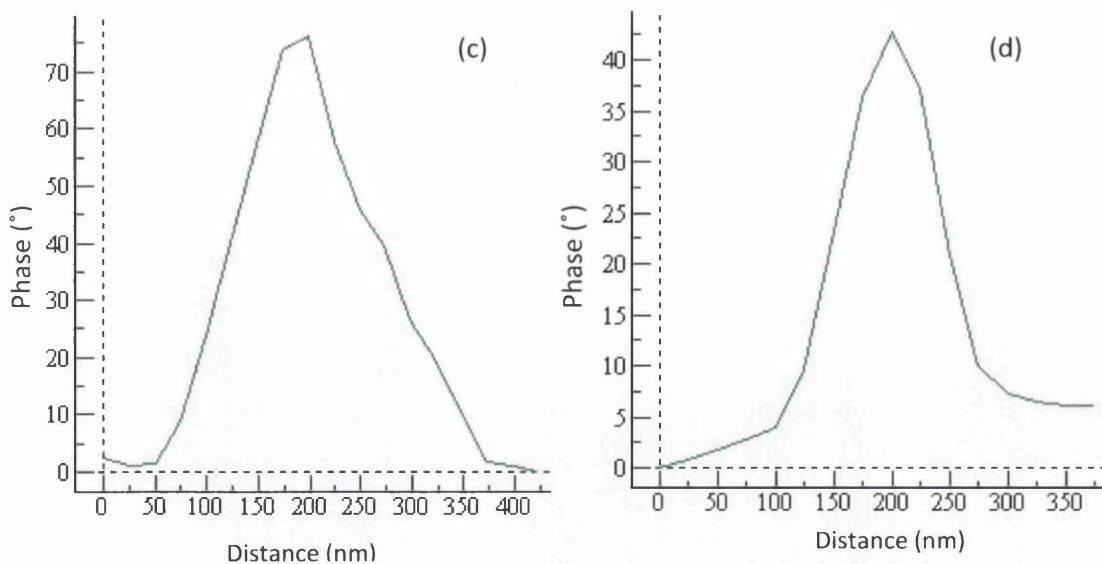
Figure 6.11 (a) EFM image of p-type silicon nanowires 2, 3 and 4, at a scan size of 6.5μmx6.5μm with a tip height of 50nm and a tip bias of -4V (b) line profile of nanowire 2, (c) line profile of nanowire 3 and (d) line profile of nanowire 4.

Nanowire 3 measures 75nm in height, 295nm in width and 611nm in length. Nanowire 4 shows similar shape as nanowire 3 but the edges of the nanowire are not clearly defined which could lead to an error in the measurement of the width of nanowire 4. Nanowire 4 measures 38nm in height, 124nm in width and 890nm in length which is longer and almost 5 times thicker than nanowire 3.

Figure 6.12 shows nanowires 2, 3 and 4 on the same electric force microscopy phase image at varying tip bias from +10V to -10V in intervals of 2V.
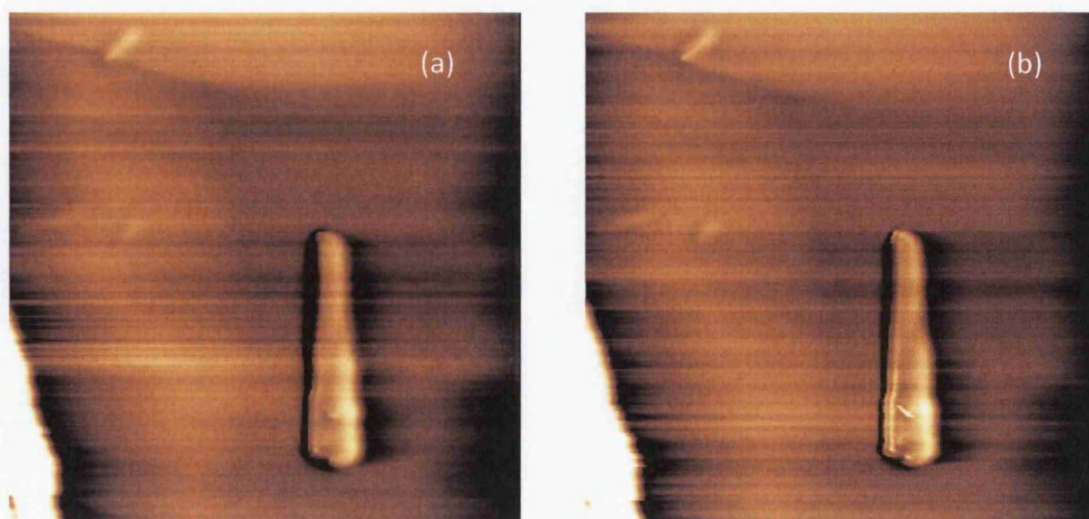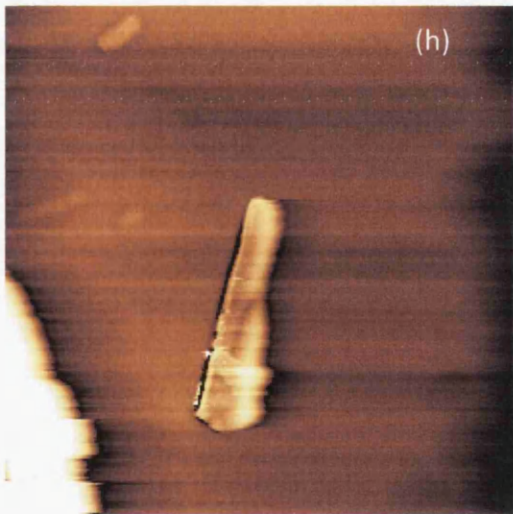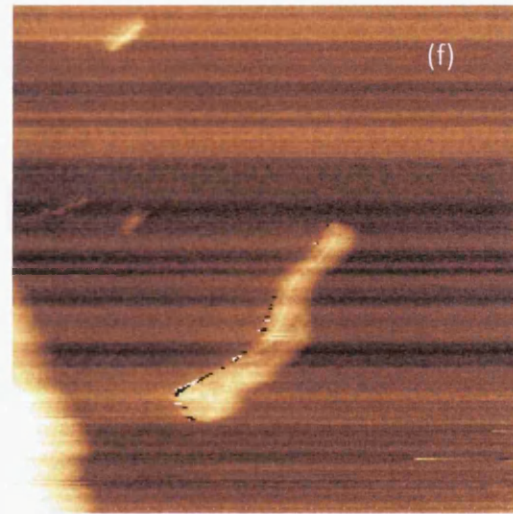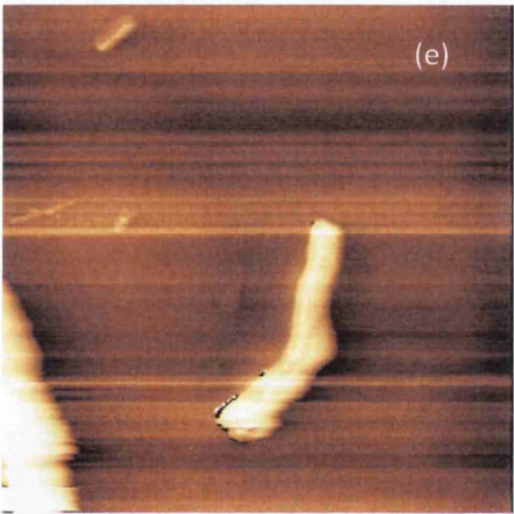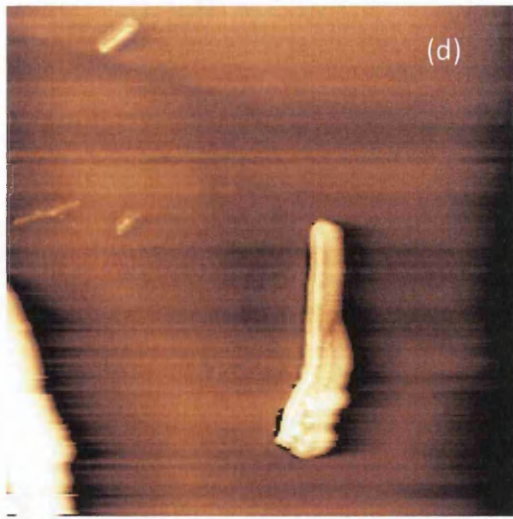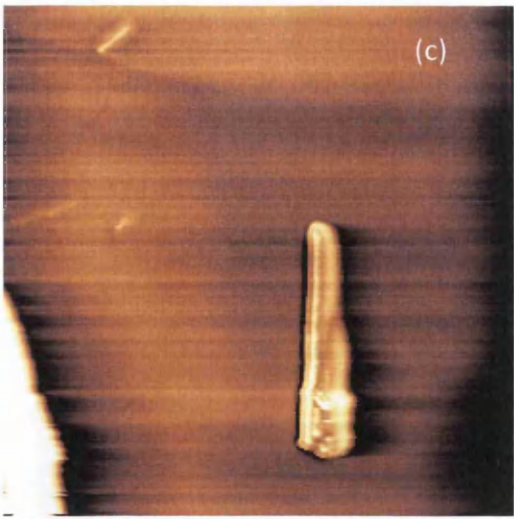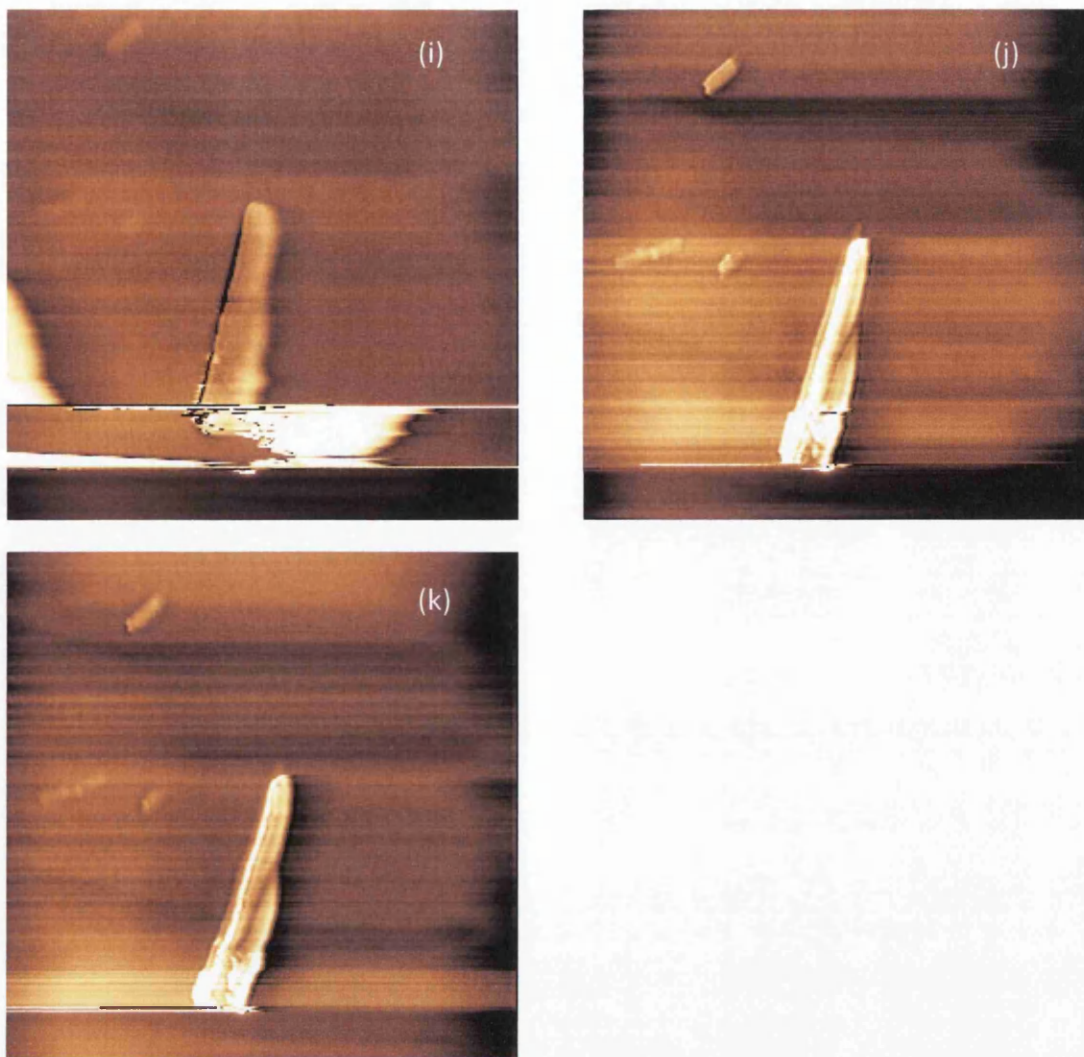
Figure 6.12 EFM images of silicon p-type nanowire 2, 3 and 4 taken at a scan size of 6.5µmx6.5µm and a tip height of 50nm with a tip bias of (a) -10V, (b) -8V, (c) -6V, (d) -4V, (e) -2V, (f) 0V, (g) +2V, (h) +4V, (i) +6V, (j) +8V and (k) +10V.

6.4 Theory

The samples were scanned using EFM as explained and outlined in chapter 3. The images obtained showed both topographic and phase data for zinc oxide nanowire and silicon nanowires on silicon substrates. The phase data collected at various tip biases was compared to and analysed using the method explained by Staii *et al* published in Nano Letters [1] and through previous work from Tan [2]. Riedel et al also used the same idea for their paper published in the Journal of Applied Physics in 2009 where they examined films of silicon dioxide and gold samples using EFM technique to determine the dielectric constant [3].

There are two situations which need to be explored, the first when the tip is over the bare substrate and the second when the tip is over the nanowire. In the first scenario when the tip is over the bare substrate only the contribution from the bare substrate and not including any

from the nanowire. The second scenario is more complex by taking into consideration the contribution from the nanowire, and the substrate.

The background phase measured against different tip biases is shown in figure 6.13. The results give a parabolic shaped graph, where the phase decreases with an increasing tip bias in both the negative and positive applied tip bias. The phase also changes sign at certain points in positive and negative applied tip biases.
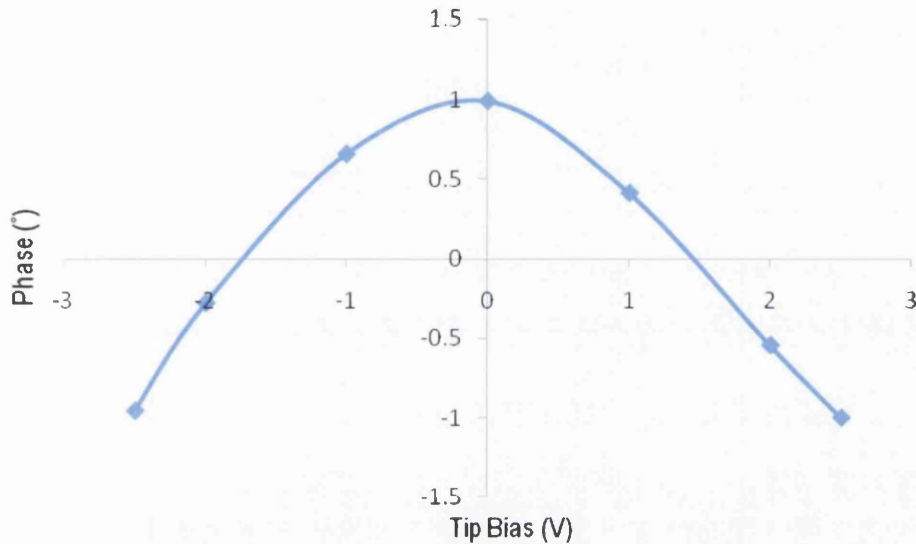
Figure 6.13 The background phase plotted against the applied tip bias showing parabolic behavior.

The cantilever is scanned at a height h above the bare substrate the electrostatic force, $F_1(h)$, between the metallic tip and the surface alters the resonant frequency by $\Delta\omega$. For a small electrostatic force the frequency change is proportional to the force gradient as outlined by equation 6.1.

$$\Delta\omega \approx -\left[\frac{\omega_0}{2k}\right]F_1'(h)$$

Equation 6.1

It is important to note that the electrostatic force $F_1'(h)$ is now the first differential and ω_0 is the resonant frequency. Therefore an expression for the capacitance, C_1' can be derived involving the tangent of the measured phase shift (Φ_0), the quality factor (Q) and the spring constant (k) of the cantilever and the voltage applied to the tip, V_{tip}.

$$Tan(\Phi_0) = -\frac{Q}{2k}C_1''(h)V_{tip}^2$$

Equation 6.2

Plotting Tan (Φ_0) against V_{tip}^2 from data obtained from the phase images yields a straight line as the equation is linear. The gradient of this line is equal to $-\frac{Q}{2k}C_1''(h)$ and as the quality factor (Q) and the spring constant (k) which are both known values the capacitance of the substrate can be calculated.

$$Gradient = -\frac{Q}{2k}C_1''(h)$$
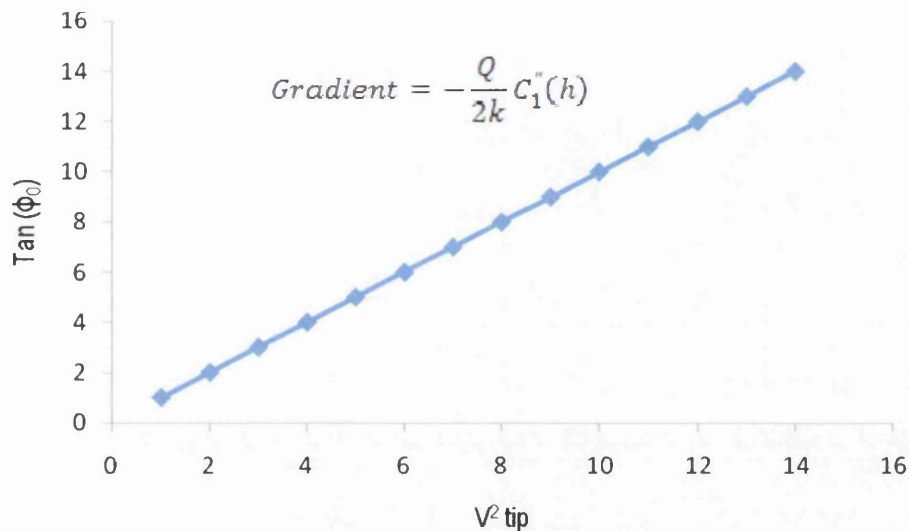
Figure 6.14 Background phase plotted against the square of the tip bias showing the gradient.

When the tip is over the substrate and only recording changes in the phase for the silicon wafer substrate the system can be thought of as two capacitors in series incorporating the dielectric constant of air, ε_0 and the dielectric constant of the silicon dioxide layer ε_r. The dielectric constant for the silicon dioxide layer can be calculated using the value for C_1'' as calculated from graph 6.14 and the equations below.
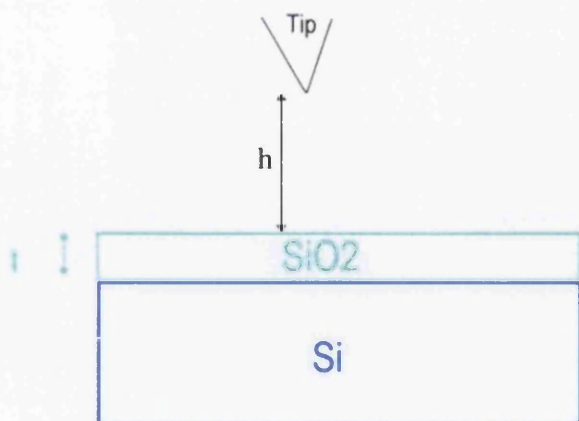
Figure 6.15 Illustration of tip over substrate showing the tip height h, and the depth of native oxide layer t.

From the diagram in 6.15

$$C_h = \frac{\varepsilon_0 \pi R^2}{h}$$

Equation 6.4

$$C_d = \frac{\varepsilon_0 \varepsilon_r \pi R^2}{d}$$

Equation 6.5

Therefore the total capacitance for the system is

$$C_{total} = \frac{\varepsilon_0 \pi R^2}{\left[\frac{d}{\varepsilon_r}+h\right]}$$

Equation 6.6

Taking the second differential

$$C''_{Total} = \frac{2\varepsilon_0 \pi R^2}{\left[\frac{d}{\varepsilon_r}+h\right]^3}$$

Equation 6.7

The equation 6.7 for C''_{Total} actually denotes C''_1 and is similar to the equation for the background capacitance as derived by Staii *et al* [1]. Using the equation 6.7 the dielectric constant for the silicon dioxide layer can be calculated and compared to literature values. The term πR^2 describes the geometry of the tip with R being the radius of curvature and the lift height h being 50nm and the thickness of the silicon dioxide layer d.

The equations above can be used to calculate the capacitance of the substrate and in order to calculate the capacitance of the nanobelt the extra electrostatic contribution due to the interaction between the nanobelt and the tip must be taken into consideration. The capacitance of the nanobelt $C'_2(h)$ can be calculated from equation 6.3.

$$Tan(\Phi - \Phi_0) \approx \frac{Q}{2k}(C''_1(h) - C''_2(h))V_{tip}^2$$

Equation 6.3

Therefore this time if $Tan(\Phi-\Phi_0)$ is plotted against V_{tip}^2 then the gradient is $\frac{Q}{2k}(C''_1(h) - C''_2(h))$ and as the previous calculation using equation 6.2 has determined a numerical value for C''_1 the capacitance for the nanobelt C''_2 can be determined.
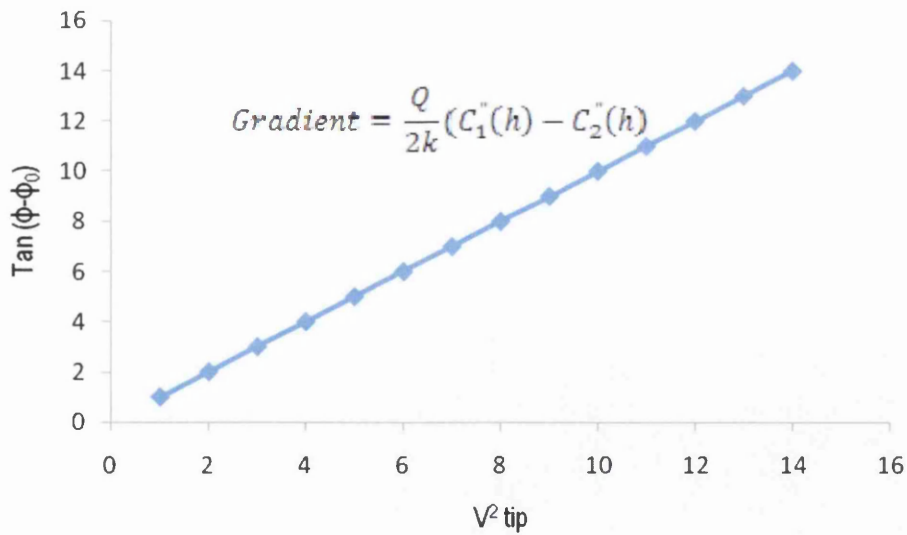
Figure 6.16 Graphical representation of the phase difference against the square of the tip bias.

The values for the capacitance of the background substrate and the nanobelt can be used to calculate a value for the dielectric constant for the silicon wafer substrate and for the zinc oxide nanobelt by examining each capacitance separately and then in series as shown in the illustration in figure 6.17.
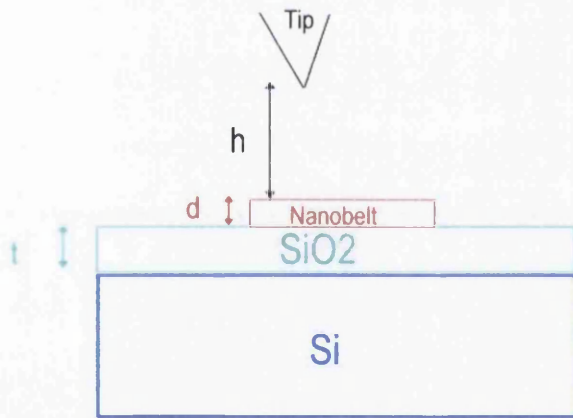
Figure 6.17 Illustration describing the distance h between the tip and the nanobelt, d the height of the nanobelt and t the height of the natural silicon dioxide layer.

Using the diagram illustrated in 6.17 equations for each capacitance can be calculated incorporating the dielectric constants of air ε_0, of the dioxide layer ε_r and the constant for the zinc oxide nanobelt ε_n.

$$C_h = \frac{\varepsilon_0 \pi R^2}{h}$$

Equation 6.8

$$C_d = \frac{\varepsilon_0 \varepsilon_n \pi R^2}{d}$$

Equation 6.9

$$C_t = \frac{\varepsilon_0\,\varepsilon_r\pi R^2}{t}$$

Equation 6.10

The equations outlined above are used to determine an expression for C_2'' by using the expression for dealing with capacitors in series as shown by equation 6.11.

$$\frac{1}{C_2} = \frac{1}{C_h} + \frac{1}{C_d} + \frac{1}{C_t}$$

Equation 6.11

$$C_2 = \frac{\varepsilon_0\pi R^2}{\left[h + \frac{d}{\varepsilon_n} + \frac{t}{\varepsilon_r}\right]}$$

Equation 6.12

Taking the second differential yields equation 6.13 which can be compared to the equation outlined in Staii [1].

$$C_2''(h) = 2\varepsilon_0\pi R^2 \frac{1}{\left[h + \frac{d}{\varepsilon_n} + \frac{t}{\varepsilon_r}\right]^3}$$

Equation 6.13

It is equation 6.13 above which can be used to calculate the dielectric constant of the zinc oxide nanobelt as all the other integers in the equation are known values.

6.5 Phase difference plots and dielectric constant.

The tan of the change in phase against the square of the tip bias were plotted for each of the samples, zinc oxide nanowire and the p and n-type silicon nanowires. These plots were used to determine a value for the dielectric constant for the silicon wafer substrate material and the nanowire itself as shown in section 6.4 above.

6.5.1 Zinc Oxide nanowires

The zinc oxide nanowires are the same as the ones outlined in 6.2 above and the theory described in 6.4 Initially the background phase of the nanobelt was recorded and plotted against the square of the applied tip bias.
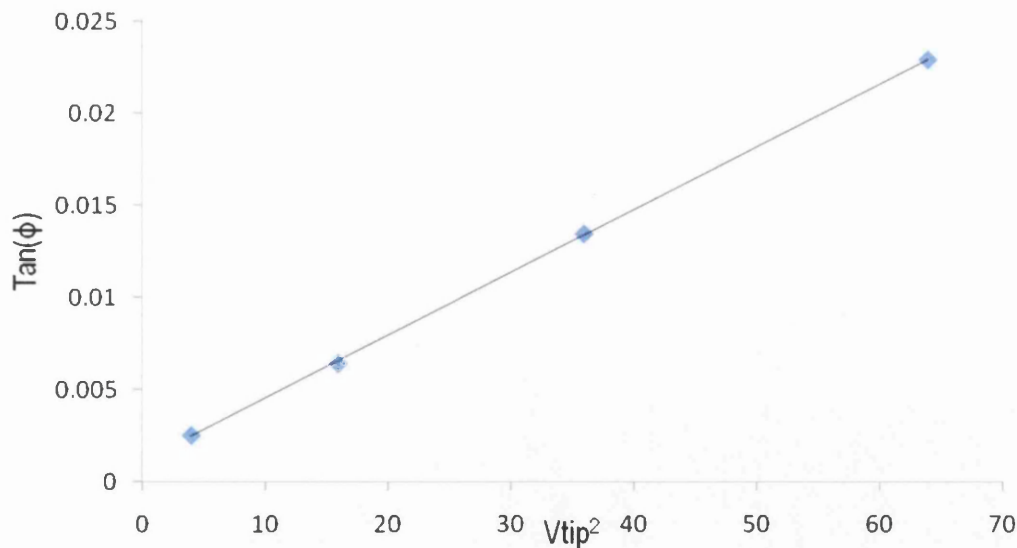
Figure 6.18 Background phase as a function of the square of the applied tip bias omitting the final result.

As described in the theory section the graph shown in figure 6.18 should yield a straight line as the relationship between the phase and the applied tip bias is linear as described by equation 6.2. A trend line was added to the results and the gradient of this result was inputted to equation 6.2. The constants Q and k were given values of 225 and 2.8 as described in the manufacturers guidance. This returned a value for the capacitance of the substrate denoted as $C_1^"$.

The values for the capacitance of the background substrate can be used to calculate a value for the dielectric constant for the silicon wafer substrate as shown in the illustration in figure 6.9 and the final equation 6.7. Using a tip radius of 20nm, a silicon dioxide thickness of 400nm and a lift height of 50nm the dielectric constant of the silicon wafer background was calculated to be 4.26.

The next step is to examine the situation involving the nanowire where the phase difference is measured against the square of the applied tip bias. The phase difference is described as phase over the nanowire minus the background phase. The result is shown in figure 6.19 showing a linear relationship as expected from equation 6.3 with the gradient being used with the value determined for $C_1^"$ to calculate a value for $C_2^"$. This value for the capacitance was then used in equation 6.12 to calculate a value for the dielectric constant of the nanowire. Using a lift height of 50nm, a silicon dioxide thickness of 400nm, a tip radius of 20nm, a nanowire thickness of 65nm and 4.26 for the dielectric constant of the silicon substrate as determined above gave a value for the nanowire dielectric constant of 0.24. The value given

in literature for the dielectric constant of bulk zinc oxide is between 1.7 and 2.5 which is larger than the value calculated for the zinc oxide nanowires.
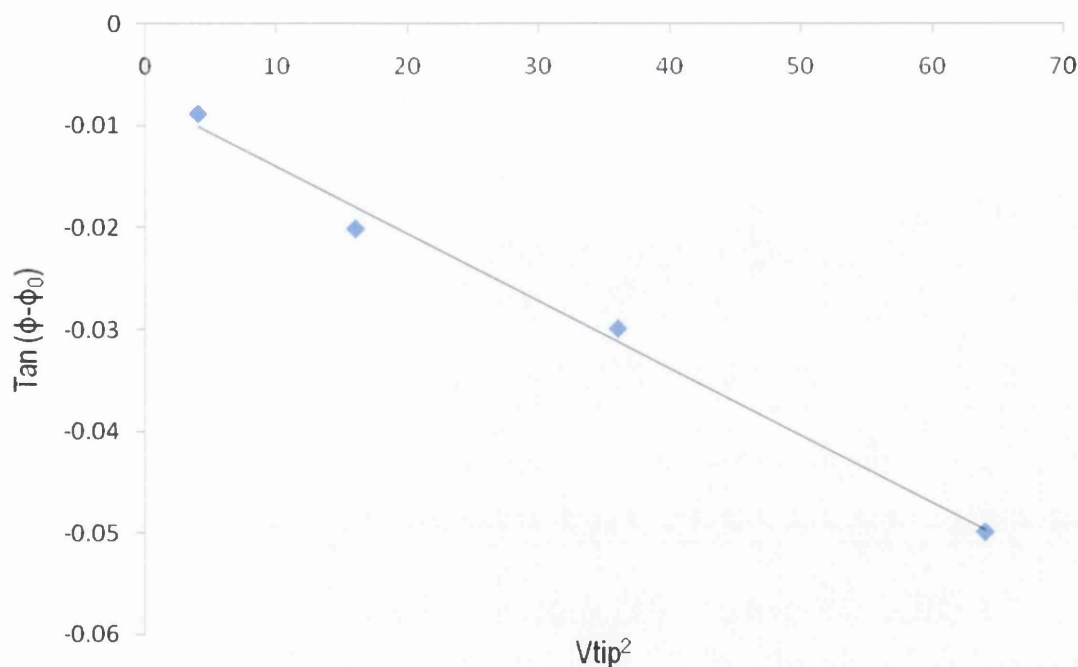
Figure 6.19 Graphical results of the tangent of the phase difference against the square of the applied tip bias.

6.5.2 N-type Silicon Nanowires

The n-type silicon nanowires were examined in a similar way to the zinc oxide nanowire and they were examined individually. Nanowire 1, 3 and 4 were imaged on the same scan so it is acceptable to use the same values for the background phase for all three nanowires. Firstly by examining the tangent of the background phase against the square of the applied tip bias as shown in figure 6.18 a value for the capacitance, c_1''. As shown by the equation 6.2 the relationship between the applied tip bias and the background phase should be linear and the values for Q and k are 225 and 2.8 respectively. This value for c_1'' was then used in equation 6.7 and using the tip radius of 20nm, a lift height of 50nm and a silicon dioxide thickness of 400nm gave a value of 3.63.
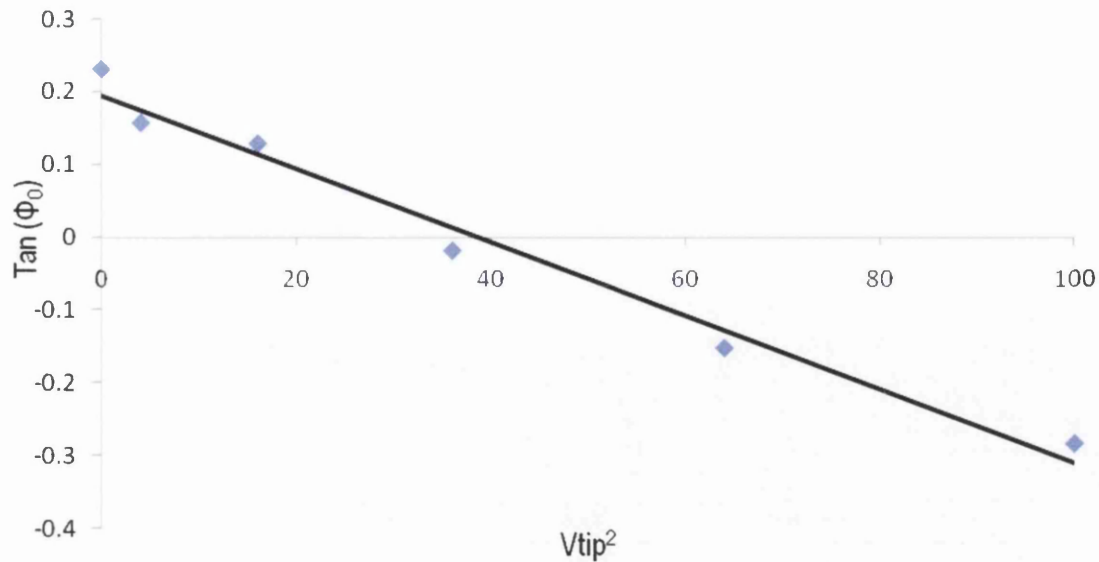
Figure 6.20 Graphical results for the tangent of the background phase against the square of the tip bias for n-type nanowire 1.

The phase difference was calculated by taking multiple measurements of the phase over the silicon nanowire at different points in order to get a more reasonable value. The phase of the background was subtracted from the phase of the nanowire to generate a value for the phase difference and this value was plotted against the square of the applied tip bias. The graphical result is shown in figure 6.21.
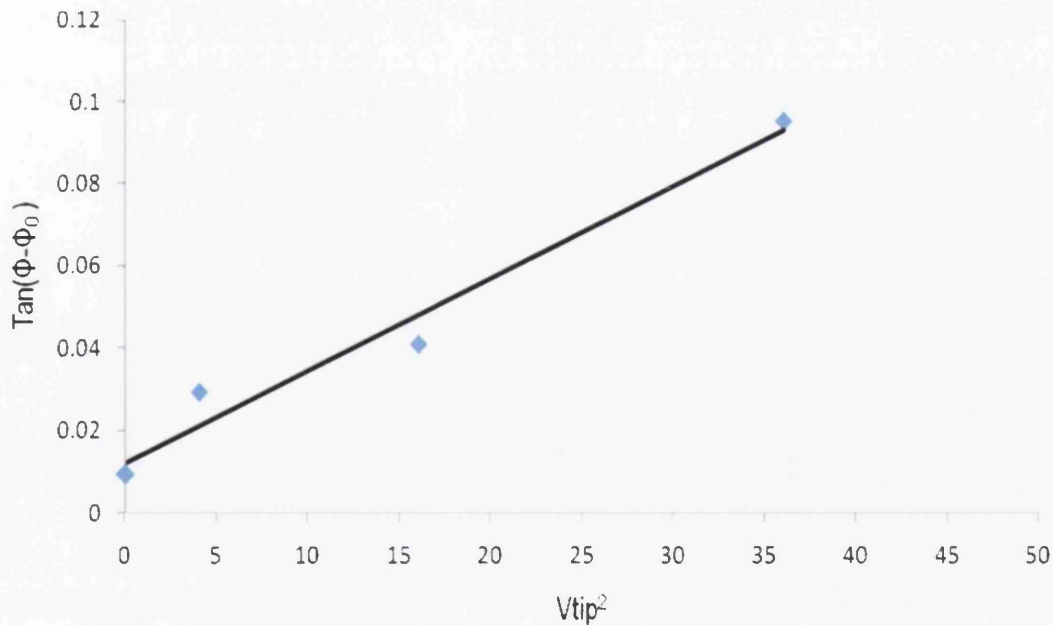
Figure 6.21 Phase change against square of the applied tip bias for n-nw1.

The gradient of the trend line in figure 6.21 was used to determine a value for C_2'' using the value previously calculated for C_1''. This value for C_2'' was then used in equation 6.13 with the tip radius of 20nm, the lift height of 50nm and a silicon dioxide thickness of 400nm in order to calculate a value for the dielectric constant for n-type nanowire 1. The thickness of this nanowire was also used in the equation and was measured to be 70nm, this gave a dielectric constant for the nanowire 1 to be 5.59.

N-type nanowire 2 background phase was examined and as it was captured on a separate image from the other three nanowires the background phase also needs to be examined. The background phase against the square of the tip bias for nanowire 2 is shown in figure 6.22. The trend line shows the linear relationship between the tangent of the phase and the tip bias and the capacitance of the silicon substrate was determined.
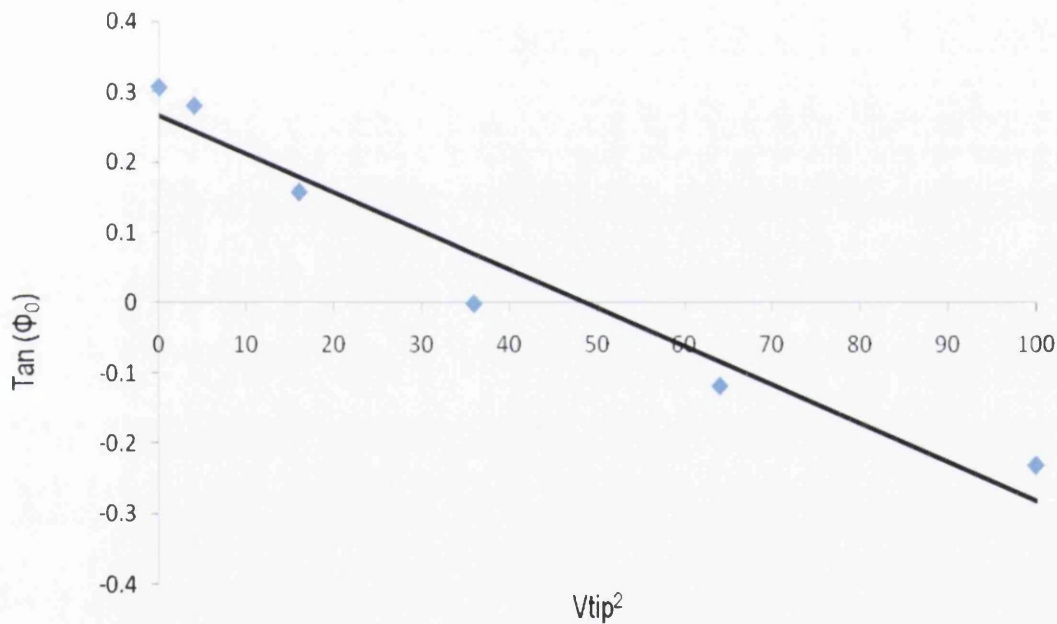
Figure 6.22 The background phase against the square of the tip bias for n-type nanowire 2.

This value for C_1'' was used to determine the dielectric constant for the silicon wafer to be 5.03 by using the equation 6.7 with values for the silicon dioxide layer thickness as 400nm, lift height of 50nm and a tip radius of 20nm.
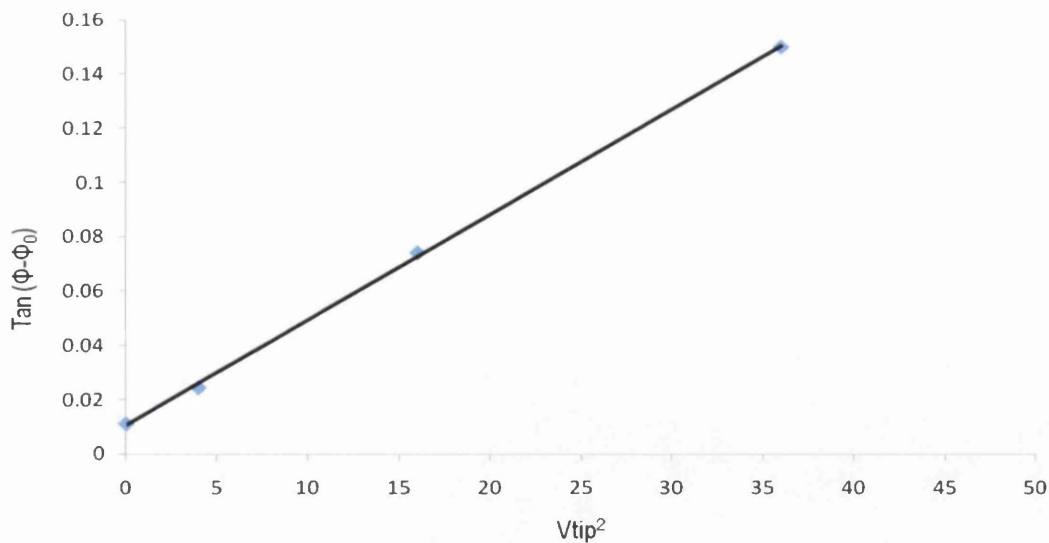
Figure 6.23 The phase difference against applied tip bais for n-type nanowire 2.

The phase difference against the square of the applied tip bias is shown in figure 6.23 with a trend line added. The gradient of this trend line can be used to determine the capacitance, C_2'' according to equation 6.3 and using the value calculated previously for C_1''. The value for the dielectric constant for nanowire 2 was determined to be 4.9.

Nanowire 3 and 4 are on the same scan as nanowire 1 therefore there is no need to be examined again and hence only the phase difference was explored for these two nanowires. The dielectric constant for nanowire 3 was determined by the same process as used previously and outlined in section 6.4. The dielectric constant for n-type nanowire 3 was calculated to be 3.04 from the graph shown in figure 6.24.
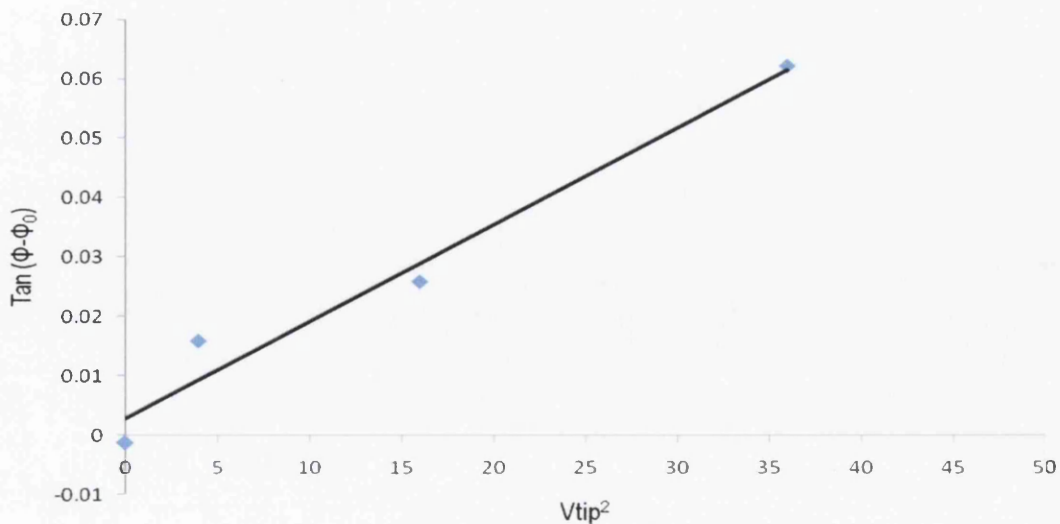
Figure 6.24 The phase difference against the square of the applied tip bias for n-type nanowire 3.

The dielectric constant for n-type nanowire 4 was determined from the graph shown in figure 6.25 and from the theory outlined above. The dielectric constant was calculated to be 5.08.
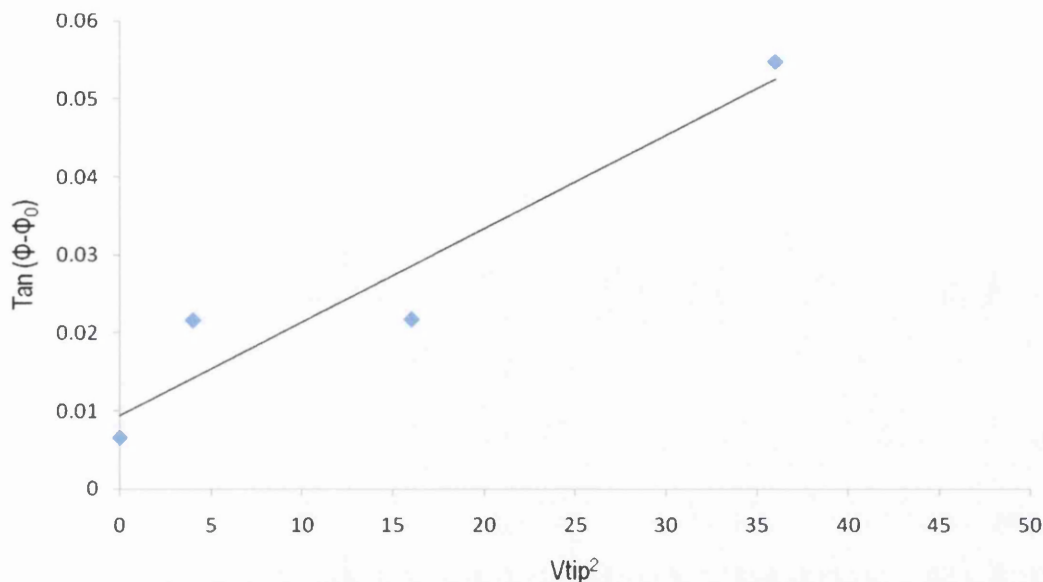
Figure 6.25 The phase difference plotted against the square of the applied tip bias for n-type nanowire 4.

6.5.3 P-type Silicon Nanowires

The p-type silicon nanowires were examined in the same way as the n-type by exploring the background phase and the phase difference against the square of the tip bias and using the equations described in the theory section of this chapter.

The background phase of p-type nanowire 1 against the square of the applied tip bias is shown in figure 6.26 below. The trend line shows that the results demonstrate a linear relationship and the equation 6.2 can be applied to calculate a value for the capacitance.
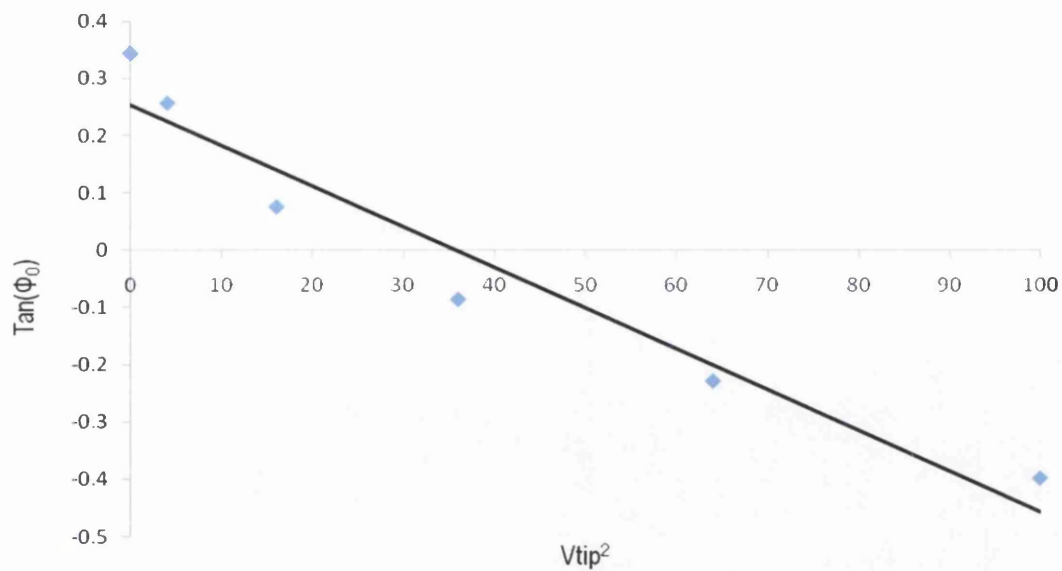
Figure 6.26 The background phase plotted against the applied tip bias for p-type nanowire 1.

The value for the capacitance was usd to calculate a value for the dielectric constant of the silicon substrate. The dielectric constant for the substrate was found to be 3.79.

The next stage is examining the phase difference which is the phase of the nanowire minus the phase of the background (figure 6.27) in order to determine the dielectric constant of the nanowire. The dielectric constant for the nanowire was calculated to be 6.25.
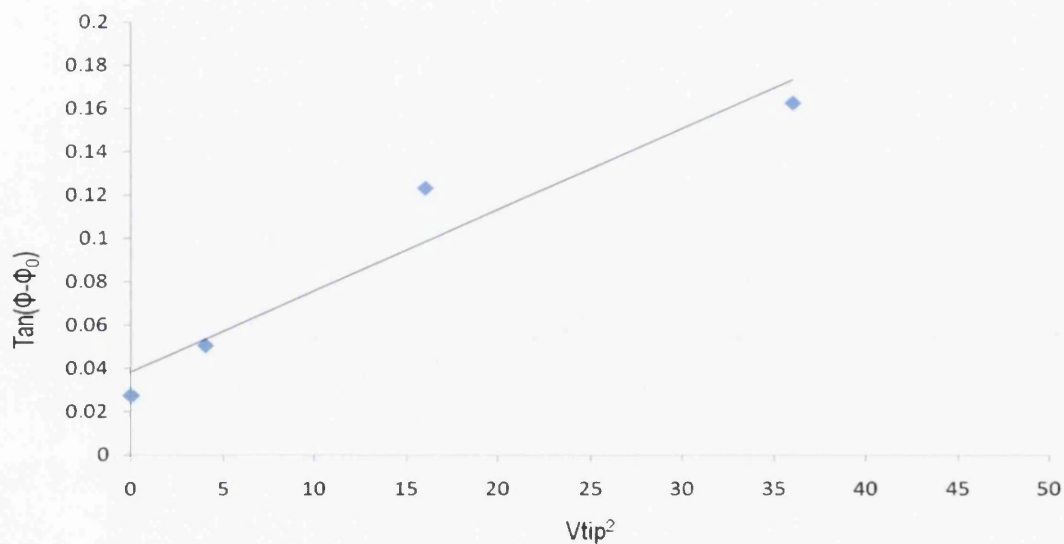
Figure 6.27 The phase difference against the square of the applied tip bias for p-type nanowire 1.

Nanowire 2, 3 and 4 are all shown on the same EFM image therefore it is feasible to only examine the background phase for nanowire 2 and use the same value for the capacitance to determine the dielectric constants for each nanowire.
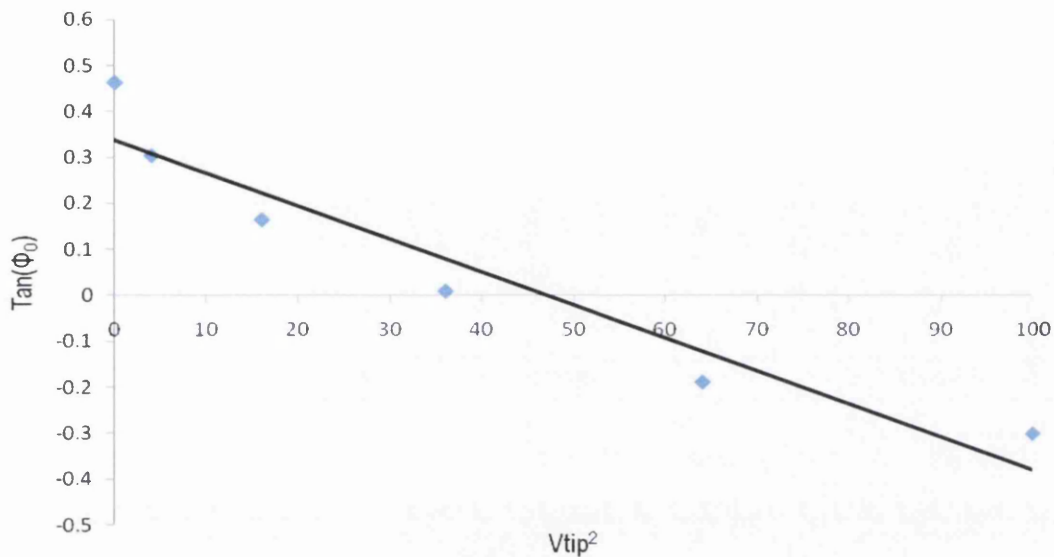
Figure 6.28 Graphical result of the background phase against the square of the applied tip bias for p-type nanowire 2.

The capacitance of the background was calculated from the data shown in figure 6.28 and this was used to determine a value for the dielectric constant of the silicon substrate which was 3.96.
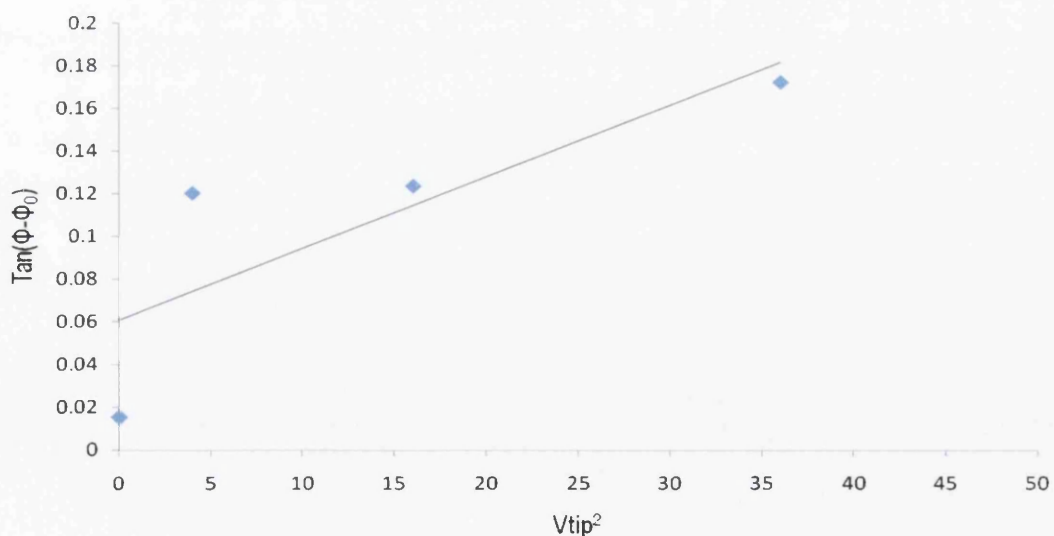
Figure 6.29 The phase difference against the applied tip bias for p-type nanowire 2.

From examining the data in figure 6.29 of the phase difference against the square of the applied tip bias the capacitance for nanowire 2 was calculated. Using this value for the

capacitance and the value determined for the background the dielectric constant calculated for nanowire 2 was found to be 16.93.

Nanowire 3 and 4 are on the same EFM scan as nanowire 2 and therefore the background value for the substrate determined above for nanowire 2 can be applied to nanowires 3 and 4. The phase difference for nanowire 3 plotted against the square of the applied tip bias is shown in figure 6.30. The dielectric constant was calculated as previously shown and was determined to be 11.76.
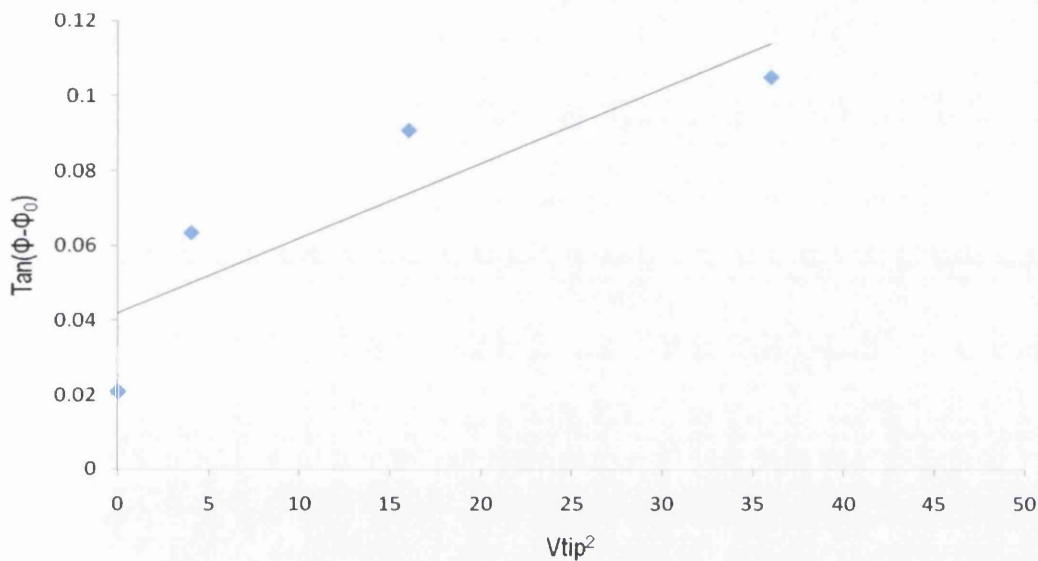
Figure 6.30 The phase difference against the applied tip bias for p-type nanowire 3.

The result for p-type nanowire 4 is shown in figure 6.31 and the dielectric constant was determined from equation 6.13 to be 4.02.
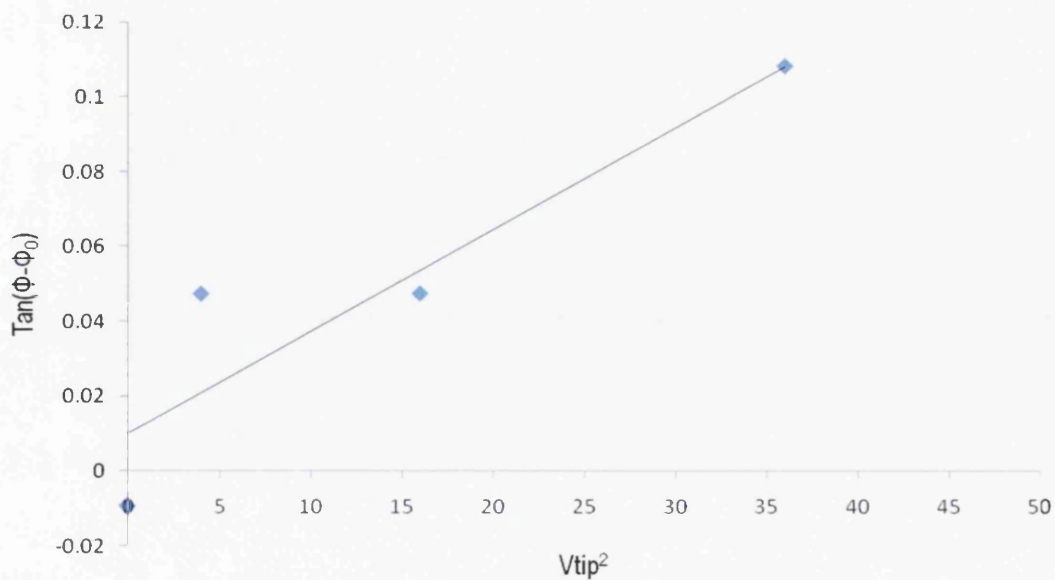
Figure 6.31 The phase difference against the square of the applied tip bias for p-type nanowire 4.

The results illustrated above show huge changes in the dielectric constants derived for each nanowire. The only difference between the two types of nanowires is the dimensions of individual wires. The dimensions of the wires could have more of an impact on the dielectric constant than first thought, which could lead to the surface to volume ratio of the wires having an influence over the phase difference of the nanowire and hence the dielectric constant.

6.6 Polarisation and Charge migration

The tip bias was increased from 0 to -10V in increments of 2V and the resultant phase change is shown in figure 6.32. The phase difference (Φ-Φ_0) is the measured phase over the nanobelt minus the background phase to give a true phase result for every tip bias. At a tip bias of -2V to -8V the phase difference is a negative value which indicates a repulsive force. The subtle increase in negativity of the phase and the increasing repulsive force is due to movement of the charge carriers within the nanobelt. When a tip bias of -8.6V is applied the phase difference suddenly exhibits a positive value indicative of an attractive force. This would suggest that at a tip biases over -8.6V the corresponding field between the tip and the nanobelt is strong enough to disrupt the electron clouds and induce a dipole within the nanobelt resulting in an attractive force. In order to understand this effect the interaction of the biased tip with the nanobelt during scanning needs to be explored.

The results shown in figure 6.32 where the nanowire is seen becoming brighter as the applied tip bias increases has been observed previously by Zdrojek et al and is outlined in section 3.5.1 [4]. The results showed the carbon nanotube when being imaged using AFM as a dark line on a relatively light background. However when an applied tip bias was used then the nanotube appears much brighter than previously.
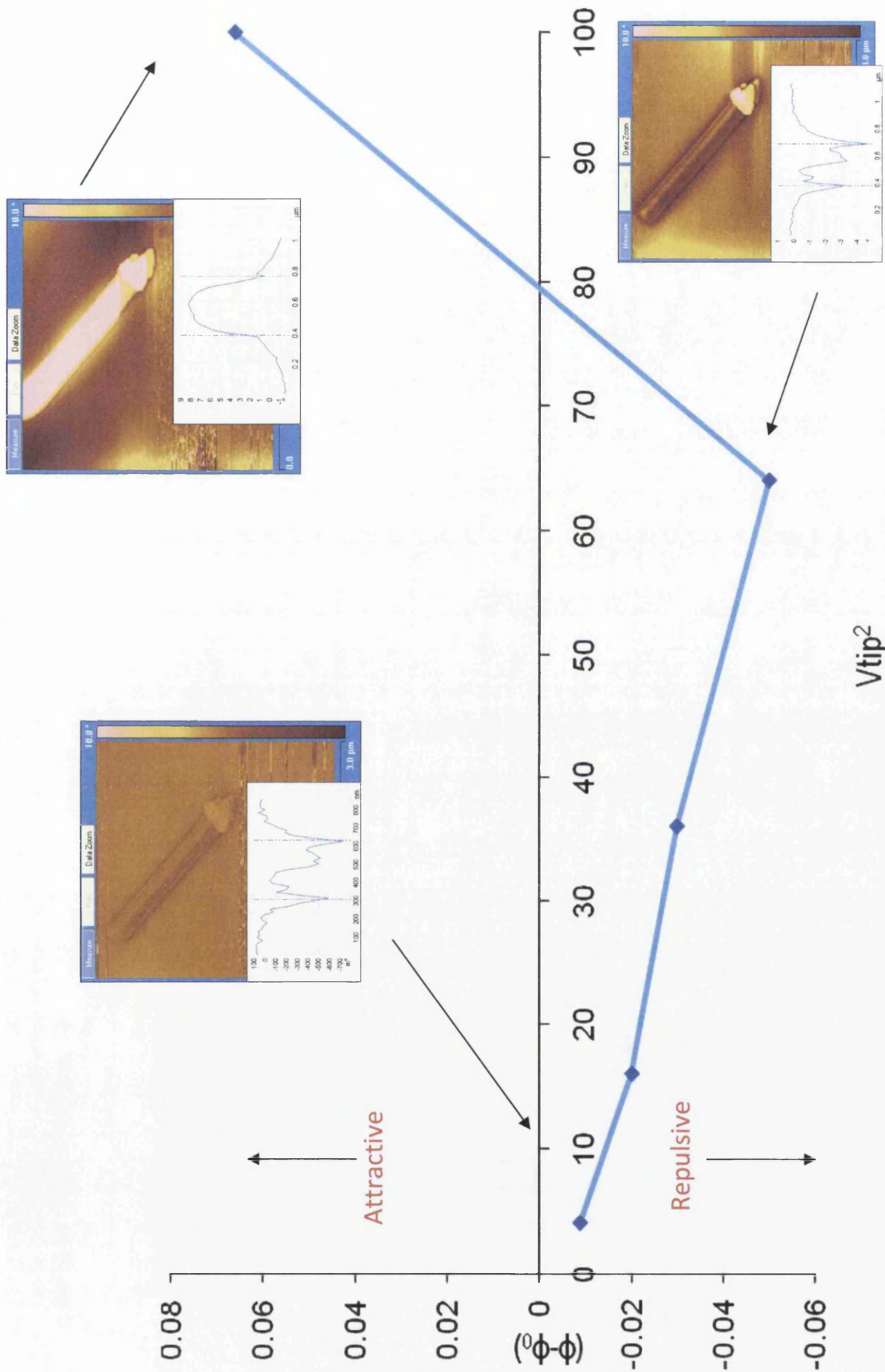
Figure 6.32 Phase difference with changing tip bias of Zinc Oxide nanobelt illustrating the change in sign of phase from a replusive force to a positive force.

This apparent charging has also been observed with silicon nanoparticles where the nanoparticles were examined using both negative and positive tip biases [5]. When a positive tip bias was used not much definition was observed. However it did show the ability to hold the charge over a period of time.

When the tip is scanning up to the nanobelt the tip begins to have an effect on the charge carriers within the nanobelt. The repulsive electrostatic force of the tip is sensed by the charge carriers in the nanobelt and they are subsequently repulsed to the furthest side of the nanobelt as illustrated in figure 6.33 (a) where the migration of charge carriers is shown schematically. As the repulsive tip scans, more of the tip is interacting with the charge carriers in the nanobelt and hence the electrostatic repulsion separates the charge carriers to the edge of the nanobelt as illustrated in figure 6.33 (b) where there is charge migration to the outer edges of the nanobelt. The tip reaches the furthest side of the nanobelt and the opposite effect is seen to that in (a) and is illustrated in figure 6.33 (c). The negatively charged tip causes electrostatic repulsion of the charge carriers which migrate to the opposite side of the nanobelt from the tip.

In all of the scenarios described in figure 6.33 only a fraction of the charge carriers interact, as the voltage applied to the tip is not enough to cause all the charge carriers within the nanobelt to interact with the tip. As shown in figure 6.32 the point at which the tip voltage is enough to influence all the charge carriers in the nanobelt occurs when the applied voltage is greater than -8.6V.

-V

(a)

Migration

Nanobelt
+ + + + + + + - -
+ + + + + - - - -
+ + + - - - - - - -

Substrate
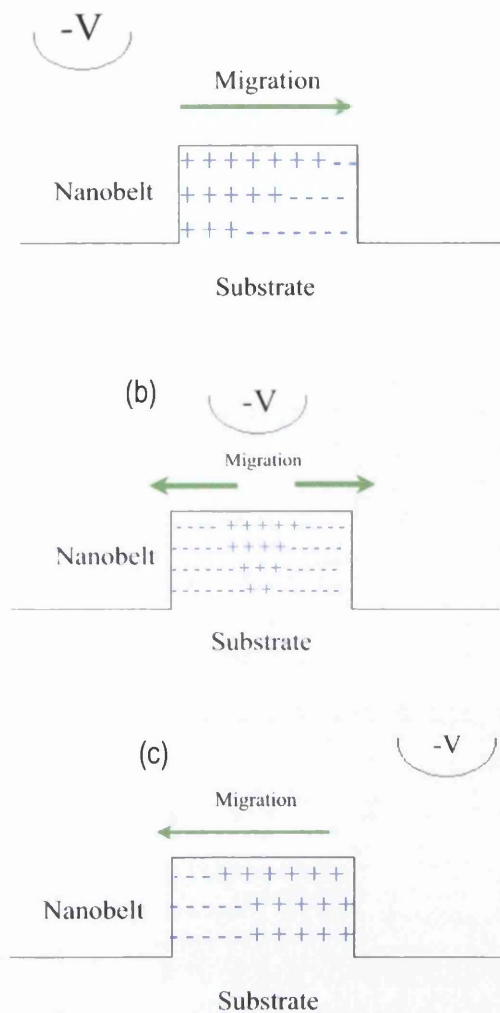
EFM tip is on the left hand side of the nanobelt and is causing a resultant migration of charge carriers to the right caused by electrostatic repulsion.

(b)

-V

Migration

Nanobelt
- - - - + + + + + - - - -
- - - - + + + + - - - - -
- - - - - + + + - - - - -
- - - - - - + + - - - - - -

Substrate

EFM tip is located directly above the nanobelt and causing a migration of charge carriers to either side of the nanobelt due to electrostatic repulsion.

(c)

-V

Migration

Nanobelt
- - - + + + + + +
- - - - - + + + + +
- - - - - + + + + +

Substrate

The EFM tip has reached the other side of the nanobelt and causes the opposite effect from (a) by repulsive interaction with the charge carriers.

Figure 6.33 The interaction between tip and nanbelt during a raster scan (a) before the tip reaches the nanobelt, (b) when the tip is directly over the nanobelt and (c) when the tip has reached the other side of the nanobelt.

When this point is reached there is an attractive force between the nanobelt and the tip which is explained in figure 6.33 where all the charge carriers interact and an induced dipole is created within the nanobelt. This completely separates the negative charge carriers and they are electrostatically repulsed into the bulk of the nanobelt furthest away from the negatively biased tip. This pushes the positive charges to the surface and creates an attractive force between these and the negatively charged tip which accounts for the positive force and the positive phase difference illustrated in figure 6.34.
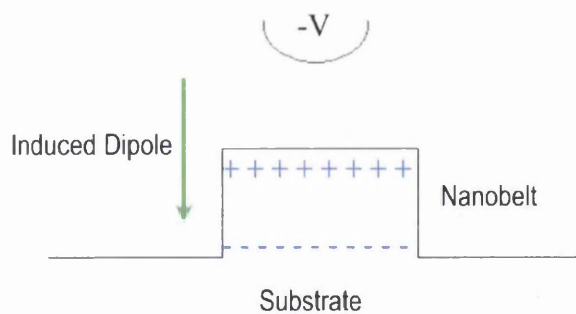
Figure 6.34 The interaction between the tip with an applied voltage of -10V and nanobelt showing the resultant induced dipole.

As the tip scans over the nanobelt it is important to examine the line profiles obtained which illustrate a clear "dip-rise-dip" profile as shown in figure 6.35. This observed behaviour is due to the position of the tip in relation to the nanobelt and the contribution that the tip experiences from the substrate surface.
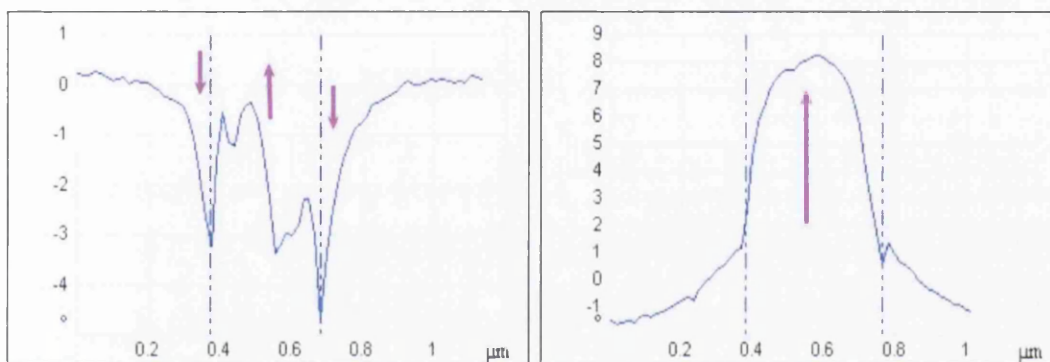
Figure 6.35 (a) A line profile showing the phase change observed with a tip bias of -8V and (b) line profile illustrating the positive only phase change associated with a tip bias of -10V.

There appears to be a dip in the line profile before the nanobelt, a rise when the tip senses the middle of the nanobelt and another dip at the otherside of the nanobelt. However when the tip bias is over -8.6V the line profile looks remarkably difference and no longer shows the dips but just one large rise. The dip rise dip profile has been previously seen by Jespersen and Nygard in Nano Letters [6]. The diagram in figure 6.36 is a line profile scan across a carbon nanotube loop with an applied tip bias of -5V. The line profile is almost identical to that seen in figure 6.35 (a) with the dip-rise-dip characteristic shape. The labels Φ_I and Φ_{NT} refer to the phase over the loop and the phase where by the tip passes over a nanotube.
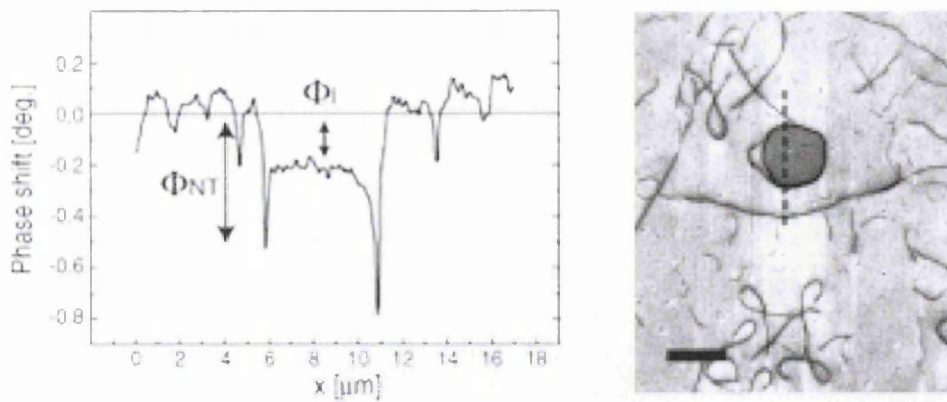
Figure 6.36 (a) line scan over carbon nanotube loop and (b) EFM image of carbon nanotube loop.

This behaviour can be atttibuted to the difference in size of the tip compared to the size of the nanobelt. The diameter of the tip is much smaller than the size of the nanobelt and therefore experiences electrostatic force from the substrate whilst also sensing part of the nanobelt. This means that the tip experiences contributions from both the tip and the substrate when imaging the side of the nanobelt and not directly above it. This is explained in the diagram in figure 6.37. When at the side of the nanobelt the tip experiences an electrostatic force from the nanobelt (Ftz) and an additional contribution from the substrate (Fts). This additional contribution would account for both dips in the line profile and account for the bending of the line profile as seen in 6.35.
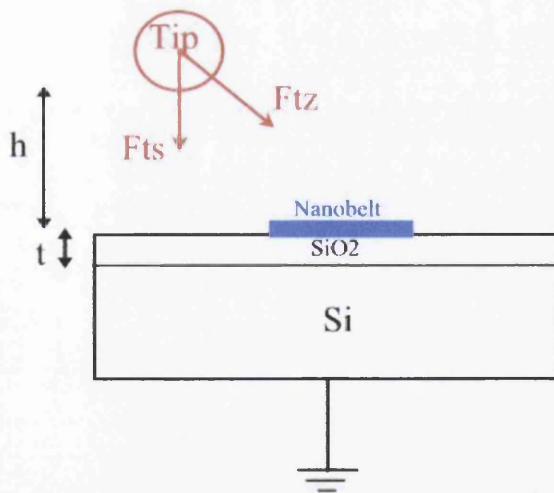
Figure 6.37 Diagram illustrating the electrostatic force experienced tip from the nanobelt (Ftz) and the additional contribution from the sample (Fts).'h' is the tip height , and the depth of native oxide layer is 't'.

6.7 Summary

As described in chapter 3 the samples of zinc oxide nanowires and silicon n and p type nanowires were explored using electric force microscopy (EFM). The data recorded was in the format of phase data taken at various tip biases and is detailed in line profiles and phase images. A value for the capacitance of zinc oxide nanobelts and silicon nanowires were derived and from this a value for the dielectric constant was calculated and compared to the available values for the bulk dielectric constants. The substrate of silicon wafer was calculated to have a dielectric constant of 4.26 and this result showed a good agreement with the literature of 3.9. The calculated value for the zinc oxide nanowire was calculated to be 0.24 and the literature value was 1.7 to 2.2. Similarly a value was calculated for the silicon nanowires of 5.59 and 4.02 for n and p-type respectively which was also in good agreement with available literature values.

The zinc oxide nanowires also appeared undergo a change attributed to a charging mechanism whereby local charge carriers are polarized and results in charge migration.

6.8 References

1.   Staii C., Johnson Jr A. T., and Pinto N., *Quantitative Analysis of Scanning Conductance Microscopy.* Nano Letts, 2004. **4**(5): p. 859-862.

2.   Tan M. T. T., *One dimensional ZnO Nanostructures as Biosensor*, in *Department of Engineering.* 2009, Swansea University: Swansea.

3.   Riedel C., et al., *Determination of the nanoscale dielectric constant by means of a double pass method using electrostatic force microscopy.* J. Appl. Phys., 2009. **106**(024315).

4.   Zdrojek M., et al., *Charging and discharging processes of carbon nanotubes probed by electrostatic force microscopy.* J. Appl. Phys, 2006. **100**(114326): p. 1-10.

5.   Melin T., Deresmes D., and Stievenard D., *Charge injection in individual silicon nanoparticles deposited on a conductive substrate.* Appl. Phys. Letts, 2002. **81**(26): p. 5054-5056.

6.   Jespersen T. S. and Nygard J., *Charge Trapping in carbon nanotube loops demonstrated by electriostatic force microscopy.* Nano Letts, 2005. **5**(9): p. 1838-1841.

Chapter 7

ZnO Nanowire Device

Synthesis and Characterisation

7.1 Introduction

This chapter provides an overview of the results obtained from the nanowires deposited on substrates which were prepared by photolithography as outlined in chapter 5 section 5.4. The titanium electrodes were deposited on to glass substrates which had nanowires already deposited, so that the nanowires were underneath the contact pads. This improved conduction of the nanowires when compared to earlier experiments where the nanowires were deposited on top of the electrodes. The titanium electrodes deposited on top of the nanowires were measured to be approximately 150nm thick by analysis using AFM. The samples were characterised using a probe station which varied the voltage applied between -10V and +10V and the corresponding current output was recorded. These results demonstrated the conductive nature of the zinc oxide nanowire devices and allowed the gas sensing capabilities of these devices to be explored in more detail.

7.2 Nanowires deposited on top of Metal Electrodes

A Glass slide with nickel pads in a honeycomb structure (figure 7.1(a)) was used as the substrate for the deposition and subsequent electrical measurements of zinc oxide nanowires. Nanowires were synthesised using a carbon catalyst at a growth temperature of 1100-1200°C using the thermal evaporation technique outlined in chapter 5. The nanowires were dispersed in isopropanol and a few drops of the nanowire solution was deposited using a pipette and then placed on a hot plate to evaporate the solvent. The hot plate was heated to a temperature of 100°C as the isopropanol readily evaporates and therefore an elevated temperature is not required. This method ensured the nanowires were on top of the metal electrodes as shown in the illustration 7.1(b).The slide was then examined under an optical microscope, if only a few nanowires were visible the sample was washed with clean isopropanol and the deposition repeated. A deposition was considered successful where various belts were bridging two contact pads and was very much a trial and error routine. The nickel pads were approximately 50nm thick with a gap of 3μm between each one. The nanowires were examined in situ on the Nickel contact pads by atomic force microscope and were measured to be 7μm in length 700nm in width and 50nm in depth. The photographs shown in figure 7.2 show the honeycomb structure and the view of a nanowire connecting two electrode pads described as a successful deposition.

(a)

(b)
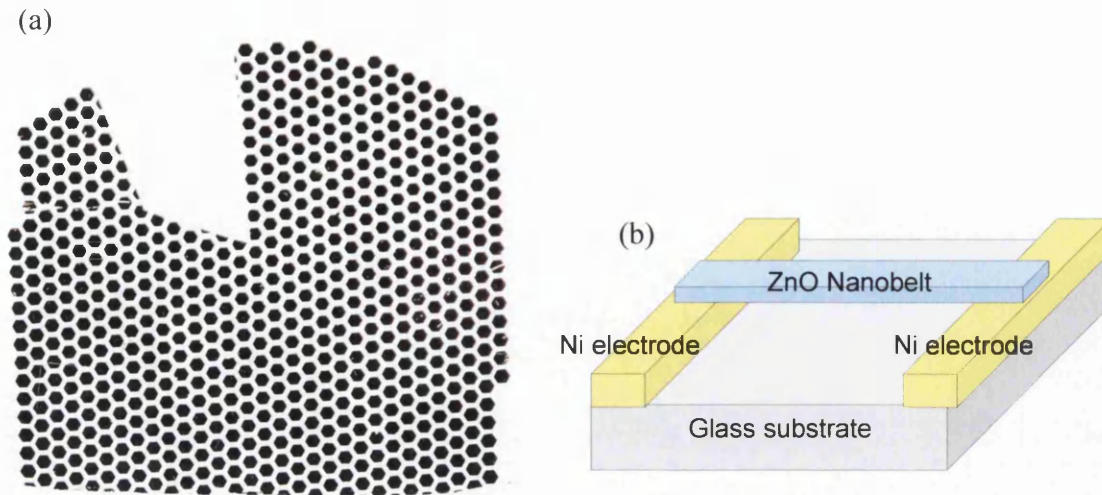
Figure 7.1 (a) Photograph of substrate with nickel electrodes on glass and (b) schematic representation of the nanowire device.

Samples were annealed in vacuum for an hour from room temperature to a maximum temperature of 600°C in 100°C increments and IV measurements were taken in the dark from −10V to +10V for each sample. The measurements were taken in the dark to prevent any contribution from the light of the microscope or natural light having an effect on the conductance. Only a few belts were lost during the repeat annealing process. Figure 7.3 and 7.4 show the IV results from two separate nanowires on the same substrate.
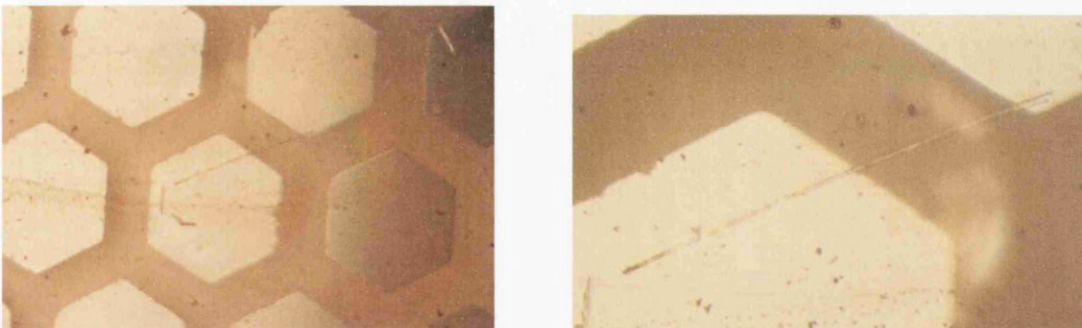
Figure 7.2 Photographs of a single nanowire crossing the gap between two nickel contact pads.

As observed in the graphs (figures 7.3 and 7.4) at room temperature neither of the nanowire showed any conduction and only small improvements were observed after annealing at 100°C. Figure 7.3 shows a marked improvement after the sample was annealed at 400°C (purple line) and the IV results showed ohmic behavior with the recorded current showing a linear relationship

with the increasing applied voltage. From the gradient of this line the resistance for the nanowire can be calculated and was determined to be 16MΩ. The results for annealing at 500°C still show an altered ohmic behavior as the line is not quite linear, however there is still a similar trend present. Before and after these temperatures the sample showed little or no conductance. Figure 7.4 shows conduction again after annealing to a temperature of 400°C (purple line) above and below this temperature the nanowire showed little or no conductance. After annealing at 300°C the nanowire shows conductance when a negative voltage is applied however this drops off when a positive voltage is applied. The curve of the line at around -10V indicates that the nanowire has entered a reverse breakdown point which may have permanently damaged the sample. This is typical behavior seen usually with a diode. Subsequent heating proved detrimental to the network of electrode pads at 700°C.
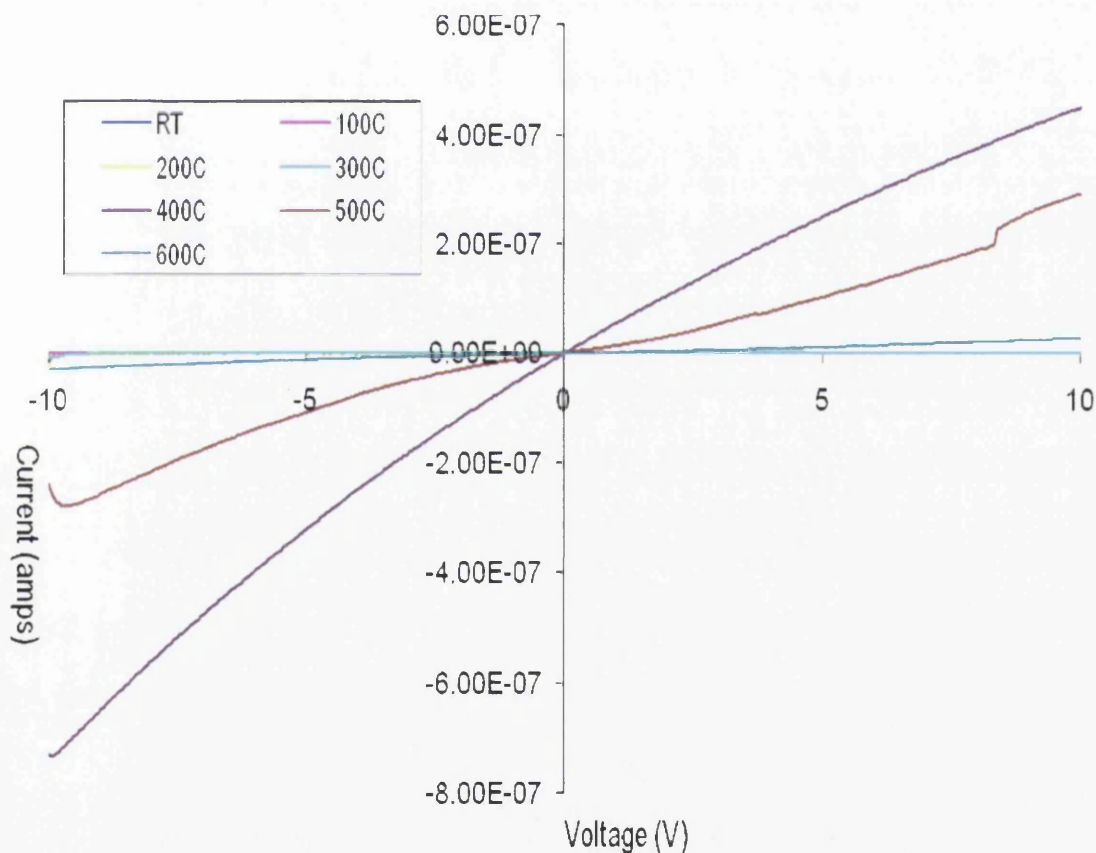
Figure 7.3 Current- Voltage graphical plot of the change in conductance of the same nanowire device after differing annealing temperatures.
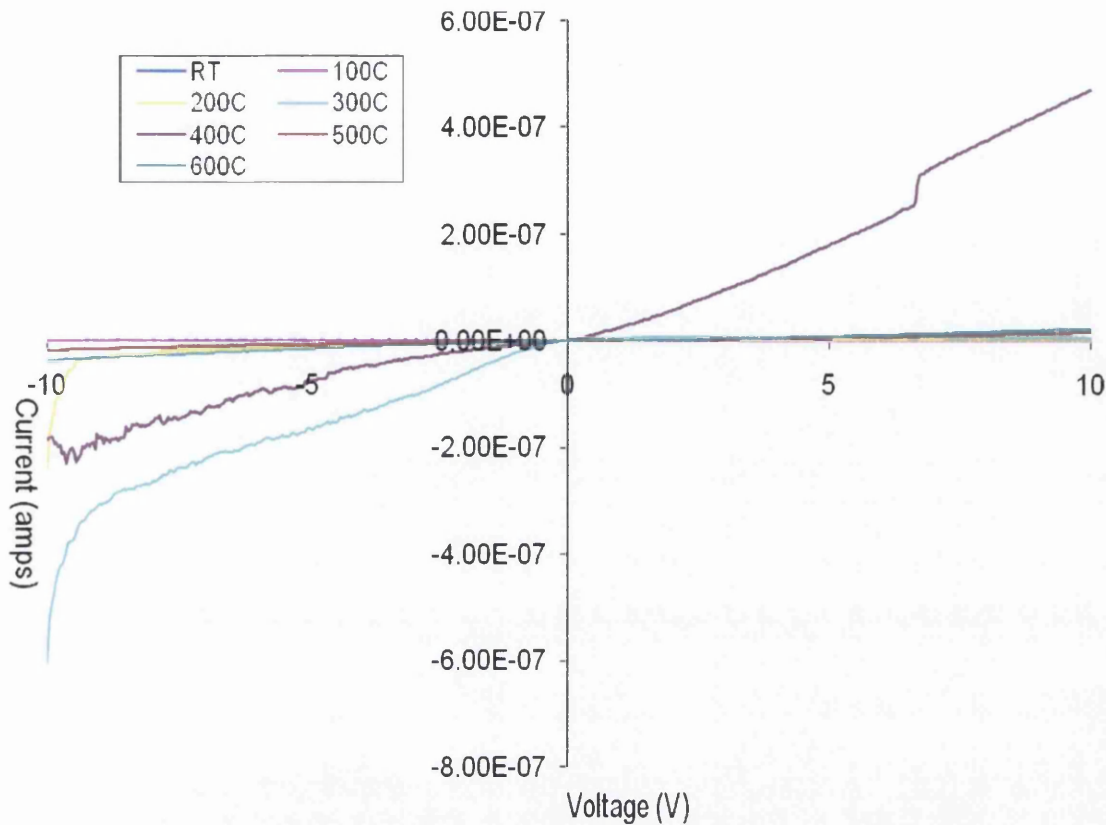
Figure 7.4 Current- Voltage graphical plot of the change in conductance of a different nanowire device after the same device was annealed at varying temperatures.

It is possible that the annealing temperature used allowed the nanowire to make a better contact with the nickel metal pads allowing for better conduction. The samples were annealed in air which could alter the surface chemistry of the nanowire. Some of the gaseous species would undergo desorption and some might bond to the surface of the nanowire. This addition would alter the resistance of the nanowire as it is confined to one dimension. As the samples were allowed to cool naturally down to room temperature it would be doubtful that the increasing temperature had much of an effect on the nanowires molecular structure as any increase in the energy of the charge carriers would have been lost as the sample was cooled and the measurements were taken. The results would suggest that some of this energy remains and allows the charge carriers more energy to interact and hence increase the conductance. The samples were always at the same temperature when measurements were taken therefore the actual bonding between the nickel contact pads and the nanowire would be the only big contribution to the conduction of the

samples. However the melting point of nickel is nearly 1500°C and therefore any amalgamation between the belt and the nickel would not be possible at the annealing temperatures used.

The results shown for the annealing experiments are similar to those published namely Arnold *et al* in Journal of Physical Chemistry B for tin dioxide nanowires [1]. Arnold et al described the increase in measured current output when the sample was annealed at a higher temperature and in vacuum. They attribute this increase to changes in the composition of the surface of the nanowire and that annealing might also desorb other species from the nanowire surface. This would include the presence of water which would mask the nanowire surface and decreasing the sensitivity of the nanowire until the water is removed by evaporation. The presence of water could be a factor in the annealing experiments with zinc oxide nanowire especially as they were annealing in air and not in a vacuum. This would indicate that at lower temperatures water molecules could still be present on the surface of the nanowire and decreasing the sensitivity. Therefore at higher annealing temperatures the current-voltage profile changes and conducts as most of the water molecules masking the surface have been removed at the annealing step.

7.3 Metal contacts formed on top of nanowires

Zinc oxide nanowires were deposited on to glass substrates before the photolithography process (as outlined in chapter 5) was conducted. The titanium metal was deposited at a rate of 1.5Ås^{-1} with an argon gas flow of 40SCCM and the resultant deposit was 150nm thick. The samples were then examined under an optical microscope before imaging successful nanowire-electrode contacts with Dimension 3100 AFM. The nanowires ranged in size (table 7.1) with sample 5 being the longest and widest belt whereas samples 2 and 6 have very similar dimensions. The three successful samples are shown in figures 7.5 (a), (b) and (c) where the AFM images clearly show the nanowire connecting the electrodes, bridging the gap and making good contact with both pads. This was an important step in the characterisation as there were discrepancies between the belts which were seen to be connecting when using the optical microscope and when the same belts were imaged with the AFM. This demonstrates the importance of a technique such as the AFM and its application in experimental data collection and characterisation.

Sample	Nanowire		
	Length	Width	Height
2	30um	700nm	100nm
5	50um	1.2um	200nm
6	35um	759nm	50nm

Table 7.1 Dimensions of the nanowire on each of the three samples.

Each sample was imaged with AFM and the measurements shown in table 7.1 were taken. The titanium electrodes measured to be 150nm in depth and the gap between the electrodes as seen in figures 7.5 is 10µm. This set-up with the nanowires underneath the electrodes is similar to that published by Fan and Lu [2]. Both samples were made using photolithography however Fan etched the contacts using e-beam evaporation.
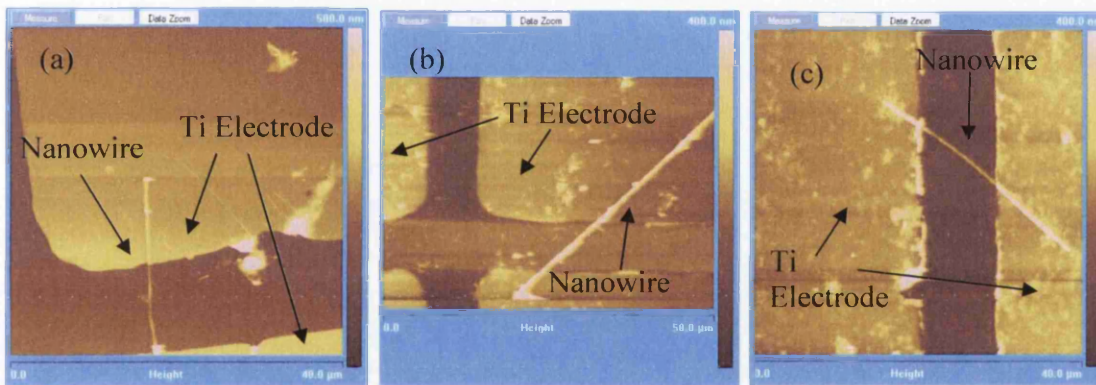
Figure 7.5 AFM images of zinc oxide nanowires bridging titanium electrodes (a) sample 2, (b) sample 5, and (c) sample

7.2.1 Electrical Measurements before wire bonding

The electrical conductance of the nanowires and the connection with the electrodes were tested using a probe station. Each sample was examined by applying a voltage ranging from -10V to +10V and the corresponding current output was recorded. The line profiles are quite noisy in places but all three samples demonstrated conductive behaviour especially, sample 2 (figure 7.8) which shows nearly ohmic behaviour. The other two samples (figures 7.9 and 7.10) did not show any apparent ohmic behaviour however the results do show the nanowires were conducting.
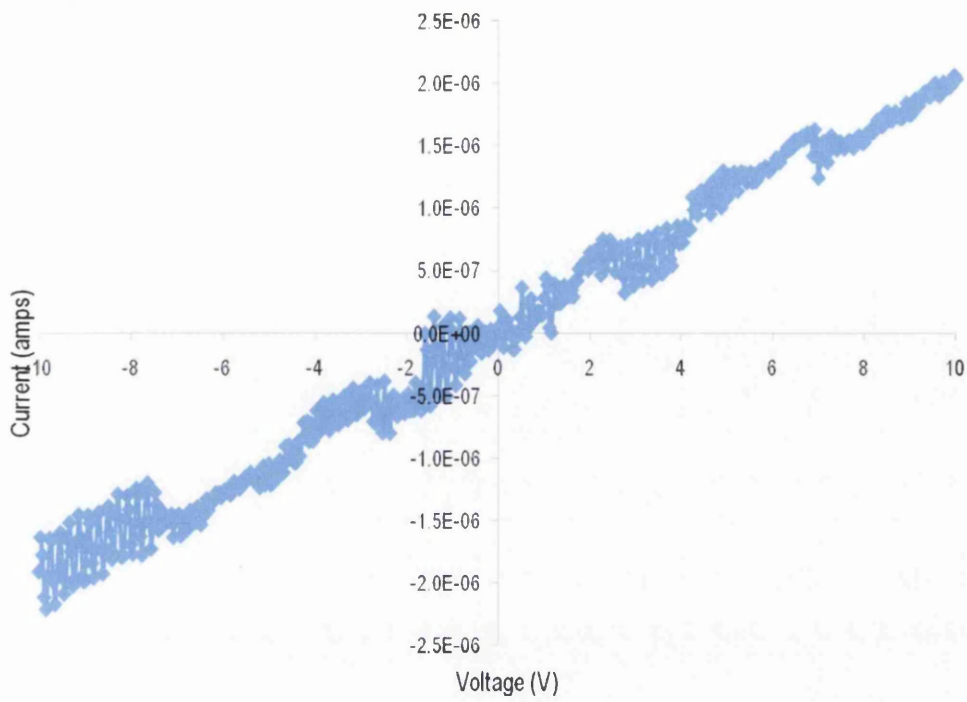
Figure 7.8 IV measurements taken of Sample 2 at room temperature before wire bonding.
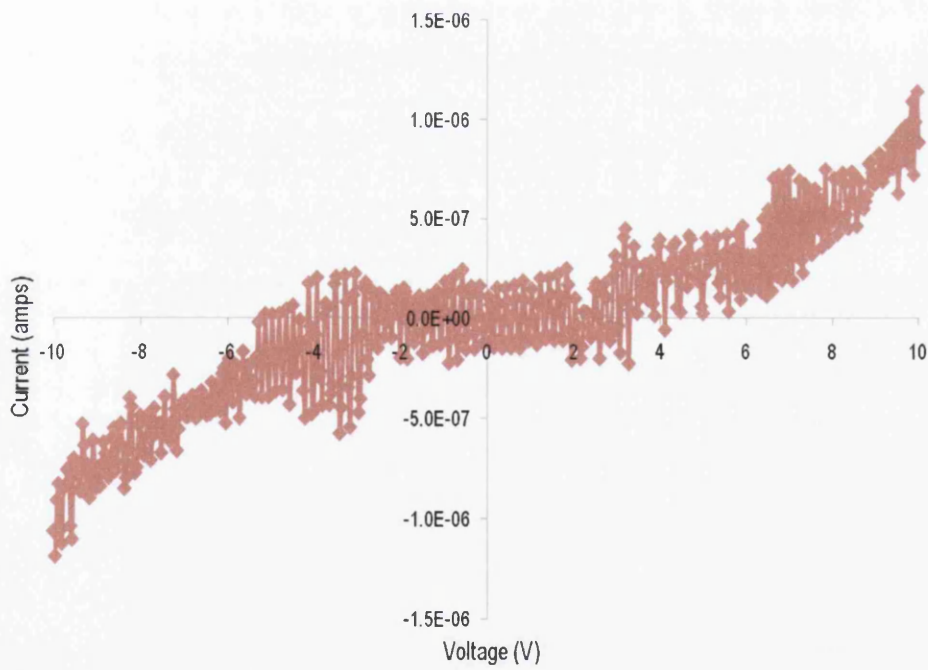
Figure 7.9 IV measurements of Sample 5 before wire bonding recorded at room temperature.
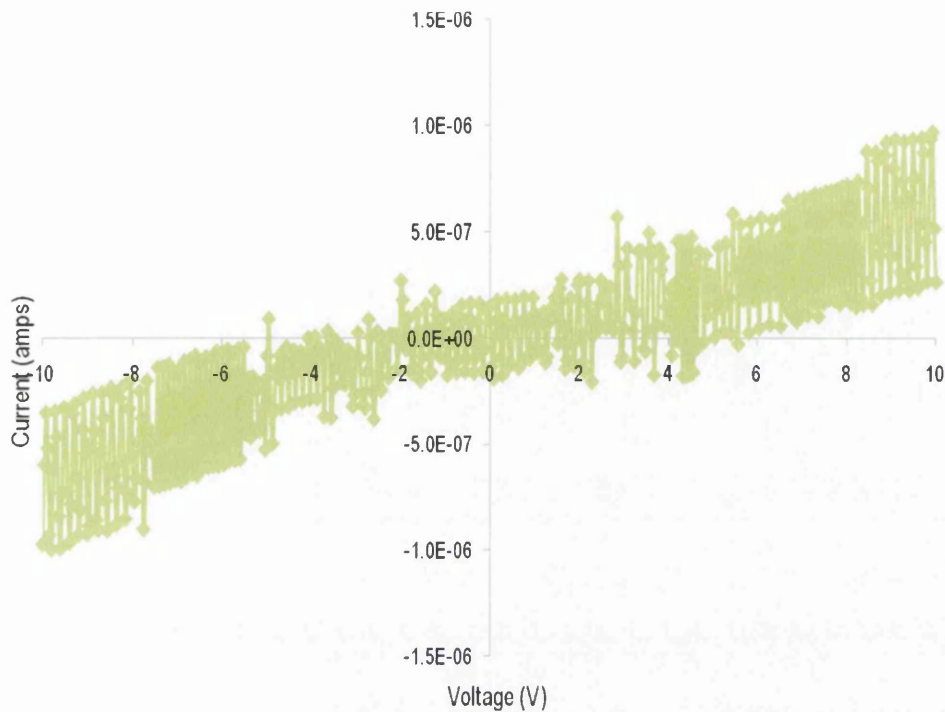
Figure 7.10 IV measurements of Sample 6 taken at room temperature before wire bonding.

7.2.2 Temperature dependent resistance measurements

A Molybdenum wire of diameter 0.125nm was bonded to the electrodes using an electrically conductive silver epoxy. The samples were tested using a probe station and found to be conducting with the wires attached. The samples were then examined with the sample being placed on a hot plate and the wires connected to a Keithley 1000 Multimeter to record the change in resistance as the temperature was increased. The results for each sample are shown below in figures 7.11-7.13.

Sample 2 was heated from room temperature up to a maximum temperature of 162°C over a period of nearly 15 minutes (orange line in figure 7.11). The resistance began to decrease and roughly dropped by half from the measurable maximum of 120MΩ to a minimum of 62MΩ (blue line in figure 7.11). As the temperature decreased the resistance of sample 2 increased over a period of 1 ½ minutes until the maximum was reached.
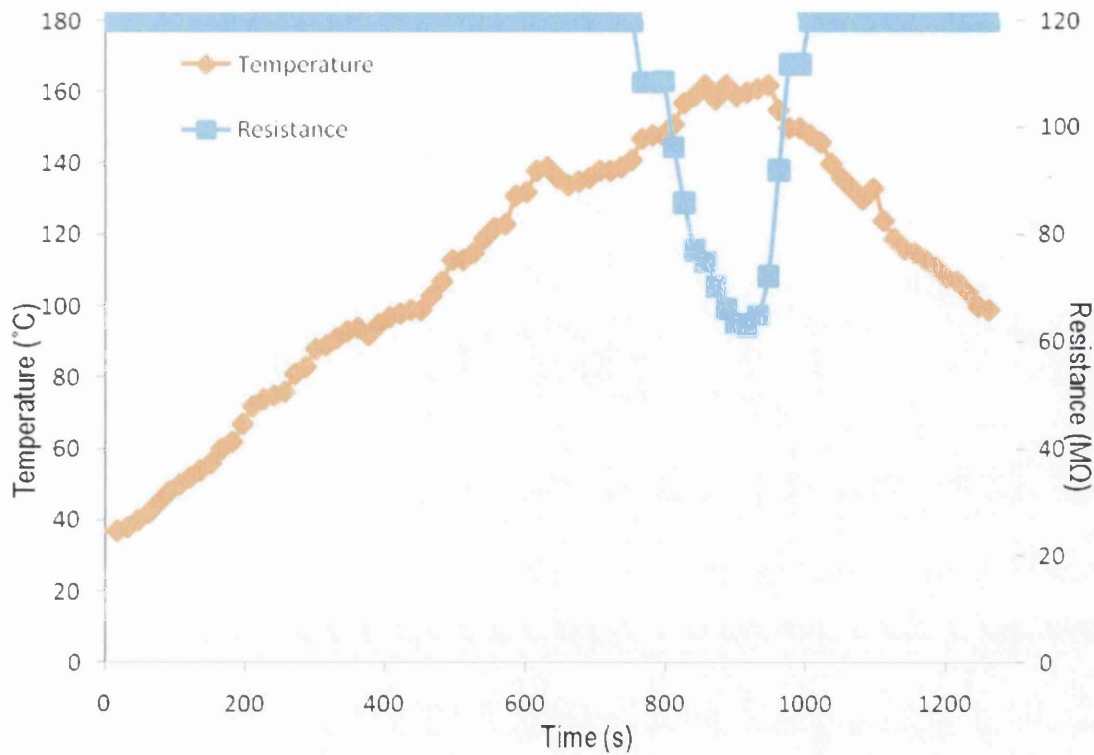
Figure 7.11 Graph to illustrate the change in resistance of Sample 2 with increasing temperature.

Sample 5 was heated from room temperature up to a maximum of 167°C and as observed in figure 7.12 at a temperature of 120°C the resistance of the sample began to decrease. The minimum resistance found was 12.69MΩ (red line figure 7.12). The sample continued to be heated until the temperature reached the maximum and the hot plate was turned off (blue line figure 7.12). As the temperature decreased over time the measured resistance increased until the maximum measurable resistance of 120MΩ was reached.
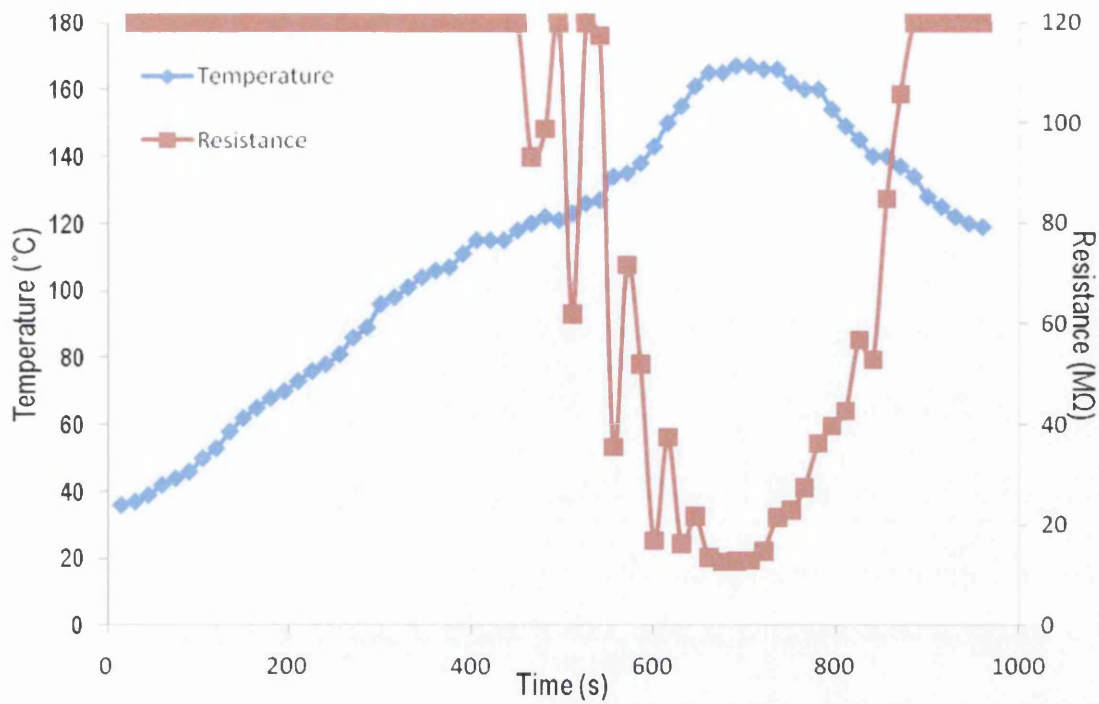
Figure 7.12 Graph to illustrate how the resistance of Sample 5 changes with increasing temperature.

Sample 6 showed similar behaviour to that observed for sample 5 but with a broader lower resistance period than sample 2. At a temperature of 118°C the resistance of this sample began to decrease until the minimum of 24.9MΩ was reached (green line figure 7.13). Again as the temperature decreased from the maximum value of 150°C (purple line figure 7.13) the resistance measured increased until the maximum measurable resistance was observed.
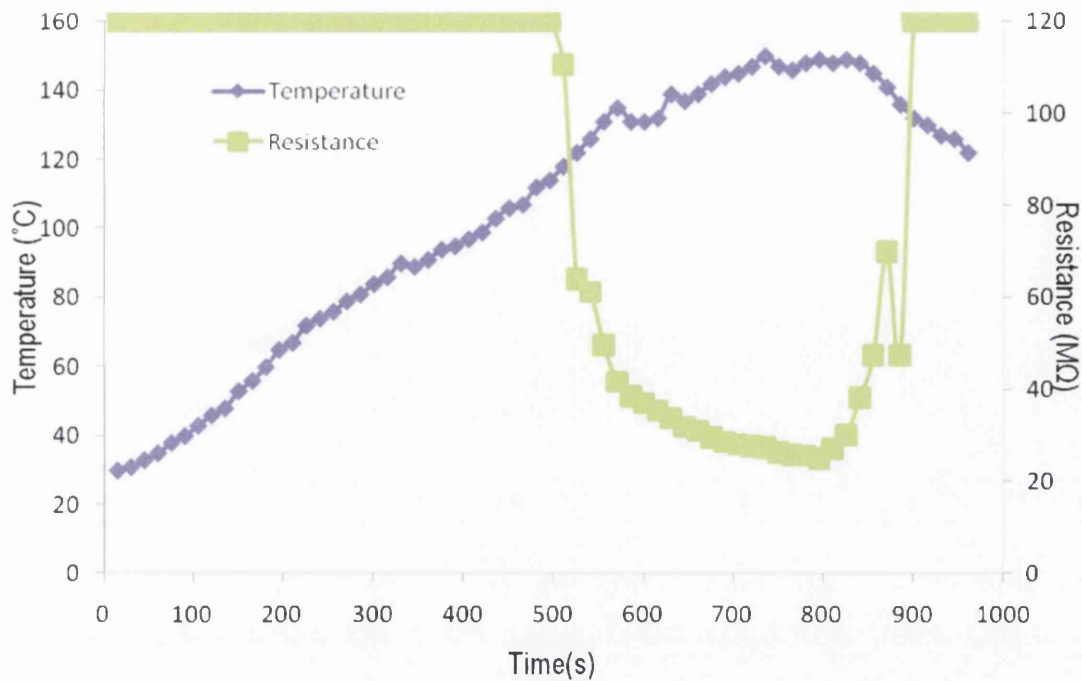
Figure 7.13 Graph to illustrate how the resistance of Sample 6 changes with increasing temperature.

7.2.3 Resistivity calculations

The values for resistivity were calculated from the data shown in figures 7.11-7.13 based on each sample which consisted of a nanowire of differing sizes. The resistivity was calculated using equation 7.1 and using the points in the trough of the resistance graphs shown in 7.11 to 7.13. The initial and final resistance values and the corresponding initial and final resistivity are shown in table 7.2 for each of the three samples.

$$Resistivity = \frac{Resistance \times cross\ sectional\ area}{length}$$ *Equation 7.1*

Sample	Nanobelt				Temperature (°C)		Resistance (MΩ)		Resistivity (Ωm)		
	Height	Length	Width	X-sectional area (m)	Initial	Final	Initial	Final	Initial	Final	Average
2	100nm	30um	0.7um	7x10⁻¹⁴	158	162	70.4	72.2	1.642 x10⁻⁴	1.68x10⁻⁴	1.66x10⁻⁴
5	200nm	50um	1.2um	24x10⁻¹⁴	134	160	35.5	36.2	1.7x10⁻⁴	1.74x10⁻⁴	1.72x10⁻⁴
6	50nm	35um	0.75um	3.795x10⁻¹⁴	135	148	41.7	38.2	4.521x10⁻⁵	4.14x10⁻⁵	4.33x10⁻⁵

Table 7.2 Each nanowire sample with the corresponding values for resistivity as calculated from equation 7.2.

The resistivity values calculated can be compared to values of other materials namely Carbon (3.5×10^{-5} Ωm) and silicon (6.4×10^2 Ωm). As observed from the calculated values the resistivity increases with increasing cross sectional area would be expected from equation 7.1. Therefore as the nanowire becomes longer the resistivity decreases as shown by sample 5 having the longest nanowire and the largest average resistivity.

7.2.4 Gas sensing

The experiment was set up as in the diagram illustrated in figure 5.19 with the gas feed through from one end of the tube and the electrical feed through from the opposite end. The sample proved to be extremely resistive and at room temperature the meter was overloaded at a maximum resistance value of 120MΩ. The chamber which held the sample inside the horizontal tube furnace was at atmospheric pressure. When a steady pressure was observed the temperature was raised inside the furnace and the sample started to conduct at a temperature of 200°C. The results are shown in figure 7.14. The red (210-220°C) and blue (200-210°C) sections on the graph show the resistance dropping as the sample is heated up to a maximum temperature of 220°C. As the temperature is raised from 210°C to 220°C the rate at which the resistance decreases is greater. The resistance decrease at an increasing temperature is due to the increase in the number of thermally generated carriers within the nanowires. The increase in temperature causes a desorption of water vapour and residual gases in particular oxygen species that were adsorbed onto the nanowire surface before the gas sensing experiments. When oxidising gases such as oxygen are removed from the surface of the nanowire, they donate

electrons back into the bulk increasing the number of charge carriers hence reducing the resistance and increasing the conductance.
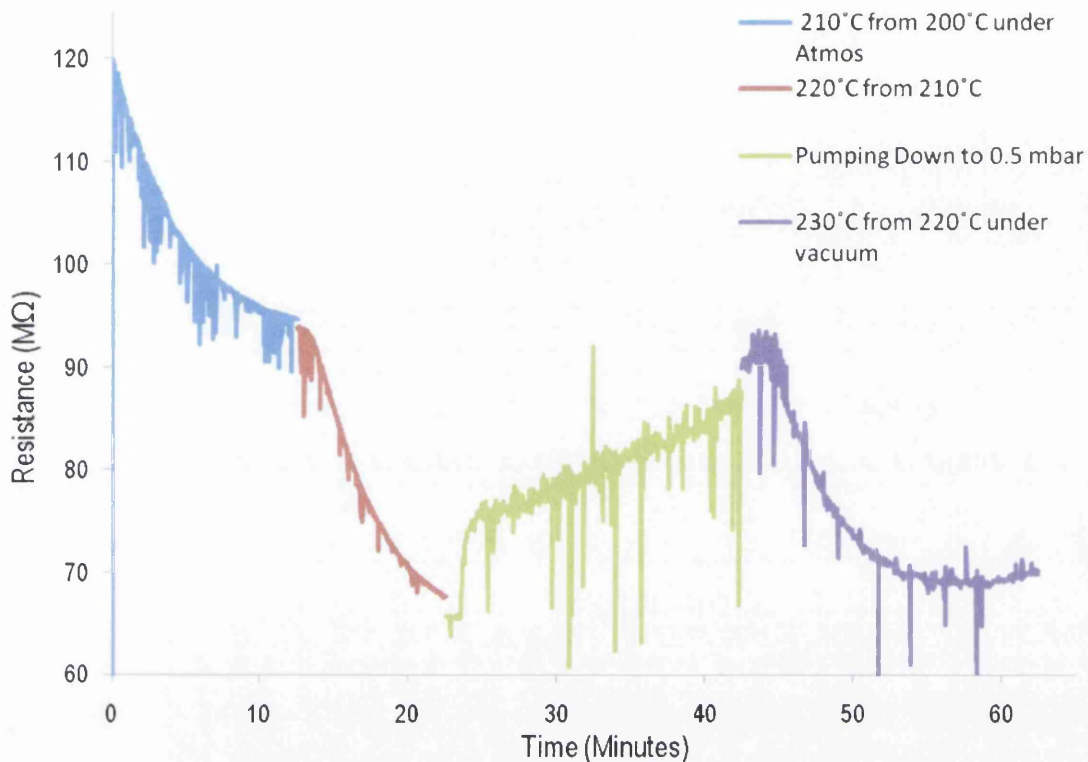
Figure 7.14 Graphical representation of the resultant change in resistance when the temperature and pressure were altered over a period of one hour.

The chamber was then pumped down to 5×10^{-1} mbar from atmospheric pressure and the measured resistance increased slightly (figure 7.14 green line). This result could be due to the tube being under vacuum hence certain species in the air were unable to donate electrons through interaction with the surface atoms of the zinc oxide which would previously happened when the tube was at atmospheric pressure. The lack of donation would have reduced the conduction and hence increased the resistance corresponding to the observed change. The temperature was then increased to 230°C and the resistance initially increased but then dropped significantly (figure 7.14 purple line). This increase in temperature and subsequent decrease in resistance would be due to the same effects as discussed aboveThe effect of altering the pressure within the tube on the resistance was examined further in a separate experiment, the results are shown in figure 7.15. The device was at a constant temperature of 230°C and the measured resistance was steady. The vacuum pump was then switched off and the resistance

was monitored for 5 minutes. As observed from the first part of the graph the resistance slowly decreased. This result could be due to a small leak present in the tube.
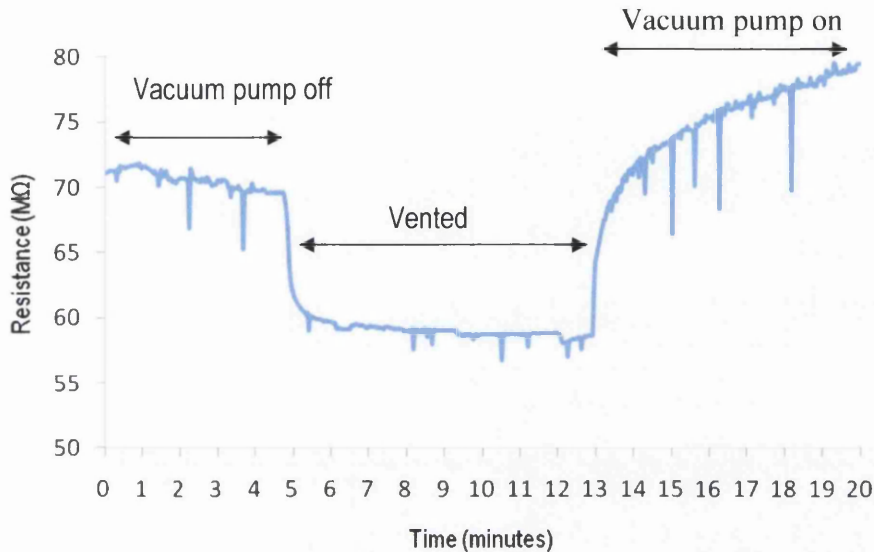
Figure 7.15 Graphical results from the zinc oxide nanowire device at vacuum and atmospheric pressure.

After 5 minutes the tube was fully vented atmospheric pressure and as seen the resistance dropped dramatically but very quickly stabilised. This would be related to the increase in conduction due to the interaction between the surface atoms of the nanowire and the molecules in the air. After 13 minutes had passed the pump was reconnected and the resistance sharply increases. This result is consistent with that observed in 7.14 where the sharp increase in resistance when the vacuum pump is switched on. As the temperature in the furnace is at 230°C the gases will be very weakly absorbed on to the surface of the nanowire and hence their swift removal due to the pump is responsible for the increased resistance.

Another way to explain these results is to compare them to those published by Wan et al in Applied Physics Letters [3]. The decrease in resistance is due to the modification of the electrical properties of the nanowire through absorption of molecules on to the surface of the nanowire. When the nanowire is vented to air as shown in figure 7.15 the conduction increases which could be a result of an oxygen molecule absorbing on to the surface of the nanowire and donating electrons to the surface molecules of the nanowire. This leads to an increase in the concentration of electrons or mobile charge carriers which increases the conduction through the nanowire and

hence reducing the resistance. It is also important to note that as the diameter of the nanowires is so small it would be fair to expect the bulk electronic transport properties of the entire nanowire will also change. Wan et al termed this a conductive switch where the entire conductivity is determined totally by the surface.

The effect of vacuum and temperature on the zinc oxide nanowire device has been explored, however it is important to consider the effect on the resistance of exposure of the nanowire to various gases. The nanowire device was exposed to oxygen and argon and the corresponding change in resistance was recorded and the graphical results are shown in figure 7.16.

In this experiment the device starts under vacuum at a pressure of 5×10^{-1}mbar and at a temperature of 220°C. The resistance of the device was recorded and found to be stable. Initially argon was allowed to flow through the tube at a rate of 95sccm (standard cubic centimetres per minute) so that the pressure inside was 30mbar. The resistance is observed to be steadily increasing as seen by the blue line in figure 7.16. This result is unexpected and could be due to other residual gases in the argon line being carried along by the flow of argon and reacting with the device. A 5% flow of oxygen was added to the argon gas and the corresponding change in resistance is shown in dark red on figure 7.16. However it does appear that the increase in resistance continues at the same rate as it did when there was no oxygen added to the argon. This would indicate that the effect of the oxygen in being masked in some way, possibly by whatever it was which gave anomalies when the device was exposed to argon. The flow of gases was stopped and the tube was evacuated with the pump from 30mbar to 5×10^{-1}mbar and the resultant change in the resistance was recorded as shown by the green line in 7.16. At approximately 50 minutes the pump is applied and the resistance rapidly increases and the meter is overloaded at 120MΩ. The tube was immediately vented to air and the resistance dramatically dropped almost instantly. . After a period of time the resistance began to plateau and the device was heated from 220°C to 230°C as shown by the purple line in 7.16 the resistance increased. The pump was then switched on and pumped the system down to vacuum and the resistance increased, instantly overloading the meter in less than a minute (light blue line in 7.16). The temperature was further increased to 240°C and the resistance of the device decreased as shown by the later part of the light blue line at about 90minutes.
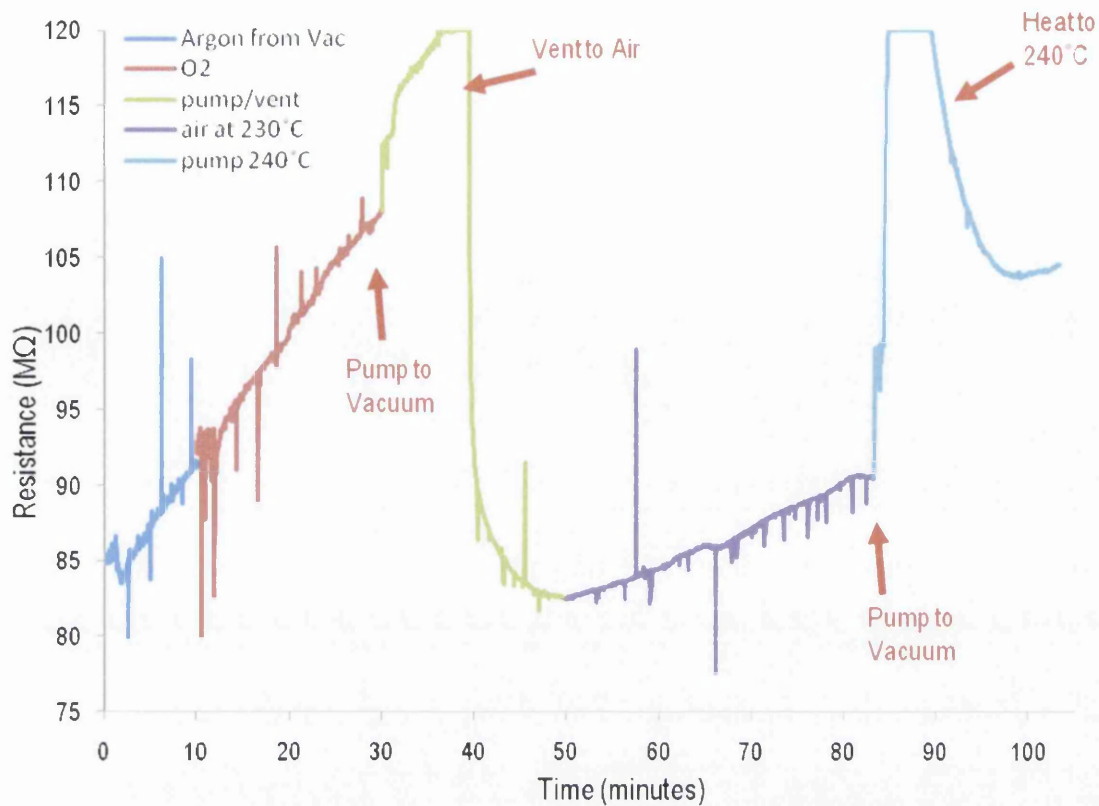
Figure 7.16 The change in resistance of nanowire device when the device was exposed to argon (blue line), oxygen (red line) and ambient air (purple line).

The sensitivity of the sensor was calculated using the equation outlined below and it was determined that this single nanowire sensor showed a 10% sensitivity.

$$sensitivity\ (\%) = \frac{Conductance\ o_2 - Conductance\ Ar}{Conductance\ Ar} \times 100 \qquad Equation\ 7.2$$

This level of sensitivity is extremely poor for a nanowire device and the experiments need to be dissected in order to examine areas of improvement.

7.2.5 Zinc Oxide Mat Sensor

Aside from the single nanowire gas sensors presented in this thesis, additional work has previously been carried out in the laboratory using large quantities of nanowires on a single substrate to create a "mat". An SEM image of these nanowires is shown in figure 7.17.
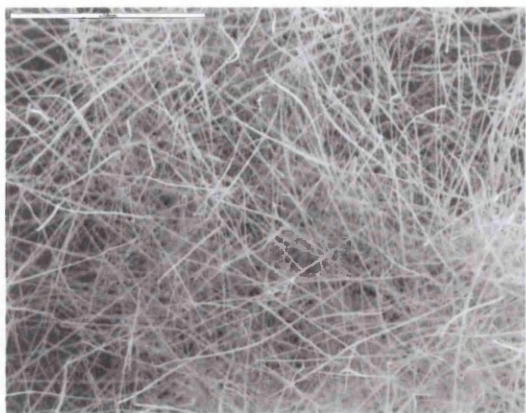
Figure 7.17 A SEM image of a mat of ZnO nanowires

A typical substrate with interdigitated platinum electrodes is shown in Figure 7.18. As-grown ZnO nanowires grown on GaN are taken and placed in a toluene and agitated in an ultrasonic bath for 15 minutes, creating a solution of ZnO nanowires. This solution is pipetted onto the sensor substrate and the toluene is evaporated. This is repeated until a suitably thick ZnO nanowire mat is created on the substrate. The sensor is then connected to a pico-ammeter inside a sealed horizontal tube furnace, similar to the gas sensing experiments described in chapter 5.

Platinum Electrodes
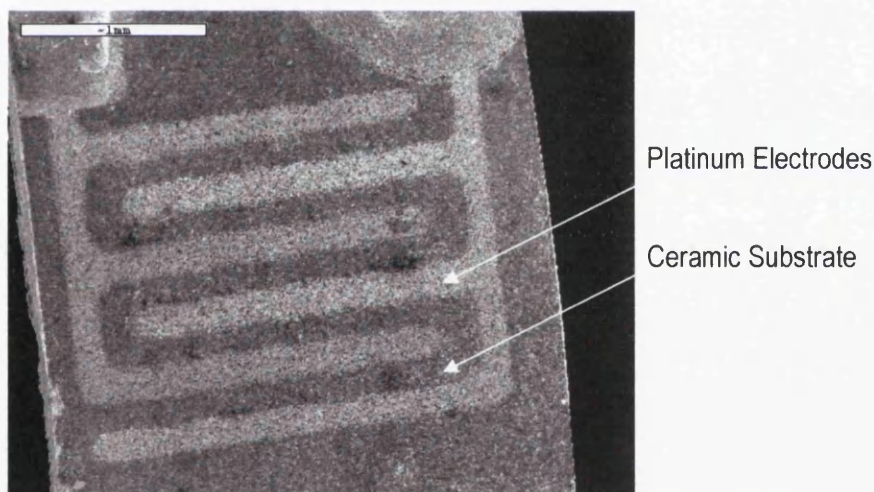
Ceramic Substrate

Figure 7.18 A scanning electron miscroscopy image of an interdigitated gas sensing substrate. The bright path corresponds to the platinum electrodes, the darker background is the ceramic substrate.

The starting resistance of the ZnO mat film is 1.6MΩ, almost 2 orders of magnitude lower than that of the single nanowire devices. At the start of the experiment the chamber was pumped to vacuum and there was a corresponding drop in resistance as shown in figure 7.19. Then the temperature was increased to 200°C. At this point the investigation was looking for a temperature at which the resistance would level out and remain constant, demonstrating a stable operating

temperature for the sensor. Since the resistance displayed no signs of doing so when raised to 200°C, the decision was taken to raise the temperature to 400°C. As demonstrated by the yellow line on the graph shown in figure 7.19. Once the resistance had stabilised, the chamber was then taken back up to atmospheric pressure with a pure Argon atmosphere. This change caused a slight increase in resistance which gradually plateaued. The next step was to introduce oxygen into the chamber in the ratio of 10% Oxygen to 90% Argon. This immediately caused the resistance to increase as shown by the dark purple line in figure 7.19. The oxygen was turned off whilst the argon continued flowing to maintain a constant pressure, the resistance plateaued but did not reduce. The chamber was then pumped to vacuum once more, the resistance decreased and stabilized quite rapidly, but was still higher than before the oxygen was introduced into the chamber.
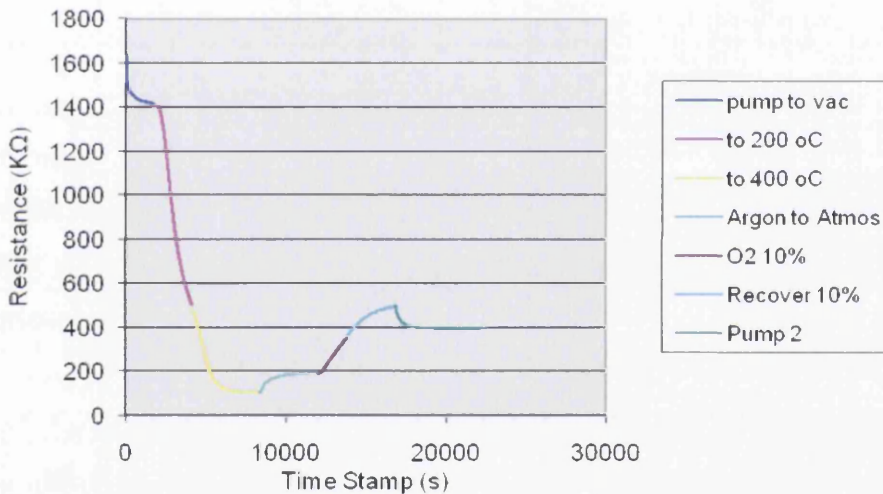
Figure 7.19 Graph of resistance against time showing the change in resistance of the sensor with different environmental conditions

The results from the exposure experiment show that the sensor does react in quantifiable ways when exposed to a gas, and the experiment was repeated numerous times with almost identical results to those shown in Figure 7.19. At the start of the experiment, when the chamber was pumped to vacuum, there was a decrease in resistance, probably due to the removal of the oxygen in the air (the presence of oxygen causes an increase in the resistance of ZnO nanowire). Then the temperature of the chamber was increased and this was acompanied by a drop in resistance, higher temperatures would increase the conductivity of the nanowire and also encourage the removal of adsopted gases and water vapour. When pure Argon was introduced

into the chamber the resistance increased. It is thought that there may have been some contaminates, such as oxygen or water vapour, in the connecting tubes and these contaminates caused the slight increase in resistance.

Oxygen was introduced into the chamber with the argon gas and increased in resistance. Oxygen is an oxidising agent, when in contact with the ZnO nanowire removes electrons from it. Finally the chamber was pumped to vacuum resulting in a drop in resistance as the oxygen was removed. This ZnO nanowire mat sensor has been shown to be fairly sensitive to the presense of oxygen, the change in resistance is also very quick and is recoverable.

The ZnO nanowire mat sensor does appear more sensitive than the single nanowire sensor and the starting resistance is significantly lower. The exceedingly high resistance of the single nanowire sensor could be improved in the future with better processing techniques. However, it is still interesting to compare the response of the sensors to verify that the single nanowire sensor is functioning correctly. Both sensors needed to run at elevated temperature and showed an increase in resistance when argon was introduced into the testing chamber. This is probably due to the contaminants in the gas lines or on the walls of the chamber as argon is not expected to illicit such a reaction, and in some way shows that both sensors are relatively sensitive, but at present we are unable to quantify this or indentify the source.

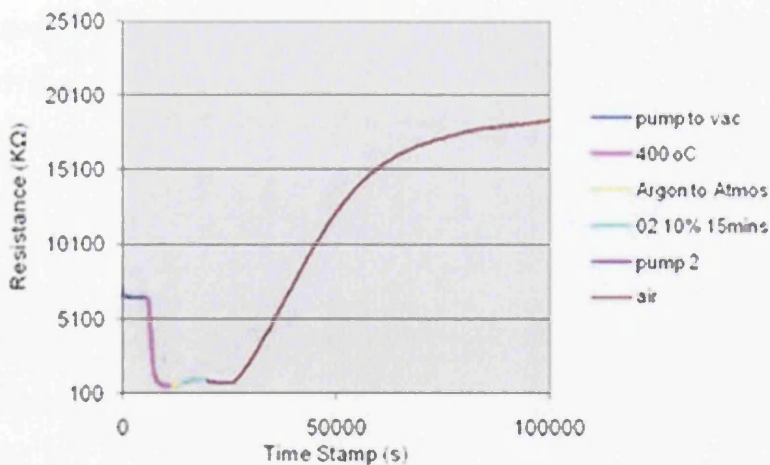*Figure 7.20 Repeat experiment with zinc oxide mat sensor showing exposure to air.*

For the mat sensor, when oxygen was introduced into the chamber the resistance increased, but crucially the resistance change due to the introduction of argon gas had stabilised first. For the single nanowire sensor, the resistance increased along a similar gradient to that of the introduction of argon, one would expect oxygen to increase the resistance of the sensor as it is an oxidizing gas hence removes electron from the ZnO nanowire surface and reducing its conductivity, unfortunately its effect here is hard to quantify. The main difference between the two sensors is when they are subjected to vacuum after an exposure. While the matt nanowire sensor showed a drop in resistance, the single nanowire sensor showed a drastic increase, overloading the ammeter in a few minutes. This response was shown to be repeatable and at least shows that the sensor is incredible sensitive, but it is hard to identify the reactant. The most likely reason for this response is small leaks in the chamber – when the pump is on air would be sucked through these and expose the sensor to air increasing the resistance, most likely it was the higher oxygen content or water vapour.

The figure 7.20 is a repeat of the tests on the matt nanowire sensor, it behaves the same as previously, but in this experiment the sensor was exposed to air, although the change was more gradual, the resistance did increase drastically in a similar way to that of the single nanowire sensor.

7.3 Summary

The zinc oxide nanowires were deposited on to glass substrates and then titanium contact electrodes were deposited using a photolithography technique. The nanowire-titanium electrode devices demonstrated good conduction when examined with a probe station by applying a voltage between -10V and +10V.

The resistance of these devices were examined and measured by increasing the temperature of the device. This simple experiment illustrated the temperature dependent resistance of these devices and showed that the resistance decreased with increasing temperature. This behaviour would be expected when examining a semiconductor material. The increasing temperature give the atoms extra energy and allow them to release electrons, which are then able to move more freely hence increasing the conduction and lowering the resistance.

The resistivity of the nanowire devices were calculated from the data obtained in the temperature dependence experiments. The difference in the resistivity calculated for each device corresponds to the change in cross-sectional area. The resistivity increases with increasing cross sectional area which would be expected from equation 7.2.

The same devices were then used for gas sensing experiments by exposing the device to atmospheric pressure and vacuum, increasing temperature and argon and oxygen gases. The device showed a decrease in resistance with increasing temperature but showed little in the way of trend for gas exposure of vacuum. These experiments are not conclusive in terms of showing which gases reacted with the ZnO nanowire sensor, or were they able to quantify the magnitude of change with known amounts of gas. However these experiments do show that the sensor works, and that the change from air to vacuum is extremely fast.

The single nanowire sensor was compared to recent literature where the sensor has been exposed to a range of substances including carbon monoxide [2, 4], nitrogen dioxide [4, 5], oxygen [6] and ethanol [4] and previous projects (section 7.2.5). Overall the sensor shows good reaction to the environmental changes within the chamber however there does not appear to be the drastic changes as shown in the literature. Therefore this experiment can be considered as a feasibility study showing that single nanowire sensors are worthy of future investigation.

7.4 References

1.   Arnold M., A.P., Pan Z., and Wang Z. L., *Field effect transistors based on single semiconducting oxide nanobelts.* J. Phys. Chem., 2003. **107**: p. 659-663.
2.   Fan Z., a.L.J.G., *Chemical sensing with ZnO nanowire field effect transistor.* IEEE transactions on Nanotechnology, 2006. **5**(4): p. 393-396.
3.   Wan Q., L.Q.H., Chen Y. J., Wang T. H., He X. L., Li J. P., and Lin C. L., *Fabrication and ethanol sensing characteristics of ZnO nanowire gas sensors.* Appl. Phys. Letts, 2004. **84**(18): p. 3654-3656.
4.   Comini E., F.G., Sberveglieri G., Pan Z., and Wang Z., *Stable and Highly sensitive gas sensors based on semiconducting oxide nanobelts.* Appl. Phys. Letts, 2002. **81**(10): p. 1869-1871.
5.   Sadek A., W.W., Kalantar-zadeh K., and Choopun S. , *ZnO nanobelt based conductomeric H2 and NO2 Gas sensors.* Chiang Mai University, 2005.
6.   Fan Z., W.D., Chang P., Tseng W., and Lu J. G., *ZnO Nanowire field effect transistor and oxygen sensing property.* Appl. Phys. Letts, 2004. **85**(24): p. 5923-5925.

Chapter 8

Conclusion

8.1 Introduction

This chapter encompasses conclusions drawn from experimental work carried out in this thesis and the potential future experiments that could be achieved if this work was used as a basis. The chapter also includes a brief section of the societal and ethical considerations which are becoming ever more prevalent when describing the application of Nanotechnology within industry and everyday life.

8.2 Experimental results

The aim of this research was to fabricate a gas sensing device based on a single zinc oxide nanowire. The most important consideration was to the nanowire itself and ensuring conduction and a good connection with the electrodes. This was achieved by experimenting with the nanowire underneath the electrodes and on top of the electrodes and with different electrode patterns both of which could be expanded on in future work.

Another important concept that arose due to this work is the work with electric force microscopy and imaging the samples with varying tip biases. This work showed the potential of the nanowires to be charged and undergo charging when imagined with a large enough tip bias. This work was used to determine the dielectric constants of the silicon substrate, zinc oxide nanowires and silicon nanowires.

8.3 Recommendations for Future Work

The work outlined in this thesis is the beginning of a long road into exploring and exploiting nanoscale materials. In relation to the gas sensing experiments the experiments would be extended to include work on passivating the devices by spin coating with polymers [1] and exploring the effect upon gas sensing capability and electrical conduction.

In order to fully understand zinc oxide capabilities as a nanoscale electronic material the piezoelectric properties need to be explored in detail. Probing the nanobelt device with an AFM tip and recording the corresponding change in conductance would be a good place to start building upon the work published by Han et al but the device will be synthesised according to the

procedure outlined in chapter 5 [2]. The probing of the nanobelt device in this way will generate information on the tensil strain experience by the belt and hence the piezoelectric capabilities. The results observed in chapter 6 could be extended to differing materials and possibily biological materials including electrically conducting bacteria [3, 4].

Future experiments would also include expanding upon the work in this thesis, exploring different materials and determining their dielectric constants in order to prove the technique described. In regards to the gas sensing experiments the nanowire samples would be exposed to a variety of gases and the samples would be more robustly made.

8.4 Societal and Ethical Considerations

The ethical and societal concerns over nanotechnology must be seriously considered by both academia and industry. There have been many research projects commissioned all over the world. An associate professor at the University of Virginia, Dr Berne, has been funded to explore the developing ethics concerning nanotechnology [5]. Dr Berne has set up workshops between students and elderly members of society to get an overall perspective on the ethical, cultural and societal implications of new technology.

The main concern over the development of nanotechnology focuses more on the potential applications of the technology rather than the underlying science [6]. There are uncertainties over the impact of new nanomaterials on human health for example as nanoparticles are the same size scale as cellular components would they be able to escape the natural defences and damage cells directly, without the involvement of the immune system. However, it can be deducted that humans have always been exposed to some type of nanoparticle whether this be from atmospheric photochemistry or forest fires.

Nanotechnology is thought to be the next industrial revolution. It has become apparent that this revolution could exasperate the divide between rich and poor countries. This divide has been termed the 'nanodivide' [6]. The development of a new technology invariably squashes an older existing industry [7]. Much of what nanotechnology aim to be able to replace hinges on raw materials sourced from many developing countries for example Chile, African countries, Russia

and China [8]. This invariably will affect the economy in these countries which will promote the nanodivide. The divide also affects the ability of certain countries to promote research into this vast area. Richer countries are more likely to afford to waste money on research which improves the understanding of techniques but does not necessarily product a marketable device. Poorer countries do not have this luxury hence they must develop well defined projects and not simple follow other countries. This also increases the risk of hazards from the lack of research experience and also strict safety regulations. This may lead to developmental test phases on humans in developing countries due to the lack of regulations for these experiments and less public attention to hazards. Invariably this nanodivide will happen and when it does developing countries may insist on their rights being covered by international conventions. United Nations Educational, Scientific and Cultural Organisation (UNESCO) produced a universal declaration on bioethics and human rights [9]. This included the protection of sharing of both knowledge and the benefits of medical, scientific and technological developments with under developed countries. This declaration should go someway to protect developing countries and help support and improve the relationship between rich and poor countries. To include developing countries in the nanotechnology boom would potentially enable them to catch up economically [10].

The main concern over the development of nanotechnology is that it should not become exclusive to developed countries which are already enjoying a much improved standard of life. The potential applications should be geared towards improving the life of developing countries thought improved and cheaper products for example water filters. Researchers and industry must not allow the divide to be exacerbated beyond repair.

The public acceptance of nanotechnology will depend heavily upon the development of legal and regulatory frameworks [6]. This may help to quell fears over the control of nanotechnology and also who benefits from the development of this new technology. Nanotechnology is not monolithic but a collection of very diverse science and technologies in the making. Therefore society will still have an opportunity to shape the development according to specific sociocultural conditions; language, cultural heritage, economy, politics and ethics [10].

8.5 References

1.   Hong W., et al., *Electrical properties of ZnO nanowire field effect transistors by surface passivation.* Colloids and Surfaces A: Physiochem. Eng. Aspects, 2008. **313-314**: p. 378-382.

2.   Han, X., Jing G., Zhang X., Ma R., Song X., Xu J., Liao Z., Wang N., Yu D.,, *Bending-induced Conductance Increase in Individual Semiconductor Nanowires and Nanobelts.* Nano Res, 2009. **2**: p. 553-557.

3.   Debabov V. G., *Electricity from microorganisms.* Microbiology, 2008. **77**(2): p. 123-131.

4.   Lovley R., *Bug Juice: Harvesting electricity with microorganisms.* Nature Reviews Microbiology, 2006. **4**: p. 497-508.

5.   Rosalyn W. Berne. *Intergenerational Instruction in Engineering Ethics about the Future.*2006[cited;Availablefrom:
        www.onlineethics.org/cms/edu/instructguides/genberne.aspx.

6.   The Royal Society and The Royal Academy of Engineering, *Nanoscience and nanotechnologies: opportunities and uncertainties.* 2004. p. 1-116.

7.   Busham B., *Handbook of Nanotechnology.* 2004, Springer-Verlag Berlin Heidelberg: Berlin, Germany.

8.   Schummer J., *The Impact of Nanotechnologies on Developing countries,* in *Nanoethics: The Ethical and Social Implications of Nanotechnology,* L.P. Allhoff F., Moor J., and Weckert J., Editor. 2007, Wiley: Hoboken NJ. p. 291-307.

9.   United Nations Educational Scientific and Cultural Organisation.   [cited; Available from:
        www.unesco.org.

10.   Schummer J., *Cultural diversity in nanotechnology ethics.* Interdisciplinary Science Reviews, 2006. **31**(3): p. 217-230.